Two High-Sensitivity Pulsar Searches

David J. Nice

A Dissertation
Presented to the Faculty of Princeton University
in Candidacy for the Degree of Doctor of Philosophy

Department of Physics

October 1992

Abstract

We have undertaken a program of two searches at radio wavelengths for pulsars using the Arecibo Observatory. One search covered 70 square degrees of sky along the Galactic plane with sensitivity to pulsars with periods as short as 1 ms. The second search covered 170 square degrees between Galactic latitudes -50° and -30° with sensitivity to pulsars with periods of 0.5 ms or more. The sensitivity to long-period pulsars in both surveys was of order 1 mJy, with reduced sensitivity at the shortest periods.

Twenty-five pulsars were detected between the two surveys. Ten of these had previously been discovered. Of the remaining fifteen new pulsars, thirteen are relatively young, slow pulsars, with periods between 0.212 s and 5.094 s. The latter period is the longest of any known radio pulsar; this pulsar also has an extraordinarily short duty cycle of 0.4%.

Two millisecond pulsars were found. PSR J2019+2425 has a period of 3.934 ms and is at a distance of ~ 1 kpc. It is in a 76.5-day binary orbit with a $\sim 0.3\ M_\odot$ companion. Its orbital eccentricity is 1.1×10^{-4}. The spin-down rate of this pulsar is extremely small, and its evolutionary timescale of 9×10^9 yr is the longest of any known pulsar. Both the low eccentricity and the long evolutionary timescale put limits on violations of the strong equivalence principle which are competitive with the best previous limits.

The second newly found millisecond pulsar, PSR J2322+2057, has a period of 4.808 ms and a distance of ~ 0.8 kpc. It is the second isolated millisecond pulsar found outside of globular clusters. Its distance of nearly ~ 0.5 kpc from the Galactic plane suggests that millisecond pulsars have a large scale height.

Contents

Abstract **i**

Acknowledgements **xi**

A Note on Pulsar Names **xiii**

1 Why Study Pulsars? **1**

1.1 Overview 1
1.2 Neutron Stars 2
1.3 Pulse Timing 2
1.4 Pulsar Distances and the ISM 5
1.5 Binary Pulsar Systems 6
1.6 Projects Undertaken 7

2 Overview of Pulsar Searching **9**

2.1 The Nature of Pulsar Signals 9
2.2 Maximizing the Signal-to-Noise Ratio 10
  2.2.1 Signal 10
  2.2.2 Noise 12
  2.2.3 Signal-to-Noise Ratio 14
2.3 Interstellar Dispersion 16
2.4 Filtering and Sampling 18
2.5 The Nyquist Criterion 19
2.6 Untargetted Pulsar Surveys 21

3 The Search Algorithm and Software 25

3.1 Dispersion Removal 26
3.2 Search for Periodic Signals 28

4 The Galactic Plane Survey 33

4.1 Hardware and Sensitivity 33
4.2 Sky Coverage 37
4.3 Results 39
4.4 PSR J1951+11 50

5 The High Latitude Survey 53

5.1 Rationale 53
5.2 Hardware and Sensitivity 54
5.3 Sky Coverage 57
5.4 Results 60

6 PSR J2019+2425 63

6.1 Timing Observations 63
6.2 Profile and Flux 65
6.3 Timing Results 67
6.4 The Binary System 70

7 PSR J2322+2057 73

7.1 Profile and Flux 73
7.2 Timing Observations 75
7.3 Isolated Millisecond Pulsar Formation 77
7.4 Limits on Planetary Companions 78

8 Applications of the Millisecond Pulsars 81

8.1 Assumptions 81
8.2 PSR J2019+2425 and General Relativity 82
  8.2.1 Precession of the Orbit 83
  8.2.2 Gravitational Radiation 84

8.2.3 Shapiro Delay 84

8.3 PSR J2019+2425 and the Gravitational "Constant" G 87

8.3.1 Orbital Effects 87

8.3.2 Spin-down Effects 89

8.4 The J2019+2425 Orbit and the Strong Equivalence Principle . 90

8.5 Proper Motion and Parallax 91

8.6 Conclusion 94

A Autocorrelation Spectroscopy **97**

B Noise Statistics **101**

References **105**

List of Figures

1.1 Galactic distribution of pulsars. 3
1.2 Pulsar periods and spin-down rates. 4

2.1 Arecibo Observatory beam geometry 11
2.2 The effect of dispersion 17
2.3 Fourier decomposition of pulse profiles. 20
2.4 The Arecibo observing area in Galactic coordinates 22
2.5 Surveys in the Arecibo-Galactic plane region. 23

3.1 Search software output 32

4.1 Plane survey: losses due to sky temperature and zenith angle . 37
4.2 Plane survey sensitivity 38
4.3 Plane survey coverage: second phase only 40
4.4 Plane survey coverage: both phases 41
4.5 Galactic latitude distribution of plane survey 42
4.6 New pulsars discovered in the plane survey 46
4.7 PSR J1951+11 subpulses 51

5.1 High latitude survey sensitivity 57
5.2 Sensitivity comparison between the surveys 58
5.3 High latitude survey coverage 59
5.4 New pulsars discovered in the high latitude survey 62

6.1 Pulse period as a function of time 64

6.2 PSR J2019+2425 profiles 66
6.3 PSR J2019+2425 timing residuals 69
6.4 PSR J2019+2425 orbital geometry 70
6.5 PSR J2019+2425 companion mass 71

7.1 PSR J2322+2057 profiles 74
7.2 PSR J2322+2057 phase residuals 76
7.3 Simulated planet around PSR J2322+2057 79

8.1 Uncertainty of J2019+2425 mass measure 86
8.2 Simulations of proper motion and parallax 93

List of Tables

2.1 Untargetted pulsar surveys 24

3.1 Search period limits 31

4.1 Interference periods excised in Galactic plane survey 42
4.2 Known pulsars not detected in the Galactic plane survey . . . 43
4.3 Known pulsars detected in the Galactic plane survey 44
4.4 New pulsars discovered in the Galactic plane survey. 45

5.1 Recycled pulsars detected in recent surveys. 54
5.2 Interference periods excised in the high latitude survey 60
5.3 New pulsars discovered in the high latitude survey 61

6.1 PSR J2019+2425 profile component parameters 67
6.2 PSR J2019+2425 timing parameters 68

7.1 PSR J2322+2057 timing parameters 75

Acknowledgements

It is a pleasure to credit my advisor, Joe Taylor, as the driving force behind this work. The surveys described in this thesis are an extension of many years of his work, and the tools used to conduct them have drawn heavily on his experience in the field of pulsar research.

Andy Fruchter blazed the way for the Galactic plane search and helped me get started using the Arecibo Telescope. Alex Wolszczan helped set up observations for the high latitude search. Fernando Camilo assisted in collecting follow-up data for the high latitude search.

The staff of the Arecibo Observatory have always been courteous and helpful. Particular thanks go to Angel Vásquez for collecting a large portion of the millisecond pulsar timing data included here.

I learned much through work on other projects while at Princeton. Dan Stinebring taught me much of the radio astronomy I know, and some of his enthusiasm for the subject has rubbed off. I have had the benefit of friendship and collaboration with several other graduate students in the pulsar lab, especially Zaven Arzoumanian, Vicky Kaspi, Marty Ryba, and Steve Thorsett.

While working on this thesis I was supported by a fellowship from the U.S. Department of Education under the program of Grants in Areas of National Need. Additional backing came from the National Science Foundation through support of the lab in Princeton, the Pittsburgh Supercomputer Center, and the Arecibo Observatory (a facility of the National Astronomy and Ionosphere Center, operated by Cornell University).

Pulsar parameters for figures and tables in this document are from a catalog compiled by A. G. Lyne, R. N. Manchester, and J. H. Taylor.

Thanks to my parents for twenty-seven years of support (and especially for arranging an unexpected birthday party in Puerto Rico during a long observing run).

This thesis is dedicated to Marian Wentworth♡.

A Note on Pulsar Names

Pulsars have been named using three distinct systems. Initially names were assigned using a combination of discovery observatory and right ascension (based on the B1950.0 coordinate system): "CP 1919" described a pulsar with $\alpha = 19^{\mathrm{h}}19^{\mathrm{m}}$ discovered by a group at Cambridge. As more pulsars were discovered, declinations were added and observatory names were dropped. CP 1919 became "PSR 1919+21", since it is at $\delta = +21°$.

More recently, the International Astronomical Union has recommended a common nomenclature scheme for all astrophysical sources of radiation (Dickel, Lortet & de Boer 1987). Names are to have the general form

DDDD Errrrrr±rrrrrr (NNNNN) sssss

where DDDD is the source type or detection technique, E is a code for the coordinate system used to describe the source location, rrrrrr±rrrrrr is the position of the source, NNNNN is an optional associated name, and sssss is optional supplementary information. For pulsars this scheme results in names such as "PSR B1919+21" when the traditional B1950.0 coordinate system is used.

The IAU (1976) has recommended using the J2000.0 coordinate system for all objects named after 1 January 1984. PSR B1919+21 would become "PSR J1921+2153" in this scheme, although there is a provision for continuing to use old names for objects named before 1984. Note that the new name has extra precision included in the declination value; such extra precision is encouraged but not mandatory under the new scheme.

In this work we use a mix of old and new coordinate systems. Previously discovered pulsars will be described in the B1950.0 system, preceded by "PSR B" (e.g., "PSR B1919+21"). Newly discovered pulsars will be named under the J2000.0 system, indicated by a "J" (e.g., "PSR J2019+2425").

Chapter 1

Why Study Pulsars?

1.1 Overview

Pulsars are remarkable objects. In the quarter century since their discovery, they have had a impact on many fields of science. Understanding their composition is a challenge in nuclear and condensed-matter physics. Their elusive emission mechanism is a complex problem in electromagnetics, atomic physics, and particle physics. Explaining their creation, evolution, and distribution is a classical astronomical task. The greatest contribution of pulsars observations, however, is their use as probes of other phenomena beyond pulsar physics. Pulsars provide great insight into the character of the interstellar medium; they provide fundamental beacons for astrometry; and they are also a most fertile ground for tests of general relativity.

In this chapter, we discuss the basic characteristics of pulsars and the applications of pulsar physics. We embarked on the searches for new pulsars which form a large part of this thesis without knowing what we would find. Instead, we assumed that the rich variety of new science attributed to pulsars would continue, and that adding more pulsars, whatever their character, to the general body of knowledge would be a useful and rewarding task. We have not been disappointed.

1.2 Neutron Stars

As a massive star evolves, its light elements are converted into heavier elements through nuclear fusion. Energy released by fusion creates an outward pressure in the star, which balances the inward pressure of gravity, resulting in a stable star of some finite size. After some time, as the lighter elements are consumed, the fusion process fails to produce the pressure necessary to support the star, and the star collapses. The core rapidly heats, causing a sudden increase in luminosity even as the star is collapsing. The result of the collapse is two-fold: a huge amount of energy is released, visible in the form of a supernova explosion; and a highly compact object is produced near the center of the original star. This compact object is a neutron star—a body whose protons and electrons largely have been converted to neutrons by inverse beta decay. The detection of neutrinos from Supernova 1987A (Hirata *et al.* 1987; Bionta *et al.* 1987) confirmed the production of a neutron star during supernova explosions.

Pulsars are a class of neutron stars distinguished by their emission of extremely regular pulsed radio signals. The details of this process are not understood, but some key features are clear. Like lighthouses, pulsars emit radiation in fixed directions relative to their surfaces, producing periodic signals to an observer on a fixed line of sight. Approximately 550 pulsars are currently known, with rotation periods ranging from under 1.6 milliseconds to over 5 seconds.

1.3 Pulse Timing

The pulse trains emitted by pulsars are extremely stable, in at least one case comparable to the best terrestrial atomic clocks: arrival times of pulses from PSR 1937+21 can be predicted with two microsecond accuracy over a time span of nearly a decade (Stinebring *et al.* 1990). Pulsar rotation behavior fits an extremely simple model: in all but the youngest pulsars, the rotation period is a slowly increasing linear function of time; these two quantities (period and

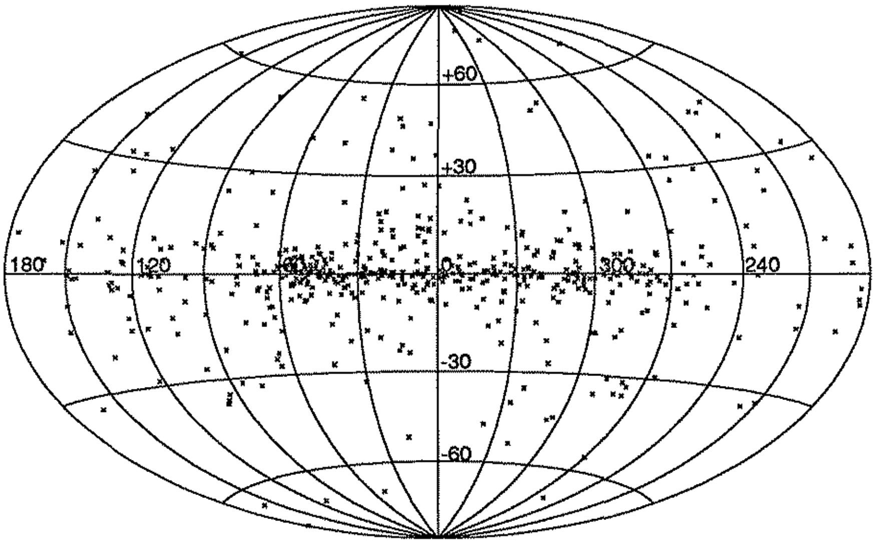

Figure 1.1: Galactic distribution of pulsars.

period change over time) are free parameters in the timing model. Propagation time across the 500-light-second-radius orbit of the earth significantly affects the pulse arrival times on earth, in a manner which depends on the position of the pulsar in the sky. Thus the position of the pulsar, described by two further parameters, must be included in the model. Finally, the absolute arrival time of a pulse is arbitrary, adding a fifth parameter.

Many facts about pulsars emerge from this five-parameter model. The observed positions have been used to study the pulsar population as a whole (see figure 1.1): a clear concentration of pulsars along the Galactic plane is evident, reflecting pulsars' origins in Galactic supernovae. (This concentration is in part a selection effect: since more pulsars are expected along the Galactic plane, searches for new pulsars have often concentrated there.) Not clear from the diagram is that pulsars tend to be a bit farther from the Galactic plane than their massive progenitors: their scale height is 230 parsecs, compared with 80 parsecs for O-B stars (Manchester & Taylor 1977). Changes in pulsar positions over time indicate that most have relatively high velocities directed away from the Galactic plane (Lyne, Anderson & Salter 1982).

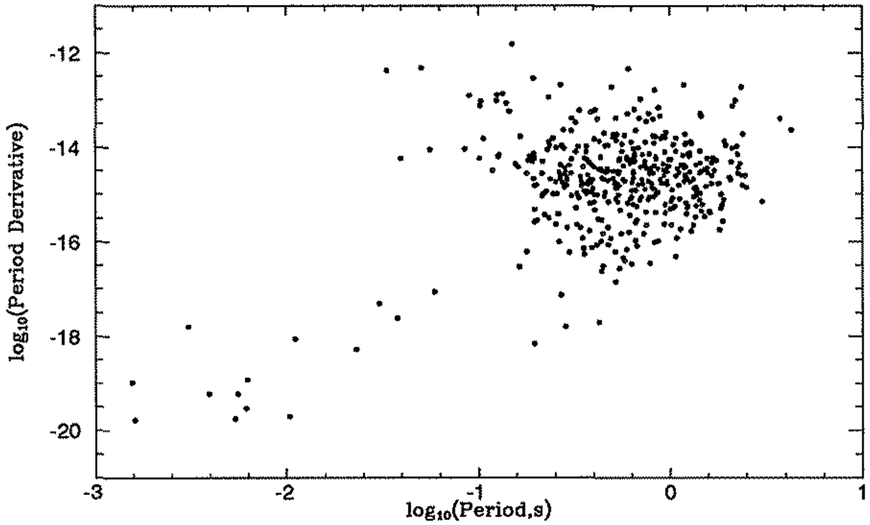

Figure 1.2: Pulsar periods and spin-down rates.

Individual pulsar position measurements can be used to associate pulsars with other objects; for instance, the discovery of PSR 0531+21 in the Crab supernova remnant was the observational "smoking gun" that linked pulsars and supernovae (Staelin & Reifenstein 1968). The very high precision positions obtained for a few pulsars are used to measure the differences between standard reference frames: pulsar positions from the timing model are derived as consequences of the earth's orbital motion, and thus they are in the reference frame of the Solar System ephemeris used to fit the model. Other astronomical observations use reference frames based on the positions of stars and other objects, and, through very long baseline interferometry, pulsar positions can be measured in these frames as well. Combining the separate position measures allows the reference frames to be "tied" together.

The period, P, and spin-down rate (observed as a period derivative, $\dot{P}$) of known pulsars are displayed in figure 1.2. The most obvious feature of the distribution is a division between the majority of pulsars, which have relatively large periods (typically 1 s) and large period derivatives (typically 10^{-15}), and a small number of fast (1.6 ms minimum) pulsars with much smaller spindown rates (typically 10^{-18}). These differences are elucidated by defining two new variables, the characteristic age τ and surface magnetic field B_0. Dimensional analysis suggests $P/\dot{P}$ as a measure of a pulsar's age. A more exact analysis, which assumes the neutron star spin-down is entirely due to braking torques from a rotating magnetic dipole at its center, gives a characteristic age $\tau = P/2\dot{P}$. The radius of a neutron star as a function of mass is not well known, but most equations of state for nuclear matter suggest that a typical 1.4 $M_\odot$ neutron star has a radius within a factor of two of 10^6 cm and a moment of inertia of order 10^{45} cm^{2}g. Given these values and the central magnetic dipole assumption, the maximum magnetic field at the surface is $B_0 \approx 3.2 \times 10^{19}(P\dot{P})^{1/2}$ with B_0 in Gauss (Manchester & Taylor 1977).

These formulae give ages of order 10^6 yr and surface magnetic fields of order 10^{12} G for slow pulsars. The fast-spinning pulsars, however, have much smaller magnetic fields, of order 10^{10} G, and much longer ages, typically 10^9 yr. Fast pulsars are very old objects; in some cases the evolutionary time scales are comparable to a Hubble time, $10-20\times10^9$ yr. It is believed that they are created by "spinning-up" through accretion of mass and angular momentum in a binary system. Since the increase in rotation rate gives the pulsars a second life, they are referred to as "recycled" pulsars. The short periods of these pulsars make very high precision timing experiments possible. Unlike slow pulsars, which are usually isolated objects, many of these faster pulsars are in binary orbits, surviving evidence of the spin-up phase of their evolution.

1.4 Pulsar Distances and the ISM

Interactions between long-wavelength radiation and free electrons in the interstellar medium (ISM) slightly retard propagation of the radiation. This causes radio pulses to reach the earth a bit later than they otherwise would. The overall delay is proportional to the integrated column density of electrons along the line between the pulsar and the earth, referred to as the dispersion measure: DM $\equiv \int dx\, n_e$. The delay is also a function of the frequency of the radio signals: $\delta t \propto \mathrm{DM}\, \nu^{-2}$, so the DM can be measured by comparing pulse arrival times at more than one frequency. (Details of this effect are discussed in chapter 2.) The DM is the sixth parameter of the basic observational model for an isolated pulsar. Dispersion measures are particularly important because they can be combined with other distance estimates to give a measure of the density of free electrons in the ISM.

In high-precision timing of nearby pulsars, it is in principle possible to measure parallax, the effect of the curvature of wavefronts due to the finite distance between the pulsar and the earth. In practice the small size of the effect makes this measurement difficult even on the nearest pulsars. To date, the only nonzero timing parallax measure on a pulsar is a weak constraint that places PSR 1855+09 at a distance of 1.0 ± 0.4 kpc (Ryba & Taylor 1991).

1.5 Binary Pulsar Systems

The most spectacular results from pulsar observations have come from timing studies of pulsars in binary orbits. The orbital motion of a binary pulsar can be measured to very high precision. The primary effect of the motion is a systematic change in the distance between the observer and the pulsar, resulting in periodic increases and decreases in the time it takes for a pulse to travel from the pulsar to the earth. A secondary effect is a slight change in the radio frequency of radiation emitted due to the Doppler effect.

Timing observations only allow measurement of pulsar motion projected along the line of sight, so not all orbital elements can be observed in a nonrelativistic system. (The situation is the same as that of a single-line spectroscopic binary.) A binary system has seven degrees of freedom. Five of these can be measured in any pulsar orbital system. Observationally these are described as the amplitude of the pulsar's orbit projected onto the line of sight; the orbital period; the phase of the orbit at some fixed time; the eccentricity; and the angle of periastron relative to some fixed frame. Two further free parameters cannot be measured in a Keplarian system in which only one body is observed. These two parameters can be thought of as the masses of the pulsar and its companion, or the inclination of the orbit and one of the masses.

In some systems it is possible to measure these last two parameters using the effects of general relativity in one of several ways. In a sufficiently small eccentric orbit, the rate of precession of the angle of periastron and a transverse Doppler shift/gravitational redshift measurement can be used to fix the parameters. Alternatively, if the line of sight between the earth and the pulsar passes sufficiently close to the pulsar's orbital companion in inferior conjunction, the pulsed signals will be delayed as they traverse the companion's gravitational potential well. This "Shapiro delay" is also characterized by two parameters. The measure of the rate of advance of periastron parameters and the Shapiro delay parameters will overdetermine the system, providing not just measures of the full seven orbital parameters but also a test of general relativity. An additional measurable quantity in tight binary systems is the decay of the orbit due to gravitational radiation. This quantity has been measured in only one system, that of PSR 1913+16, where it not only confirmed general relativity to be correct but also provided the first experimental evidence for gravitational radiation (Taylor & Weisberg 1989; Taylor *et al.* 1992).

1.6 Projects Undertaken

With so many applications (and many others not described here), it was clear to us that continuing to search for pulsars would be a worthwhile task. We undertook two high-sensitivity searches using the 305 m radio antenna of the National Astronomy and Ionosphere Center at Arecibo, Puerto Rico.

A basic description of pulsar searches is given in chapter 2, and a more detailed description of the specific algorithm we used for searching is in chapter 3. The first of our searches concentrated on an area of the Galactic plane; details can be found in chapter 4. The second survey was performed at high Galactic latitudes; see chapter 5. Two millisecond pulsars were discovered in the course of the surveys. They are described in chapters 6 and 7. A discussion of applications of these pulsars can be found in chapter 8.

Chapter 2

Overview of Pulsar Searching

In this chapter we discuss the factors affecting the observability of pulsars, and we lay the groundwork for a detailed analysis of the sensitivity of the searches discussed in chapters 4 and 5. We pay particular attention to the effects of the unusual design of the 305 m telescope at Arecibo. We conclude with a summary of published untargetted pulsar searches made to date.

2.1 The Nature of Pulsar Signals

Pulsars are detected in the radio regime by their short, broadband pulses of radio energy. Individual pulses of the strongest pulsars can be detected using large radio telescopes. Indeed, pulsars were first discovered as periodic blips on a chart recorder. Studies of individual pulses have shown that, while pulse-to-pulse variations of pulse shapes and intensities for a given pulsar can be large, the shape produced by summing many consecutive pulses is a very stable and reproducible "average profile" (Helfand, Manchester & Taylor 1975).

Individual pulses cannot be detected from weaker pulsars. Only by folding the signal at the pulse period can these pulsars be detected at all. The number of pulses involved in a single observation can be very large: PSR J2019+2425, one of the pulsars found in the survey discussed in chapter 4, was discovered in a measurement that included more than 17,000 pulses.

A well-designed pulsar search maximizes the detected signal from a pulsar while minimizing noise from other sources. If the signal-to-noise ratio (SNR) for the pulsed signal is above a threshold determined by the statistics of the background noise of the search it will be detected; if below, it will be missed.

2.2 Maximizing the Signal-to-Noise Ratio

2.2.1 Signal

Let S be the pulsed flux density per unit frequency arriving at earth from some source. In radio astronomy the standard unit of flux is the Jansky, with 1 Jy = 10^{-26} $\mathrm{Wm^{-2}Hz^{-1}}$. Pulsar fluxes are generally quoted in milliJanskys, with 1mJy being a fairly weak pulsar signal. A telescope receiver converts the radio signals into voltage fluctuations in an electronic circuit. The fluctuations are generally measured in Kelvins, where a 1 K signal is equivalent to the voltage fluctuations (due to Johnson noise) measured across a resistor at temperature 1 K. The telescope gain G, conventionally given in Kelvins per Jansky, provides a direct conversion of source flux density into electronic fluctuations. In practice the input power is detected and integrated over some time period. An observation using two orthogonal polarizations over integration time t and bandwidth B, will have total signal

$$E = SGBtk_B \tag{2.1}$$

where k_B is the Boltzmann constant.

The telescope gain is proportional to the aperture of the telescope: the larger the aperture, the more flux is intercepted, and the higher the gain. At the Arecibo Observatory, the gain varies substantially depending on the zenith angle of the source under observation. This is due to the geometry of the instrument (see figure 2.1.) At low zenith angles (i.e., observing a source directly overhead) the portion of the dish illuminated by the feed (i.e. the part of the telescope actually used) is defined by a circular pattern in the

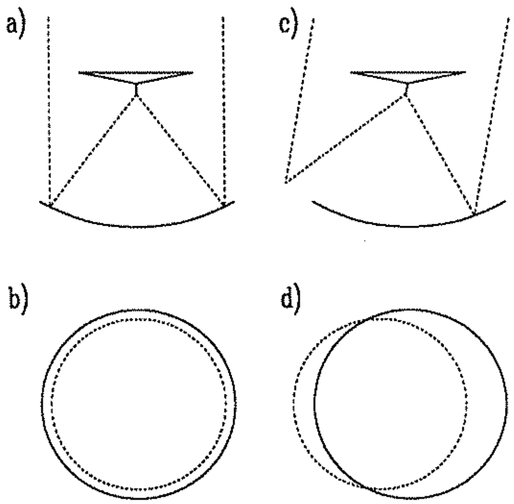

Figure 2.1: Schematic of the geometry of the 430 MHz system at the Arecibo observatory. (a) Side view of an observation of a source at zenith. Parallel rays come down in a vertical direction and are reflected into a feed suspended from the triangular structure. (b) Overhead view of an observation at zenith. The area illuminated by the feed is shown as a broken circle within the reflecting dish (the solid circle.) (c) An observation away from zenith. Some rays at the edge of the illumination pattern are past the edge of the dish. (d) Overhead view of an observation away from zenith. The illuminated circle is partially off the reflecting dish.

center of the dish. As the zenith angle is increased (up to a physical limit of approximately 20°) the area illuminated slowly moves away from the center. As it does so, the edges of this area can overflow the boundary, reducing the gain. In the particular case of the 430 MHz system used in our search programs, the gain as a function of zenith angle z (in degrees) is (NAIC 1989):

$$G(z) = \begin{cases} G_0 & z \leq 3.5^\circ \\ G_0/f(z) & z > 3.5^\circ \end{cases} \tag{2.2}$$

$$f(z) = 0.93464 + 0.01718(z) + 0.00011(z)^2 + 0.00006(z)^3, \tag{2.3}$$

where G_0 is the gain measured at zero zenith angle. In the extreme case of $z = 20°$, we have $f(z) = 1.80$, indicating that only $(1.80)^{-1} = 0.55$ of the illuminated area is intercepting the dish.

2.2.2 Noise

In an ideal universe (for pulsar astronomers at least) variations in detected signal would be due entirely to the amplitude-modulated radio signals emitted by the pulsars themselves. Unfortunately this is not the case. There are at least four distinct sources of undesired radio power ("noise") coupled into the observing system. These are: (1) signals coming from the area of the sky under observation but not related to the pulsar ("sky noise"); (2) signals coming from other directions ("sidelobes"); (3) thermal noise from the ground detected when the illumination pattern falls off the dish ("spillover"); and (4) noise associated with the receiver circuitry ("receiver noise"). Each of these is discussed below.

Noise is quantified as the temperature of a blackbody that would emit at the same intensity as the noise source. The total noise temperature is referred to as the system temperature, T_{sys}. Since noise photons are uncorrelated, the fluctuations in detected voltage from any broadband source in two orthogonal polarizations across bandwidth B integrated over time t is

$$N = k_B T_{\mathrm{sys}} (2Bt)^{1/2}. \tag{2.4}$$

Sky noise varies as a function of observing frequency and position in the celestial sphere. The dominant source of sky noise at the low radio frequencies used in these surveys is synchrotron radiation, which is concentrated along the plane of the Galaxy. Discrete sources, such as the Crab nebula, can also contribute significantly to the noise flux. During our search in the Galactic plane area, the system temperature would quickly rise and fall as the Galactic plane passed overhead, and it was important that our equipment be able to compensate for these changes in flux.

Telescope beam patterns are not perfect. Ideally a telescope would be sensitive to sources in a cone of known dimension projecting outward from the telescope, and signals emitted anywhere within that cone would be detected with a simple sensitivity pattern. Both the laws of physics and the designs of telescopes prevent realization of this goal. Real antenna patterns invariably have sidelobes, areas of illumination far from the main beam. Finally, the physical design of telescopes often requires that cables, supports, receiving equipment, and the like be placed in the main beam, causing additional diffraction effects.

The 430 MHz system at Arecibo has a measured system temperature of 50–70 K at a cold point in the sky with zero zenith angle. The sky contributes approximately 20 K to this figure; the remainder is due to losses in the feed and receiver, and is a constant for all observations independent of telescope pointing. We will refer to this as receiver noise (with temperature $T_{\rm r}$), although it does not all originate within the receiver circuitry.

Most radio telescopes operate by reflecting the incoming flux to a single antenna (called a feed). The feed antenna is connected to electronic receivers which amplify and detect incoming flux. If the illumination pattern of the feed antenna falls off the reflecting dish, a thermal noise flux will be detected from whatever the illumination pattern intercepts. If the geometry is such that the spillover flux comes from the sky, it will act as a noise source with temperature equal to the sky temperature, $T_{\rm sky}$. If the feed's main beam is oriented toward the ground, the spillover noise temperature will equal the ground temperature, typically $T_{\rm gr} \sim 300$ K. As discussed above, the geometry of the Arecibo instrument is such that a large fraction of the area illuminated may be the ground surrounding the reflecting dish. The effect of this on telescope gain was discussed earlier. There is also an effect on system temperature, since flux will be received from the sky and the ground in proportion to the fractions of each illuminated:

$$T_{\rm sys} = \frac{1}{f(z)} T_{\rm sky} + (1 - \frac{1}{f(z)}) T_{\rm gr} + T_{\rm r}, \tag{2.5}$$

where the gain adjustment factor $f(z)$ was defined in equation 2.3. High-zenith-angle observations are hampered in two ways; first, by a reduction in gain; and second, by an increase in noise temperature.

2.2.3 Signal-to-Noise Ratio

Combining equations 2.1 for signal energy E and 2.4 for noise N, the overall signal-to-noise ratio for a continuous signal is

$$\mathrm{SNR} = \frac{E}{N} = \frac{GBt}{T_{\mathrm{sys}}(2Bt)^{1/2}}S = \frac{G(2Bt)^{1/2}}{2T_{\mathrm{sys}}}S. \tag{2.6}$$

If the noise level were known *a priori* it would be a simple matter to calculate the flux density S from a continuously observed source. In practice, however, the noise level is continually varying, and over long time scales these variations are comparable to the signals we are interested in detecting. The noise level must be measured nearly continuously as observations are made. This is most easily done by "chopping" the signal – turning it on and off with a 50% duty cycle, and comparing the radio power in the "on" and "off" states. Frequently radio observations use this technique by repeatedly pointing the telescope on- and off-source. Conveniently, pulsar signals are switched on and off at the source, so for our observations there is no need to switch the telescope. If we consider a signal modulated as a sine wave with amplitude S (instead of having discrete "on" and "off" states), the SNR is reduced by a factor of $2^{1/2}$ relative to an unmodulated signal. This reduction is because the root-mean-square value of the sine-wave modulated signal is $2^{-1/2}S$ rather than S. The sine wave is detected with signal to noise

$$\mathrm{SNR} = \frac{G(Bt)^{1/2}}{2T_{sys}}S. \tag{2.7}$$

We can write the flux over a pulsar period P as $S(t)$, $0 \leq t < P$, in the time domain. Since it is periodic we can also write it as a Fourier series:

$$S(t) = S_0 + \sum_{j=1}^{\infty} S_j\, e^{i(2\pi jt/P+\phi_j)}. \tag{2.8}$$

We will ignore the phases ϕ_j and concentrate on the amplitudes S_j of the harmonic signals. The amplitudes are independent of each other, and equation 2.7 can be applied to each. The resulting SNR measures are summed in quadrature to produce the actual observed SNR:

$$\begin{aligned} \mathrm{SNR}^2 &= \sum_{j=1}^{n_h} \mathrm{SNR}_j^2 & (2.9) \\ &= \sum_{j=1}^{n_h} \left(\frac{G(Bt)^{1/2}}{2T_{sys}} S_j \right)^2 & (2.10) \\ \mathrm{SNR} &= \frac{G(Bt)^{1/2}}{2T_{sys}} \left(\sum_{j=1}^{n_h} S_j^2 \right)^{1/2}, & (2.11) \end{aligned}$$

where we have written the sum over a finite number of measurable harmonics, n_h. Note that the quadrature-sum term in equation 2.11 does not depend on the total pulsar time-averaged flux density S_0 but only on the shape of the pulse as defined by the harmonic coefficients S_j. Continuum signals are not detected in our scheme.

To explore further the implications of the dependence of sensitivity on pulse shape, consider a boxcar pulse shape of unit power and duty cycle w:

$$s(t) = \begin{cases} w^{-1} & 0 \le t < w \\ 0 & w \le t < 1. \end{cases} \qquad (2.12)$$

Parseval's theorem states that

$$\sum_{k=0}^{n-1} |s(k/n)|^2 = \sum_{j=0}^{n-1} |S_j|^2 \qquad (2.13)$$

where we have assumed the unit periodicity of s. The right-hand side of this expression is the square of the pulse-shape factor in equation 2.11. The left-hand side can be approximated by $\int_0^1 dt\, s^2(t) = 1/w$. Substituting into equation 2.11, this gives

$$\mathrm{SNR} \propto w^{-1/2}. \qquad (2.14)$$

In summary, then, for a fixed total flux density, the narrower the width of the pulse, the easier the signal is to detect.

2.3 Interstellar Dispersion

As a radio signal propagates through the interstellar medium, it interacts with free electrons, which slightly reduces the group velocity of the signals. Using the notation of Manchester and Taylor (1977), the velocity v of an electromagnetic wave of frequency ν in a plasma is

$$v = c\left(1 - \frac{\nu_p^2}{\nu^2}\right)^{1/2} \simeq c\left(1 - \frac{1}{2}\frac{\nu_p^2}{\nu^2}\right) \tag{2.15}$$

where we have introduced the plasma frequency

$$\nu_p^2 \equiv \frac{n_e e^2}{\pi m_e} \tag{2.16}$$

and n_e, e, and m_e, are the local number density, charge, and mass of electrons. Signals at frequency ν traveling along path $\int dx$ are delayed relative to a signal traveling at the vacuum propagation velocity by

$$\begin{aligned} t_d &= \int dx\,(\frac{1}{v} - \frac{1}{c}) & (2.17)\\ &= \int dx\,\frac{1}{2}\frac{\nu_p^2}{\nu^2} & (2.18)\\ &= \frac{e^2}{2\pi m_e}\frac{1}{\nu^2}\mathrm{DM} & (2.19)\end{aligned}$$

where we have defined the dispersion measure

$$\mathrm{DM} \equiv \int dx\, n_e. \tag{2.20}$$

The leading constant $e^2/\pi m_e$ is approximately $(2.41 \times 10^{-4})^{-1}$ when DM is in $\mathrm{cm}^{-3}\mathrm{pc}$, ν is in MHz, and t_d is in seconds. Figure 2.2 demonstrates the delay in pulse arrival times at low frequencies.

If the total power is detected in a passband of width $\delta\nu$, a dispersed signal will be smeared due to its differential delays within the band. An estimate of the effect of this smearing can be made by differentiating equation 2.19:

$$\begin{aligned} \delta t_d &= -\frac{e^2}{\pi m_e}\frac{1}{\nu_0^3}\mathrm{DM}\delta\nu & (2.21)\\ &\equiv -\alpha^{-1}\delta\nu, & (2.22)\end{aligned}$$

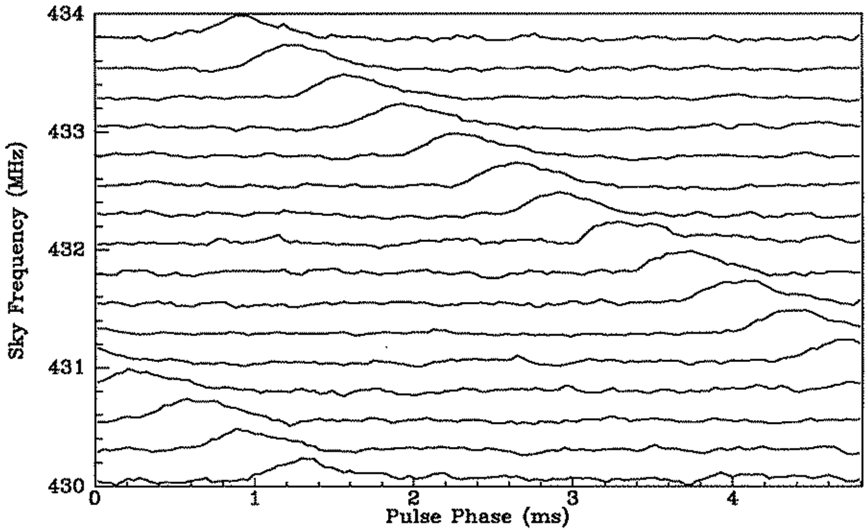

Figure 2.2: Pulse profiles of PSR J2322+2057 in several adjacent frequency bands. The pulse arrives slightly later at lower frequencies due to interstellar dispersion. The pulses are smeared due to differential dispersion delays within each passband.

where α, the "dispersion sweep", is a function of the center frequency ν_0. The smearing can be reduced by using narrow passbands or observing at high frequencies. Since distant pulsars have higher values of DM, their signals will be smeared the most. Dispersion measures as high as 1090 $\mathrm{cm}^{-3}\mathrm{pc}$ have been measured in the direction towards the Galactic center, but more typical numbers are 10 to 500 $\mathrm{cm}^{-3}\mathrm{pc}$ in the Galactic plane. The highest DM for a source within our Galaxy but away from the plane (i.e., with Galactic latitude $|b| > 30°$) is 40 $\mathrm{cm}^{-3}\mathrm{pc}$.

A more precise calculation of the smearing can be made using the exact shape of the passband. Let $a(\nu)$ be the passband transmission function, and assume it is zero except in some relatively small band $|\nu - \nu_0| \ll \nu$ and it is normalized such that $\int_0^\infty d\nu\, a(\nu) = 1$. (This removes some information about the effective total bandwidth of the filter—we include that information in the total bandwidth B.) Equation 2.21 gives the relative delays of signals within the band. If t_0 is the pulse arrival time at the mid-band point ν_0 then the signal of an emitted impulse has the dispersed form across a narrow band

$$\delta(t-t_d)=\delta(t-(t_0+\alpha^{-1}(\nu-\nu_0))) \tag{2.23}$$

in time/frequency space as it arrives at the earth. The observed response to this signal is the convolution of the impulse with the passband shape:

$$\begin{aligned} r_d(t) &= \int d\nu\, a(\nu)\, \delta(t-t_0-\alpha^{-1}(\nu-\nu_0)) && (2.24)\\ &= \alpha\, a(\nu_0+\alpha(t-t_0)). && (2.25)\end{aligned}$$

More generally, the pulsar signal emitted at the source, $S_e(t)$, is convolved with this dispersion-broadening function:

$$S_d(t)=\int dt'\, \alpha\, a(\nu_0+\alpha(t-t'))\, S_e(t'), \tag{2.26}$$

where the "*e*" and "*d*" subscripts denote the emitted and dispersed signals.

2.4 Filtering and Sampling

Interstellar dispersion is not the only source of smearing, so $S_d(t)$ is not the signal that is actually recorded. The signal is smoothed and measured at discrete intervals, which filters out high-frequency elements of the signal in the process. An impulse at time t_0 will affect a measurement at time t with some response function $r_s(t-t_0)$. This too must be convolved with the profile:

$$\begin{aligned} S_{\rm obs}(t) &= \int dt'\, r_s(t-t')\, S_d(t') && (2.27)\\ &= \int dt'\, \alpha\, a(+\alpha(t-t')+\nu_0) \int dt''\, r_s(t'-t'')\, S_e(t''). && (2.28)\end{aligned}$$

These convolutions are more easily analyzed in the Fourier domain. We write $\mathcal{R}$ for the Fourier transform of the instrument response function $r(t)$ and $\mathcal{A}$ for the transform of the normalized passband transmission function $a(\nu)$. Ignoring irrelevant phase changes, the similarity theorem (Bracewell 1965) gives the transform of $a(\alpha t)$ as $\alpha^{-1}\mathcal{A}(\alpha^{-1}f)$. The convolution theorem says that the Fourier transform of a convolution of two functions is the product of the Fourier transforms of those functions. Thus the transmission function of a signal at frequency f is

$$\mathcal{S}_{\rm obs}(f) = \mathcal{A}(\alpha^{-1}f)\mathcal{R}(f)\mathcal{S}_e(f). \tag{2.29}$$

(Note that f refers to the frequency of fluctuations of the envelope of the radio noise, not the radio frequency itself, which we denote by ν.)

Figure 2.3 shows the rapid falloff of $\mathcal{S}_{\rm obs}$ as a function of f for a filterbank-based observing system in which $a(\nu)$ is a wide passband function, and hence its transform $\mathcal{A}(\alpha^{-1}f)$ is a narrow filter.

2.5 The Nyquist Criterion

Attenuation due to dispersion smearing affects only the pulsar signal; the noise flux has no coherent structure across frequency. However, the noise is attenuated due to finite sampling in the same manner as the signal.

The Nyquist theorem states that an observation which samples a signal at some frequency f_s can fully reproduce the signal if it has bandwidth not exceeding $f_n \equiv f_s/2$; f_n is called the Nyquist critical frequency. Signal components with frequencies higher than f_n cannot be distinguished from those below f_n. In fact, these signals are folded around so that a signal with frequency f where $f_n < f < 2f_n$ will be indistinguishable from a signal with frequency $2f_n - f$, a phenomenon referred to as aliasing (Bracewell 1965).

For this reason the noise power observed at frequency $f < f_n$ is the sum in quadrature of noise powers at f, $2f_n - f$, $2f_n + f$, and so on, and (assuming the initial noise spectrum is frequency independent) the observed noise power $N_{\rm obs}$ is

$$N_{\rm obs} \propto \left(\mathcal{R}^2(f) + \sum_{j=1}^{\infty}\left(\mathcal{R}^2(2jf_n - f) + \mathcal{R}^2(2jf_n + f)\right)\right)^{1/2}. \tag{2.30}$$

Combining equations 2.7, 2.29 and 2.30, the signal to noise ratio SNR_j for

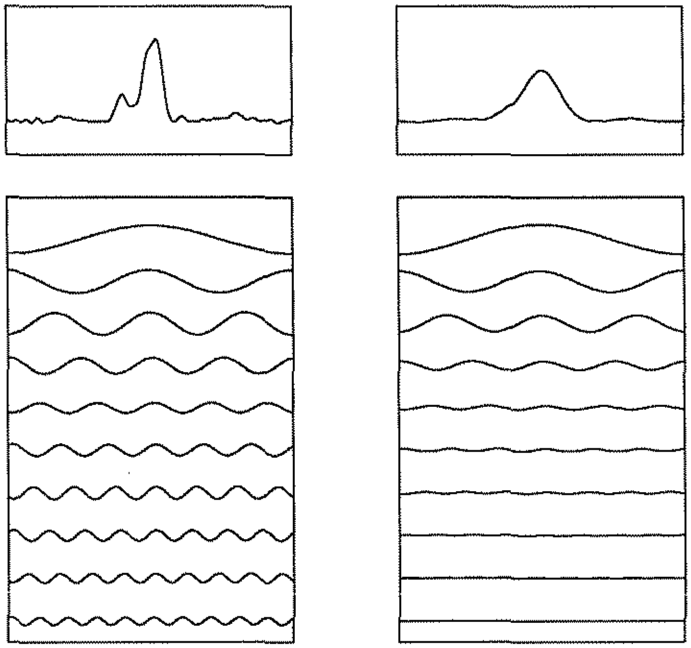

Figure 2.3: Fourier decomposition of pulse profiles. Two profiles of PSR J2019+2425 are shown: the one on the left was taken with coherent de-dispersion hardware, so there is little dispersion smearing; the one on the right was taken with a finite bandwidth filterbank and thus has significant smearing (about 12% of the period in this case). Below each profile are plots of the first 10 harmonics of the Fourier transform of the profile. The rapid falloff in amplitude of the harmonics for the smeared pulsar is evident.

the jth harmonic of a pulsar with period P (i.e., with frequency $f_j = j/P$) is,

$$\mathrm{SNR}_j = \frac{G(Bt)^{1/2}}{2T_{sys}} \frac{\mathcal{A}(\alpha^{-1}f)\mathcal{R}(f_j)}{\left(\mathcal{R}^2(f_j) + \sum_{k=1}^{\infty}\left(\mathcal{R}^2(2kf_n - f_j) + \mathcal{R}^2(2kf_n + f_j)\right)\right)^{1/2}} S_j \tag{2.31}$$

where S_j is the intrinsic pulsar emission in this harmonic as defined in equation 2.8. A measurement involving n_h harmonics would then have an overall signal to noise ratio

$$\mathrm{SNR} = \left(\sum_{j=1}^{n_h} \mathrm{SNR}_j^2\right)^{1/2}. \tag{2.32}$$

2.6 Untargetted Pulsar Surveys

Table 2.1 lists untargetted pulsar searches published to date. Searches in the 1970's were designed under the assumption that the fastest pulsars had periods of order 30 ms, so they were conducted with sample intervals at typically one-half to one-third this period. Since the discovery of the 1.6 ms pulsar PSR 1937+21 in 1982 (Backer *et al.* 1982), surveys have been conducted with faster sampling rates, though not always fast enough to have detected the fastest known pulsars.

Because of its enormous collecting area, the Arecibo Observatory has been the site of the most sensitive surveys. Figure 2.4 shows the portions of the celestial sphere visible with this instrument. Since pulsars are concentrated along the Galactic plane, the region of the plane visible from Arecibo (centered near Galactic longitude $l = 50°$) has received particularly close scrutiny.

Figure 2.5 shows the boundaries of several searches in this area. The UMass-Arecibo survey (Hulse & Taylor 1975) used an 8 MHz passband centered at 430 MHz and collected data for more than two minutes at each position observed. This survey remains the most sensitive ever undertaken for slow pulsars, but due to its slow sample rate it was not sensitive to millisecond pulsars. Nevertheless, among the 40 pulsars found was the recycled binary PSR 1913+16, the first such object discovered. Segelstein *et al.* (1986; see also Stokes *et al.* 1986) surveyed this area again, with a much faster sample rate but with a bandwidth slightly under 1 MHz. Since this survey was much less sensitive to slow pulsars than the UMass-Arecibo survey, it found only four new slow pulsars, but it also found one new millisecond pulsar, PSR 1855+09.

Much of this region was observed in the Jodrell Bank "B" and "C" surveys. These projects were undertaken at relatively high frequencies, 610 to 1400 MHz, and were significantly lower in sensitivity than those undertaken at Arecibo. Although these surveys discovered many new pulsars, none were within the range of sky accessible from the Arecibo telescope.

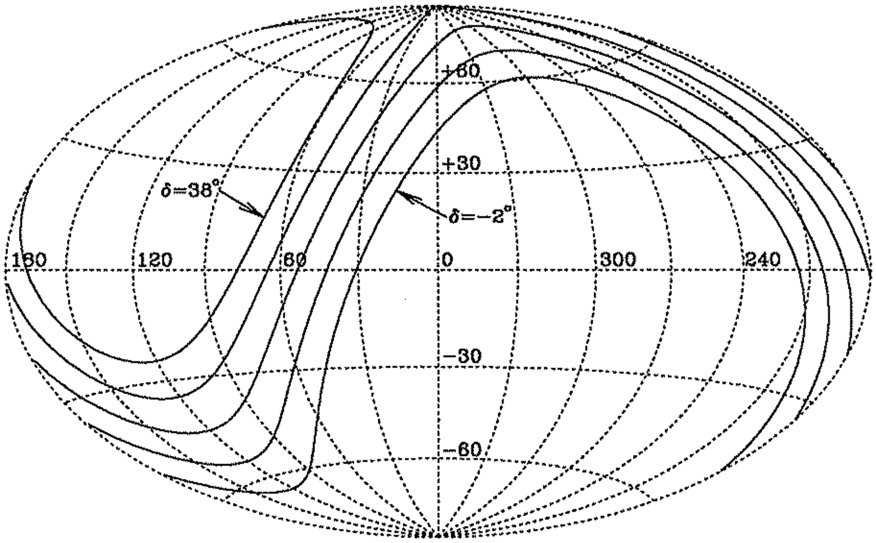

Figure 2.4: The sky visible from Arecibo in Galactic coordinates. Lines of constant declination are shown at declinations −2°, +8°, +18°, +28°, and +38°. The outermost lines are the absolute pointing limits of the telescope; the most sensitive observations can be made in the strip around declination +18°, which transits overhead. Sensitivity falls off rapidly as a function of zenith angle.

The most recent effort to survey the Galactic plane from Arecibo was begun in 1986 (Fruchter 1989) and completed as part of this thesis. Newly available data acquisition equipment allowed use of the full 10 MHz passband available at 430 MHz while sampling as fast as 516 μs, making much deeper searches for millisecond pulsars possible. Chapter 4 describes this search in detail.

As the Galactic plane search progressed, it became clear that recycled field pulsars observable with current equipment were nearby objects and therefore would not be concentrated along the Galactic plane. This conjecture was confirmed by the discovery of two millisecond pulsars at high Galactic latitudes by Wolszczan (1991). For these reasons, we undertook survey at high Galactic latitudes, using somewhat different data acquisition equipment, which allowed a faster sampling rate of 250 μs. This survey is discussed in chapter 5.

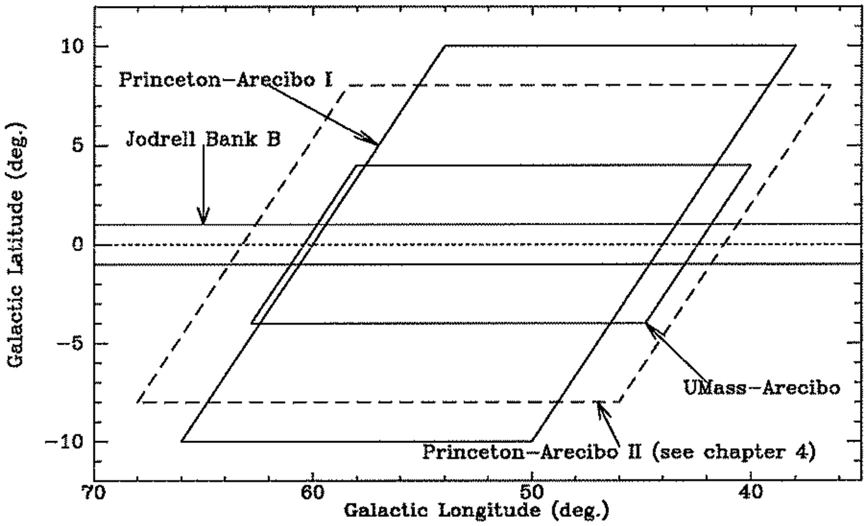

Figure 2.5: Surveys of the portion of the Galactic plane visible from the Arecibo Observatory. Much of the sky in the range $-6° < b < 6°$ was also observed in the Jodrell Bank C survey. Parameters of the surveys are discussed in the text and in table 2.1; the Princeton-Arecibo II survey is discussed in chapter 4.

Table 2.1: Published field pulsar surveys. The center observing frequency is ν. The interval between samples is t_s; generally the analog signals were low-pass-filtered at 1.5 to 2.0 times this value before sampling. $S_{\rm min}$ is the minimal detected flux for a low duty cycle, slow pulsar, in a typical beam area. The flux value quoted for a search is for the observing frequency used during that search.

Search (Reference)	ν (MHz)	t_s (ms)	$S_{\rm min}$ (mJy)	Area (deg^2)	Notes
UMass-Arecibo	430	16.7	1	24	A
(Hulse & Taylor 1974, 1975)				140	G
UMass-NRAO (Damashek, Taylor & Hulse 1978)	400	16.7	10	12500	N
Molonglo I	408				M
(Large & Vaughan 1971)					
Molonglo II	408	10.0	15	27000	S
(Manchester *et al.* 1978)					
Molonglo III	843	0.5	8	200	GS
(D'Amico *et al.* 1988)					
Princeton-NRAO II	390	2.2	3	3725	N
(Stokes *et al.* 1986)					
Princeton-Arecibo I	430	0.4	2	289	G
(Stokes *et al.* 1986)					
Jodrell Bank A (Davies, Lyne & Seiradakis 1977)	408	40.0	10	3000	
Jodrell Bank B	1400	2.0	1	200	GN
(Clifton *et al.* 1992)					
Jodrell Bank C	1400	0.3	40		GN
(Biggs & Lyne 1992)	928	0.3	74	1500	
	610	0.4	97		
Parkes	1500	0.3	2.5	800	GS
(Johnston 1990)		1.2	1.0		
Princeton-Arecibo II	430	0.5	2	235	GN
(Fruchter 1989; chapter 4)					
Princeton-Arecibo III	430	0.25	0.7	170	N
(chapter 5)					

Notes: A. Galactic anti-center. G. Galactic plane. M. Much of the southern sky covered with a variety of hardware setups. N. Northern sky. S. Southern sky.

Chapter 3

The Search Algorithm and Software

As the data acquisition hardware in the two searches differed somewhat, detailed sensitivity calculations will be relegated to separate chapters. The software used to search the data for pulsars was nearly identical, however; it is described in generic terms here.

The data take the form of a matrix of power measurements taken at regular intervals in many adjacent narrow-bandwidth frequency channels. Specifically, we define n_{chan} to be the number of frequency channels, n_{sam} to be the number of time samples taken for each channel, and t_s be the time interval between samples. We further define ν_0 to be the center frequency of the band under observation, and $\delta\nu$ to be the spacing of the frequency channels (and also the approximate width of a single channel). The high-latitude search data was in this matrix form when collected. Because the Galactic plane data was collected with an autocorrelation spectrometer rather than a filterbank, it needed some manipulation to transform it into the time–frequency matrix form (see section 4.1.)

Nearly all the data reduction was done using the Cray Y-MP computer system of the Pittsburgh Supercomputer Center. Overall processing time was about 60 seconds of CPU time per beam area for the Galactic plane search and 20 seconds per beam area for the high latitude search, using a single processor on the Y-MP. The average computational rate achieved by the code was nearly 10^8 floating-point operations per second, and the total number of floating-point instructions executed was of order 10^{14}.

3.1 Dispersion Removal

The data processing algorithm can be divided into two major steps: first, de-dispersed time series are created at various assumed dispersion measures (DM's); second, these time series are searched for periodicities.

The de-dispersion procedure is performed on short subsets (in time) of the data. Long-term drifts in measured flux level are removed in parallel with the de-dispersion. The data are stored on magnetic tape as consecutive blocks of 256 or 512 time samples by n_{chan} frequency channels. A sufficient number of these blocks is retrieved to cover approximately 500 ms. (The actual times were 529 ms and 512 ms for the plane and high-latitude surveys, respectively.) Within this data subset, measurements in each frequency channel are normalized by removing any constant offset and scaling such that the root-mean-square value is one. This normalization procedure acts as a high-pass filter, attenuating signals with a time constant of ~ 500 ms. Such filtering is necessary to eliminate slow drifts in the signals, but it has the side effect of reducing sensitivity to wide, long-period pulsar signals. Fortunately most pulsars have relatively narrow pulse widths, so the pulsar signal variation is relatively fast, usually well under 500 ms even for pulsars with periods over 500 ms. Thus pulsar signals are only minimally affected.

After filtering, the normalized subset of data is used to generate numerous de-dispersed time series at various assumed dispersion constants. In the first iteration of this process, $2n_{\mathrm{chan}}$ time-series are created, corresponding to $2n_{\mathrm{chan}}$ different trial DM's. Equation 2.21 gives the differential dispersion delay between two frequencies near our nominal frequency ν_0:

$$\delta t_d = \alpha^{-1}(\nu_1 - \nu_2), \tag{3.1}$$

$$\alpha^{-1} = \frac{e^2}{\pi m_e}\frac{\mathrm{DM}}{\nu_o^3}. \tag{3.2}$$

For fixed DM there is a linear delay δt_d as a function of frequency offset $(\nu_1 - \nu_2)$.

To produce a time series for some assumed DM, data in each frequency channel are shifted by an amount proportional to the difference between the channel frequency and the standard frequency ν_0, and the shifted channels are summed. This procedure is performed with DM values

$$\mathrm{DM} = \frac{\pi m_e}{e^2}\frac{\nu_0^3}{B}t_s M \tag{3.3}$$

where $B = n_{\mathrm{chan}}\delta\nu$ is the total bandwidth and M takes on all integer values from 0 to $2n_{\mathrm{chan}}-1$.

The $M = 0$ time series is equivalent to summing data points from each of the frequency channels at the same time sample; the $M = 1$ time-series is equivalent to the highest and lowest channels having a relative time offset of one sample period, t_s; and so on up to $M = 2n_{\mathrm{chan}}-1$, where the highest and lowest series are offset by almost $2n_{\mathrm{chan}}$ time samples.

At $M = n_{\mathrm{chan}}$, dispersion smearing within a single channel is the same as the sample time. For $M \gg n_{\mathrm{chan}}$, dispersion smearing is the dominant source of signal attenuation, and the time resolution of the data can be reduced without loss of sensitivity. For analysis at higher dispersion measures, adjacent time samples are added in each frequency channel, reducing the size of the data matrix by a factor of two without loss of information. The de-dispersion procedure is now repeated on the new, coarser data, resulting in de-dispersed series with channel-to-channel offsets from two to four time samples, twice the DM limit of the first pass. This process is iterated up to whatever DM limit is desired; specifics will be given in later chapters.

The linear approximation in equation 2.21 isn't sufficiently accurate for the high-frequency-resolution data of the plane search. To introduce a slight curvature in $\delta t_d(\nu)$, the time/frequency data matrix is doubled in size in the frequency dimension with alternate frequency channels filled with zeros. Nonzero channels are then shifted up and down slightly, effectively changing their apparent frequency, to allow use of the linear formula. As an added benefit, the double-size matrix is a computational convenience in the de-dispersion algorithm.

The de-dispersion calculation is performed by the "Tree" algorithm, a highly efficient scheme that processes the full data block at once and avoids redundant arithmetic, requiring only order $n_{\rm chan} \log n_{\rm chan}$ operations per time sample to create the de-dispersed time series (Taylor 1974). Because a de-dispersed time-series of length t necessarily contains information collected over a time-span longer than t, we retain some information from each data block to be used in processing the next block. In the high-latitude search, an extra data block was processed before the main data series to be used in de-dispersing the first block of the main series. In the Galactic plane survey, zero-padding was used where necessary.

Since the entire de-dispersed data set must be accumulated before the search for periodic signals can begin, it is advantageous to store it as efficiently as possible. The de-dispersed time series are therefore compressed to 2-bit numbers. This has little effect on data dominated by noise; if the pulsed signal is strong, its apparent strength will be reduced somewhat, but never so much as to put it below the detection threshold.

3.2 Search for Periodic Signals

The de-dispersion process generates a large number of long time series each of which is independently analyzed for periodicities. In both surveys the longest time series had $n_{\rm sam} = 131,072 = 2^{17}$ data samples, with shorter series at large DM's. The exclusive use of data series with lengths equal to powers of two allows the use of the most efficient fast Fourier transform routine in the spectral analysis of the signals.

A Fourier transform of the n_{sam}-element time series is taken, resulting in an array of $n_{\mathrm{sam}}/2$ complex Fourier coefficients. Amplitudes of the complex coefficients are calculated, resulting in a voltage fluctuation spectrum with $n_{\mathrm{sam}}/2$ elements.

Next, known interference sources are removed from the Fourier series and power spectrum. The most common source of interference is the commercial power line signal, nominally 60 Hz. To remove it, the $\mathrm{DM} = 0$ power spectrum is searched between 59.75 and 60.25 Hz to find the actual frequency of the power line. All bins of all spectra within 0.3% of the 60 Hz line are zeroed, as are bins within 0.3% of higher harmonics (120 Hz, 180 Hz, etc.). In the high latitude survey, this zeroing was expanded to 0.9% around the 60 Hz fundamental. In both cases empirical examinations of test data determined the sizes of the zeroed regions. Several other known interference sources are also excised at this point. In general the sources of interference were not known, but repeated detection of a periodic signal at different telescope pointing positions identified the periodicity as interference. Tables of the excised periods are given in chapters 4 and 5. In all cases of interference excision, the appropriate complex Fourier coefficients are zeroed along with the power spectrum bins.

Because of aliased noise power around the Nyquist frequency, the power spectrum has larger amplitudes in its highest-frequency bins. To remove this bias, the spectrum is divided into 64 subsets and each part scaled by its average value, with the average itself removed. The complex Fourier coefficients are similarly normalized. After this flattening has been done the entire spectrum is rescaled to a root-mean-square value of one.

Finally the search for periodic signals begins. First, the power spectrum is searched for peaks. The highest-valued 0.2% of the bins of the spectrum are recorded, and measures of the power are made at frequencies 1/2 bin above and below these peaks (as well as at the peaks themselves). The 1/2-bin-offset measures are made by interpolating the complex Fourier coefficients. The parameters of the single highest peak measured are stored by the software.

In section 2.5, we discussed the decomposition of a profile into Fourier components. The search just described is equivalent to searching for the strongest single harmonic component in the data and ignoring the remaining parts of the pulsar signal. For pulsars with narrow pulse profiles and rotation frequencies lower than the Nyquist rate one can do much better by combining signals from harmonically related spectral bins, that is, bins in the power spectrum with integer ratios of bin numbers.

For this reason we analyze combinations of two, three, four, eight, and sixteen harmonically related signals. Each combination is analyzed separately, since the maximum sensitivity to a pulsar signal depends on its shape and will not necessarily be found using the maximum number of harmonics available. First the amplitudes of the fundamental and higher harmonics are summed by adding the nearest appropriate low-frequency power bins to the highest harmonic in a series; no interpolation is done at this stage. For trial frequency f the harmonic frequencies are f, $2f$, and so on up to $n_h f$, where n_h is the number of harmonics used. To satisfy the Nyquist criterion we must have $n_h f < f_n = 1/2t_s$, so the maximum detectable frequency in data analyzed with n_h harmonics is $(2n_h t_s)^{-1}$.

The summed-harmonic spectra are searched for peaks. Again the strongest 0.2% of the bins in each spectrum are recorded and analyzed in more detail. Since complex Fourier coefficients of the multiple harmonics are available, we do more than just sum the spectral amplitudes. By back-transforming the complex Fourier coefficients (interpolating as necessary), time-domain pulse profiles are generated, whose signal-to-noise figures can be calculated. The back-transform analysis is done in two stages. In the first stage, the number of harmonics used is the same as the number used to generate the power spectrum itself (n_h), so $2n_h$-point pulse profiles are produced in the time domain. Signal strengths for these profiles are measured by calculating the maximum signal in a single bin of the profile or shared by two adjacent bins. For $n_h > 4$, the three strongest candidates thus measured are analyzed further: new profiles are generated by using up to $2n_h$ complex Fourier coefficients, if available. (At the highest fundamental frequencies, the higher harmonics will be unavailable

Table 3.1: Nominal limits of the searches. The sample interval, t_s, was 516 μs in the plane search and 250 μs in the high-latitude search. The integration time, $t_{\rm int}$, was 32.768 s and 67.715 s, respectively, in the two searches.

n_h	P_{min}	P_{max}
1	$2t_s$	$(63/64)\ t_{\rm int}$
2	$4t_s$	80 ms
3	$6t_s$	80 ms
4	$9t_s$	150 ms
8	$16t_s$	150 ms
16	$32t_s$	2500 ms

due to Nyquist considerations.) The new profiles have double the resolution of the original one. The signal strengths within these profiles are calculated by numerically integrating power around the peak (allowing up to 25% duty cycle for the pulsar signal) and calculating the noise level in the profile using off-peak data. Profiles are also generated and analyzed at frequencies spaced 1/2 bin away from the highest harmonic of the original peak in the power spectrum. Parameters are retained for the strongest candidate found with each combination of harmonics.

Six candidates are found for each trial DM: the strongest signals for each of $n_h = 1, 2, 3, 4, 8$, and 16. The time series for all DM's with the same length ($n_{\rm sam}$) are processed; in the end, information is retained only about the top candidate in each combination of harmonics for a set of DM's. Parameters of these candidates are saved, along with time-domain profiles for $n_h > 1$ candidates and small slices of the power spectra for $n_h = 1$ candidates. A sample of output from the computer code is given in figure 3.1.

Table 3.1 lists the nominal minimum and maximum period allowed in our search program as a function of number of harmonics in use. The minimum period is determined by the Nyquist criterion. The maximum periods were chosen to maximize sensitivity to fast pulsars and to reduce our susceptibility

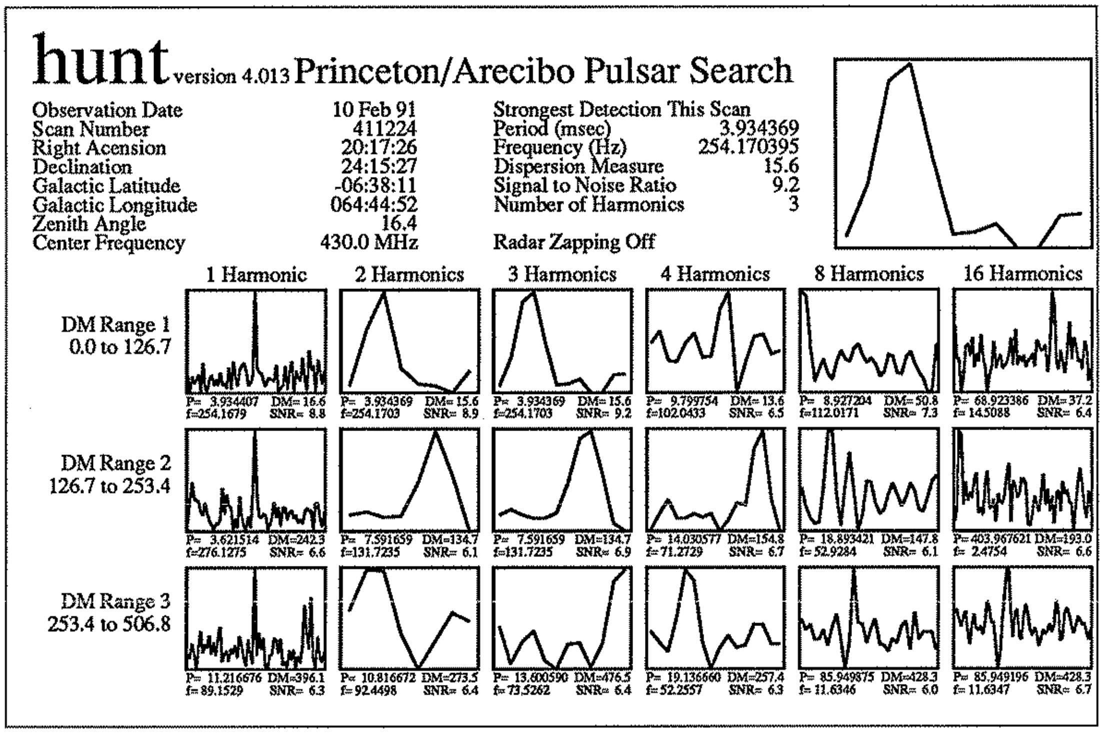

```
hunt version 4.013 Princeton/Arecibo Pulsar Search
Observation Date          10 Feb 91    Strongest Detection This Scan
Scan Number                  411224    Period (msec)             3.934369
Right Acension             20:17:26    Frequency (Hz)          254.170395
Declination                24:15:27    Dispersion Measure            15.6
Galactic Latitude         -06:38:11    Signal to Noise Ratio          9.2
Galactic Longitude        064:44:52    Number of Harmonics              3
Zenith Angle                   16.4
Center Frequency          430.0 MHz    Radar Zapping Off
```

```
DM Range 1 0.0 to 126.7
1 Harmonic:   P= 3.934407 DM= 16.6   f=254.1679 SNR= 8.8
2 Harmonics:  P= 3.934369 DM= 15.6   f=254.1703 SNR= 8.9
3 Harmonics:  P= 3.934369 DM= 15.6   f=254.1703 SNR= 9.2
4 Harmonics:  P= 9.799754 DM= 13.6   f=102.0433 SNR= 6.5
8 Harmonics:  P= 8.927204 DM= 50.8   f=112.0171 SNR= 7.3
16 Harmonics: P= 68.923386 DM= 37.2  f= 14.5088 SNR= 6.4

DM Range 2 126.7 to 253.4
1 Harmonic:   P= 3.621514 DM=242.3   f=276.1275 SNR= 6.6
2 Harmonics:  P= 7.591659 DM=134.7   f=131.7235 SNR= 6.1
3 Harmonics:  P= 7.591659 DM=134.7   f=131.7235 SNR= 6.9
4 Harmonics:  P= 14.030577 DM=154.8  f= 71.2729 SNR= 6.7
8 Harmonics:  P= 18.893421 DM=147.8  f= 52.9284 SNR= 6.1
16 Harmonics: P=403.967621 DM=193.0  f= 2.4754 SNR= 6.6

DM Range 3 253.4 to 506.8
1 Harmonic:   P= 11.216676 DM=396.1  f= 89.1529 SNR= 6.3
2 Harmonics:  P= 10.816672 DM=273.5  f= 92.4498 SNR= 6.4
3 Harmonics:  P= 13.600590 DM=476.5  f= 73.5262 SNR= 6.4
4 Harmonics:  P= 19.136660 DM=257.4  f= 52.2557 SNR= 6.3
8 Harmonics:  P= 85.949875 DM=428.3  f= 11.6346 SNR= 6.0
16 Harmonics: P= 85.949196 DM=428.3  f= 11.6347 SNR= 6.7
```

Figure 3.1: Sample search software output. The strongest candidate pulsar signal in each of several DM ranges and several combinations of harmonics is displayed. The "1 Harmonic" plots show a small slice of the power spectrum around the strongest peak; plots in the remaining columns show time-domain candidate profiles. The plot at the top shows the strongest overall detection in this scan.

to slowly varying noise. A sufficiently strong pulsar could be found beyond these limits on either end of the scale. At the fast end, a one-harmonic signal could be aliased as a signal below the Nyquist frequency. At the slow end, a higher harmonic of the pulsar could be detected and interpreted as the fundamental frequency. The latter possibility occurred with the discovery of the 5.094 s pulsar PSR J1951+11 in the Galactic plane search.

Chapter 4

The Galactic Plane Survey

The second Princeton-Arecibo pulsar survey, a search program oriented towards the Galactic plane and optimized for millisecond pulsar detection, was begun in 1986. Results of the first phase of the survey can be found in Fruchter (1989). Results of the second phase are discussed here.

4.1 Hardware and Sensitivity

The most straightforward method of producing the narrow channels necessary to reduce dispersion smearing is through the use of a filterbank, a set of many narrow radio frequency filters, each tuned to a slightly different frequency. While such circuits are conceptually simple, they are not very flexible, and they become quite cumbersome as the number of channels increases. For the Galactic plane search, a filterbank with more than one hundred channels would have been necessary to span the 10 MHz available bandwidth with sufficient resolution to avoid smearing the signal from a 1 ms pulsar with a DM of order 100. No such filterbank is available at Arecibo, and the construction of a new one at Princeton seemed impractical.

Instead, the Arecibo-Berkeley 40 MHz correlator was used for data acquisition. This instrument analyzes radio frequency signals by digitizing and cross-correlating them. (40 MHz refers to an internal clock frequency.) For our search, the correlator was configured to produce autocorrelation functions for four 2.5 MHz subsets of each of two 10 MHz passbands in two orthogonal circular polarizations. Some relevant details of autocorrelation spectroscopy and this instrument are given in appendix A. Each 2.5 MHz passband was three-level sampled at 10 MHz, twice the Nyquist rate, and correlated with itself for 64 lags. Individual autocorrelations were accumulated for a period of $t_s = 516.625\ \mu\text{s}$. Since the incoming radio signals were largely random noise (with a slowly-varying envelope), all but the zero lag were uncorrelated from one sample to the next. The digitization level was set to optimize SNR for these uncorrelated lags. A separate measure of the total power (in principle equal to the zero lag of an autocorrelation, but without the effects of low-resolution digitization) was made using an independent high-resolution power counter in each passband. The double-Nyquist sampling partially compensated for the coarse three-level digitization, but half of the resulting 64 lags were redundant, so only 32 lags were retained for further processing.

The autocorrelation lags from opposite polarizations were summed, scaled and written to magnetic tape, as were the power counter values. When the data were later read from tape during processing, the power counter measures were scaled and substituted for the zero lag. A cosine transform was then performed, creating a filterbank-style time/frequency data matrix from the autocorrelation data. This data matrix was then analyzed using the algorithm outlined in chapter 3.

The telescope tracked a particular point on the sky during a scan and slewed to the next point between scans. Within a scan, a total of $2^{17} = 131,072$ adjacent spectra were collected, one every 516.625 μs, for an observing time of 67.715 s. The threshold levels of the digitizing circuit were reset before the start of each scan to allow for changes in system temperature.

The nominal bandwidth $\delta\nu$ of frequency channels after processing was 78.125 kHz, so dispersion smearing within individual channels was of order

$$t_d = (e^2/2\pi m_e)\mathrm{DM}\,\delta\nu\,\nu^{-3} \sim 8.15\mu s \times \mathrm{DM}, \tag{4.1}$$

with DM in $\mathrm{cm}^{-3}\mathrm{pc}$. For $\mathrm{DM} < 63$, the dispersion smearing time scale t_d was less than the sampling time $t_s = 516.625\ \mu\mathrm{s}$, and the finite sampling rate was the dominant source of pulse smearing and the limiting factor in detecting the fastest pulsars. Conversely, for $\mathrm{DM} > 63$, dispersion smearing dominated the effective time resolution.

We can use equations 2.31 and 2.32 to make a more quantitative analysis of the sensitivity of this search:

$$\mathrm{SNR}_j = \frac{G(Bt)^{1/2}}{2T_{sys}} \frac{\mathcal{A}(\alpha^{-1}f_j)\mathcal{R}(f_j)}{\left(\mathcal{R}^2(f_j) + \sum_{k=1}^{\infty}\left(\mathcal{R}^2(2kf_n - f_j) + \mathcal{R}^2(2kf_n + f_j)\right)\right)^{1/2}} S_j \tag{4.2}$$

$$\mathrm{SNR} = \left(\sum_{j=1}^{n_h} \mathrm{SNR}_j^2\right)^{1/2} \tag{4.3}$$

where S_j is the signal strength of the jth harmonic (with frequency $f_j = j/P$, where P is the pulsar period), n_h is the number of harmonics used in the data processing, $f_n = 1/2t_s$ is the Nyquist frequency, and $\mathcal{A}$ and $\mathcal{R}$ are the Fourier transforms of the passband shape and the sampling function.

In appendix A, we show that for the autocorrelator

$$\mathcal{R}(f) = \mathrm{sinc}(ft_s) \tag{4.4}$$

$$\mathcal{A}(f) = \Lambda(\delta\nu\, f) \tag{4.5}$$

where

$$\mathrm{sinc}(x) \equiv \sin(\pi x)/\pi x \tag{4.6}$$

$$\Lambda(x) \equiv \begin{cases} 1 - |x| & |x| < 1 \\ 0 & \text{elsewhere.} \end{cases} \tag{4.7}$$

The factors in front of S_j in equation 4.2 can be divided into two parts: the first group depends only on observatory and feed characteristics, and does not include attenuation due to finite sampling rate and finite bandwidth filters. The second group of factors depend on the filtering of the signal by the interstellar medium and the data collection system. We divide the analysis of sensitivity between these two sets of factors.

The maximum gain of the 430 MHz system at Arecibo is 19.7 K/Jy. The gain falls off quickly as a function of frequency, though, and the average gain (at zero zenith angle) across the 10 MHz passband used in this survey was 14.9 K/Jy (NAIC 1989). Integration time for each beam area was $t_s = 67.715$ s, and the bandwidth used was $B = 10$ MHz. The system temperature T_{sys} depends on zenith angle and sky temperature, and varied from 60 K to over 200 K in our observations. Substituting these values into equation 4.2 and assuming a minimum system temperature of 60 K gives 3.3 mJy^{-1} as the first factor in the SNR_j expression. For slow pulsars the second factor in the equation is approximately one, so we have $\mathrm{SNR}_j = 3.3\ \mathrm{mJy}^{-1} S_j$. In appendix B we show that noise fluctuations up to SNR ~ 8 are expected, so a sine wave signal of amplitude $S_j = 2.5$ mJy or more would produce a SNR over the detection threshold. Since the signal-to-noise ratio grows with the square root of the number of harmonics in use, the minimum detectable flux for a slow pulsar with 16 equal-strength harmonics and a minimal system temperature would be 0.6 mJy.

Substantial variations in system temperature and zenith angle caused significant reductions in sensitivity for some beam areas. The sky position and zenith angle for each data scan are known, so the sky temperature, antenna gain, and system temperature can be calculated. We calculated the reduction in sensitivity due to these effects for each beam area of the second phase of this survey, using the 408 MHz map of Haslam *et al.* (1982) for sky temperature estimates, and incorporating the dependence of gain and system temperature on zenith angle as described in chapter 2. A histogram showing the distribution of reduced sensitivity due to these effects is given in figure 4.1. Similar statistics for the first phase of the search are given in Fruchter (1989).

The second term in equation 4.2 describes in detail the dependence of sensitivity on pulsar rotation frequency f and dispersion measure DM due to pulse smearing by the interstellar medium and the data acquisition system. The attenuation of detectable flux due to these effects for several values of DM is plotted in figure 4.2. In the figure it is assumed that the intrinsic

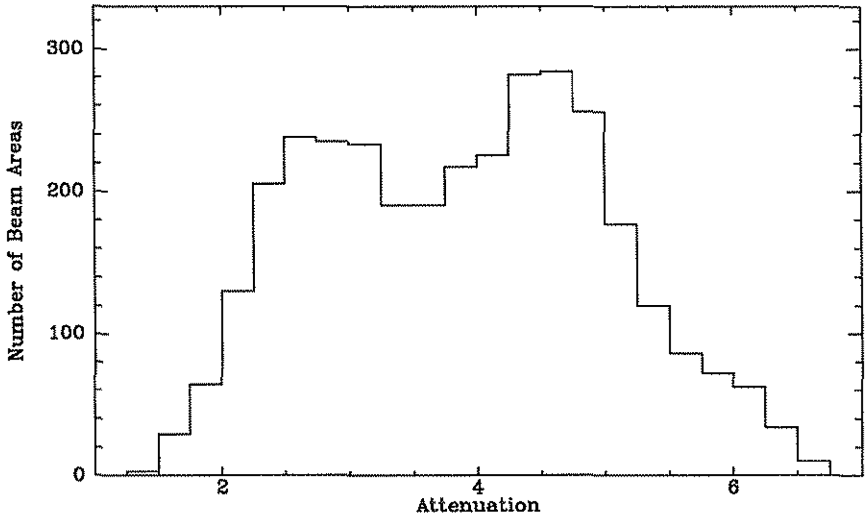

Figure 4.1: Distribution of reduction in sensitivity due to system temperatures above 60K and zenith angles above 3.5°. Details of these effects are discussed in chapter 2. All beam areas successfully processed in the second phase of the Galactic plane survey are included.

flux emitted by the pulsar is the same in each of the first sixteen harmonics (equivalent to a duty cycle of no more than 6% $\sim 1/16$.) The discrete jumps in the sensitivity curve occur at transition points where the number of usable harmonics changes.

4.2 Sky Coverage

A rectangular grid was searched with $9' \times 9'$ separation between pointing positions. This spacing is approximately the telescope half-power beam width at 430 MHz. The grid was defined in 1987.0 coordinates to allow for the possibility of switching to constant-declination, drift-mode searches, although this mode was never implemented during the Galactic plane survey. Grid points had coordinates right ascension $\alpha(1987.0) = 18^h21^m00^s + (38^s)n_\alpha$ and declination $\delta(1987.0) = +0°04'.5 + (9'.0)n_\delta$ where n_α and n_δ are integers. The

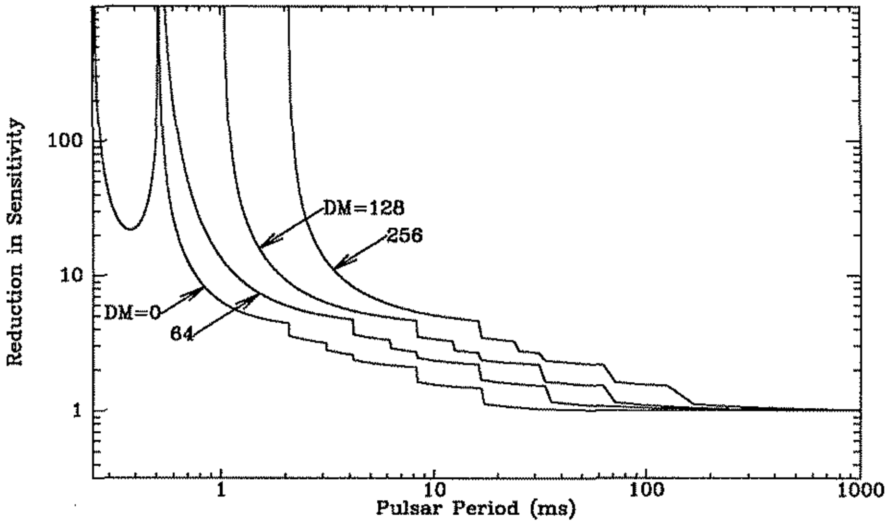

Figure 4.2: Reduction in sensitivity to short-period pulsars for several values of dispersion measure. Discrete jumps in the sensitivity are points where the number of harmonics used in the search changes (see chapter 3.) Base sensitivity (equal to 1 on the y-axis above) is about 0.6 mJy for observations with optimal sky temperature and zenith angle. The search was completely insensitive to pulsars at the sample period of 516.625 μs and its harmonics.

separation between points was fixed in right ascension at 38^s (approximately $9'$ on the sky at $\delta = 18°40'$, the center of Arecibo's range), so the density of beam areas on the sky was slightly higher at higher declinations and lower at lower declinations.

Specific points from the grid were chosen for observation in the second phase of the survey using several criteria. Points successfully observed in the first phase of the survey were not re-observed. All points observed were within eight degrees of the Galactic plane ($|b| < 8°$). Zenith angle was minimized by selecting points relatively close to declination $\delta = 18°40'$. Consecutive observations generally included adjacent grid points by following rows of constant declination on the grid or dithering between two adjacent rows. Telescope scheduling also affected the sky coverage—some portions of the $|b| < 8°$ region were visible earlier (or later) than other portions and thus were observed more often, although individual points were never re-observed. Observing sessions were always begun on a test source, usually PSR B1737+13, to verify equipment operation.

A substantial amount of observation time was lost due to radio frequency interference. The 430 MHz band is allocated to navigation purposes, and radar signals from naval vessels frequently contaminated the passband. (The observatory is approximately 10 km from the Atlantic Ocean, and there is an unblocked line of sight between the antenna platform and the ocean.) The radar signals were modulated at several periods from 1 ms to 10 s—disastrous for pulsar searches—and frequently covered a large portion of the passband. Although there was an attempt to remove these signals during the first phase of the search (Fruchter 1989), we found the situation nearly hopeless, and in the end data contaminated by this interference were not used.

A total of 5540 unique pointings were made, including calibration sources. Of these 3342 were successfully processed, interference-free search points. Since the sky area of each point was a circle of diameter 9′, the total sky coverage was approximately 75 square degrees. The points observed in the second phase of the survey are shown in figure 4.3. The first phase covered about 7200 beam areas, or 160 square degrees (Fruchter 1989); thus the entire survey encompassed approximately 235 square degrees. A map of all points surveyed in both phases is given in figure 4.4. The distribution of points in Galactic latitude is given in figure 4.5.

4.3 Results

The data were processed as described in chapter 3. Time series of 131,072 points were searched for periodicities at DM's from 0 to 128 $\mathrm{cm}^{-3}\mathrm{pc}$ stepping at intervals of approximately 0.5 $\mathrm{cm}^{-3}\mathrm{pc}$. Adjacent data points were summed, and the resulting 65,536-bin series were searched at DM's at integer intervals from 128 to 256 $\mathrm{cm}^{-3}\mathrm{pc}$; the data series were compressed once more, and the

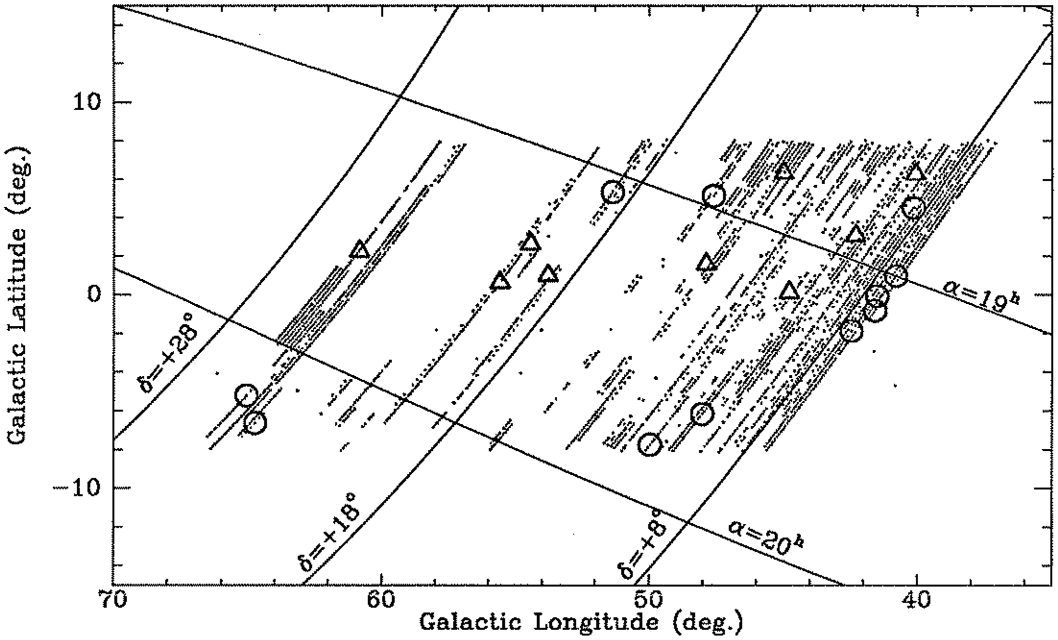

Figure 4.3: Sky coverage of the second phase of the Princeton-Arecibo II survey. Dots are successfully processed beam areas; circles are newly discovered pulsars; triangles are previously discovered pulsars detected in the survey.

remaining 32,768-bin series were searched at intervals of 2 $\mathrm{cm}^{-3}\mathrm{pc}$ between 256 and 512 $\mathrm{cm}^{-3}\mathrm{pc}$. A large number of candidate periods were disallowed due to repeated detection of interference; the ranges excised are listed in table 4.1.

Seven known pulsars had catalog positions within the nominal half-width of the telescope's main beam, $5'$, of search pointing positions. Five of these were detected and two were not. An additional four pulsars, including one millisecond object (PSR B1855+09), were detected despite distances greater than $5'$ from the beam center. These detections were largely possible because of the great intrinsic strength of these pulsars; however, the uncertainty in some of the cataloged positions is of order $5'$ (because they are known only from Arecibo pointing measures at 430 MHz) so the actual distances to the beam center may differ slightly from our calculations.

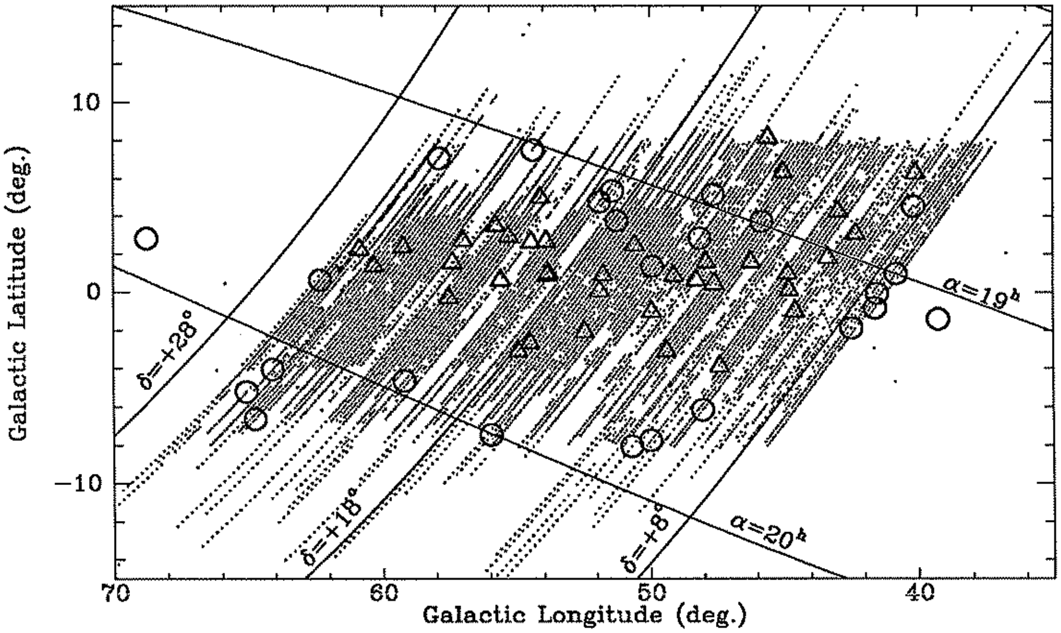

Figure 4.4: Sky coverage of both phases of the Princeton-Arecibo II survey. Dots are successfully processed beam areas; circles are newly discovered pulsars; triangles are previously discovered pulsars detected in the survey.

A total of twenty pulsars were detected in the survey. Nine of these had been discovered previously; their parameters are given in table 4.3. A list of pulsars near our pointing positions but not detected in this survey is given in table 4.2.

Eleven new pulsars were detected. Of these, ten were slow, apparently isolated objects. Parameters of these pulsars are given in table 4.4, and their profiles are shown in figure 4.6. One new millisecond pulsar was detected: PSR J2019+2425 has a period of 3.935 ms. Like many recycled pulsars, it is in a binary orbit. This object is discussed in detail in chapter 6.

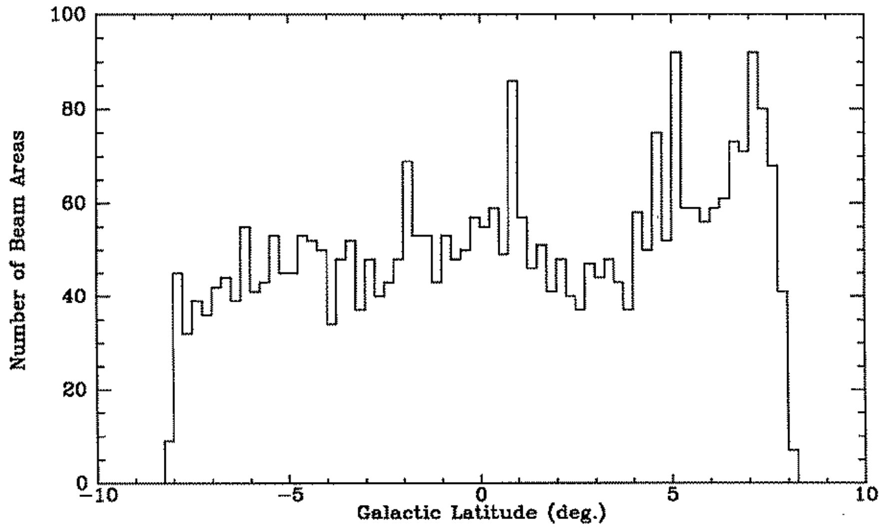

Figure 4.5: Number of beam areas observed as a function of Galactic latitude for the second phase of the Galactic plane search. The slight bias towards positive Galactic latitude was an effect of telescope scheduling.

Table 4.1: Period ranges (in milliseconds) automatically excluded from consideration due to multiple occurrences of interference signals.

1.0332–1.0334	3.0997–3.0998	7.7830–7.7940
1.0900–1.0950	3.1133–3.1135	8.1774–8.1776
1.1600–1.1680	3.2700–3.2850	8.3500–8.3900
1.3628–1.3630	3.3200–3.3500	10.9033–10.9034
1.5500–1.5600	3.8850–3.8950	11.0213–11.0214
1.9458–1.9460	4.0880–4.0890	13.2255–13.2257
2.0665–2.0667	4.4058–4.4063	22.0426–22.0427
2.1800–2.1900	5.1888–5.1889	33.0630–33.0640
2.3300–2.3400	5.4250–5.4300	66.1200–66.1300
2.5940–2.5950	5.4510–5.4550	132.2400–132.2600
2.7129–2.7130	5.5000–5.6100	
2.7257–2.7258	5.9620–5.9630	

Table 4.2: Previously known pulsars within 10′ of a telescope pointing position in the Galactic plane survey but not detected. The half-power half-beam width of the telescope is about 5′, so most of these non-detections are expected. However, we have included this larger list since known pulsars were occasionally detected farther than 5′ from the center of the beam (see table 4.3.) Note that some catalog positions only have 5′ accuracy, so beam-center distances may be significantly off.

Name (1950.0)	Dist from Beam Ctr	Zenith Angle	Period (ms)	DM	Flux (mJy)	Notes
B1848+12	9.9′	18.0°	1205.299	71	4	
B1901+10	6.5	9.9	1856.568	140	2	
B1901+10	6.5	10.0	1856.568	140	2	
B1901+10	7.1	10.0	1856.568	140	2	
B1903+07	8.3	11.2	648.039	260		
B1906+09	4.0	9.1	830.270	250	5	
B1906+09	9.4	9.0	830.270	250	5	
B1911+09	4.0	9.0	1241.964	155	3	
B1911+09	6.7	9.1	1241.964	155	3	
B1911+09	7.4	8.9	1241.964	155	3	
B1911+11	9.7	8.3	600.997	80	5	
B1911+13	8.1	5.5	521.472	144		
B1911+13	9.0	5.2	521.472	144		A
B1914+09	9.0	8.5	270.253	61	15	B
B1919+15	7.3	5.1	618.180	95		C
B1920+20	7.2	6.1	1172.761	203	6	D
B1925+18	8.9	4.0	482.765	250	3	D
B1926+18	8.8	4.3	1220.469	109	3	D
B1929+20	9.4	2.3	268.215	210	50	D
B1943+18	7.6	13.3	1068.707	215	4	E
B1944+26	9.1	10.8	435.000	182	2	
B2000+16	8.8	17.6	276.440	80	1	

Notes: A. Marginal detection of 3rd Harmonic, SNR = 6.0. B. Marginal detection, SNR = 5.8. C. Mild 5.5ms interference; shouldn't affect this pulsar. D. Detected at a different pointing position (see table 4.3). E. Possible detection of 4th harmonic, SNR = 5.9.

Table 4.3: Previously known pulsars within 10′ of the telescope pointing position in the Galactic plane survey which were detected in the survey. The variable n_h refers to the number of harmonics used in the detection. Each scan in which a pulsar was detected is listed.

Name (1950.0)	Beam Dist	Zen. Angle	Period (ms)	Search DM	Cat. DM	Flux (mJy)	SNR	n_h
B1839+09	3.7′	16.9°	381.32	46	49	18	38.7	16
B1848+13	5.8	14.6	345.56	55	59	4	18.3	16
B1855+09	5.5	10.7	5.36	13	13	15	9.3	4
B1913+10	2.9	8.3	404.49	126	240	20	11.9	16
B1915+13	8.0	4.5	194.61	93	94	30	44.5	16
B1915+13	9.2	4.5	64.86	76	94	30	86.9	2
B1915+13	9.2	4.7	194.61	95	94	30	20.9	16
B1920+20	4.4	6.2	1171.92	128	203	6	10.8	16
B1925+18	5.5	3.8	482.81	300	250	3	8.9	16
B1929+20	0.6	2.1	67.04	190	210	50	27.3	3
B1929+20	9.0	2.0	286.22	225	210	50	8.8	16
B1935+25	8.8	8.3	200.97	15	62	13	49.3	16
B1935+25	1.4	8.2	200.99	36	62	13	43.8	16

Table 4.4: New pulsars discovered in the plane survey. Except for J2019+2425, positions and DM's are those from the search data. Positions have 5′ uncertainty; DM accuracy varies as a function of period, but is of order 20. Except for PSR J2019+2425 (discussed in detail in chapter 6), the flux values are estimated from the initial discovery scan, and may differ significantly from the mean flux due to interstellar scintillation.

Pulsar (J2000.0)	α (1950.0)	δ (1950.0)	P (ms)	DM ($cm^{-3}pc$)	Flux (mJy)
J1848+08	$18^h46^m03^s$	$+08°25'55''$	328.66	95	2.8
J1859+15	18 57 32	15 19 18	933.97	90	3.0
J1902+07	18 59 07	07 22 11	487.81	90	2.4
J1906+18	19 04 34	18 45 57	1019.09	115	1.9
J1908+07	19 05 39	07 30 53	212.35	10	6.5
J1909+07	19 07 53	07 12 47	2711.99	115	4.9
J1915+07	19 13 15	07 30 30	1542.70	50	3.6
J1941+10	19 39 16	10 20 12	905.39	130	4.4
J1951+11	19 48 45	11 13 44	5094.08	90	12.8
J2015+25	20 13 01	25 18 38	2303.96	40	2.2
J2019+2425	20 17 23	24 15 46	3.93	17	9.5

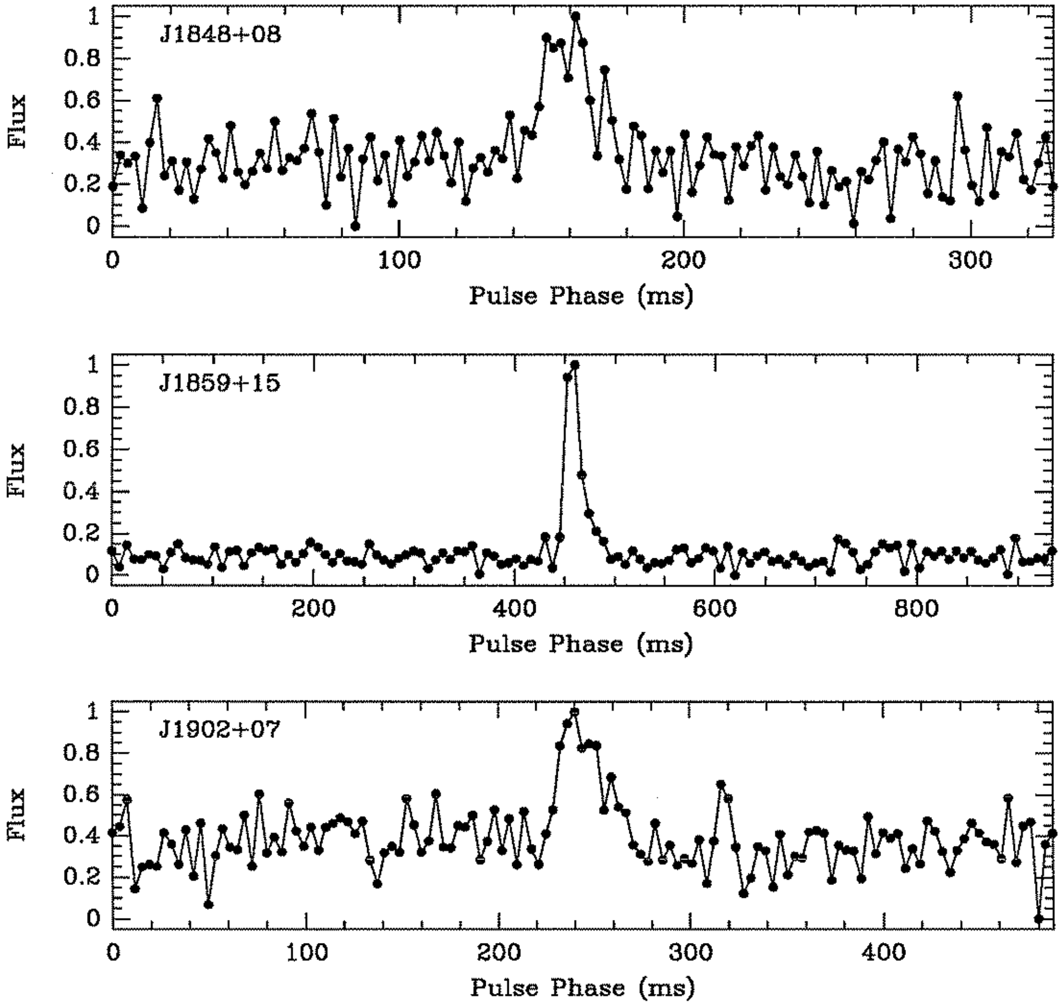

Figure 4.6: Profiles of new pulsars discovered in the Galactic plane survey. Approximately two minutes of data were folded to produce these profiles. Data were collected with 516 μs resolution; adjacent samples were summed to produce 128-bin profiles for these plots. Part one of four.

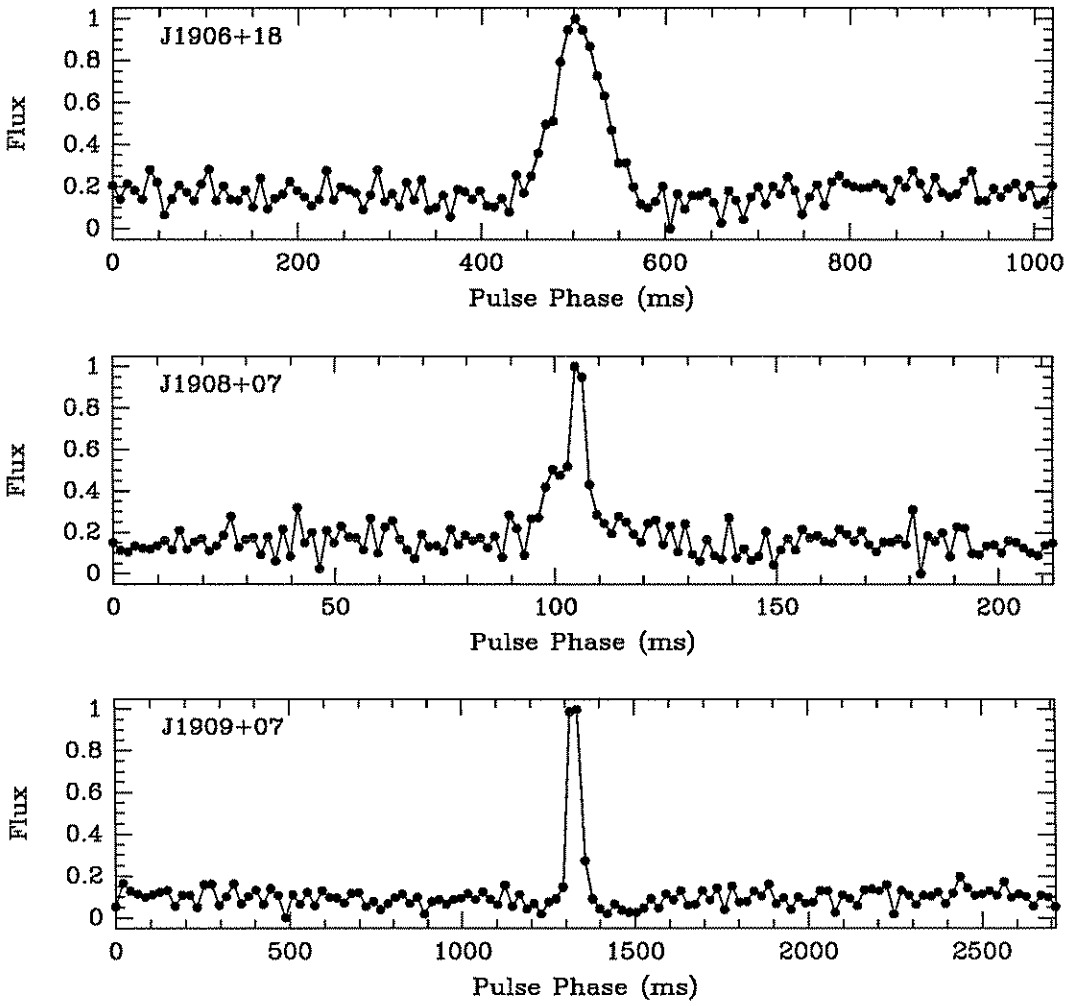

Figure 4.6: Part two of four.

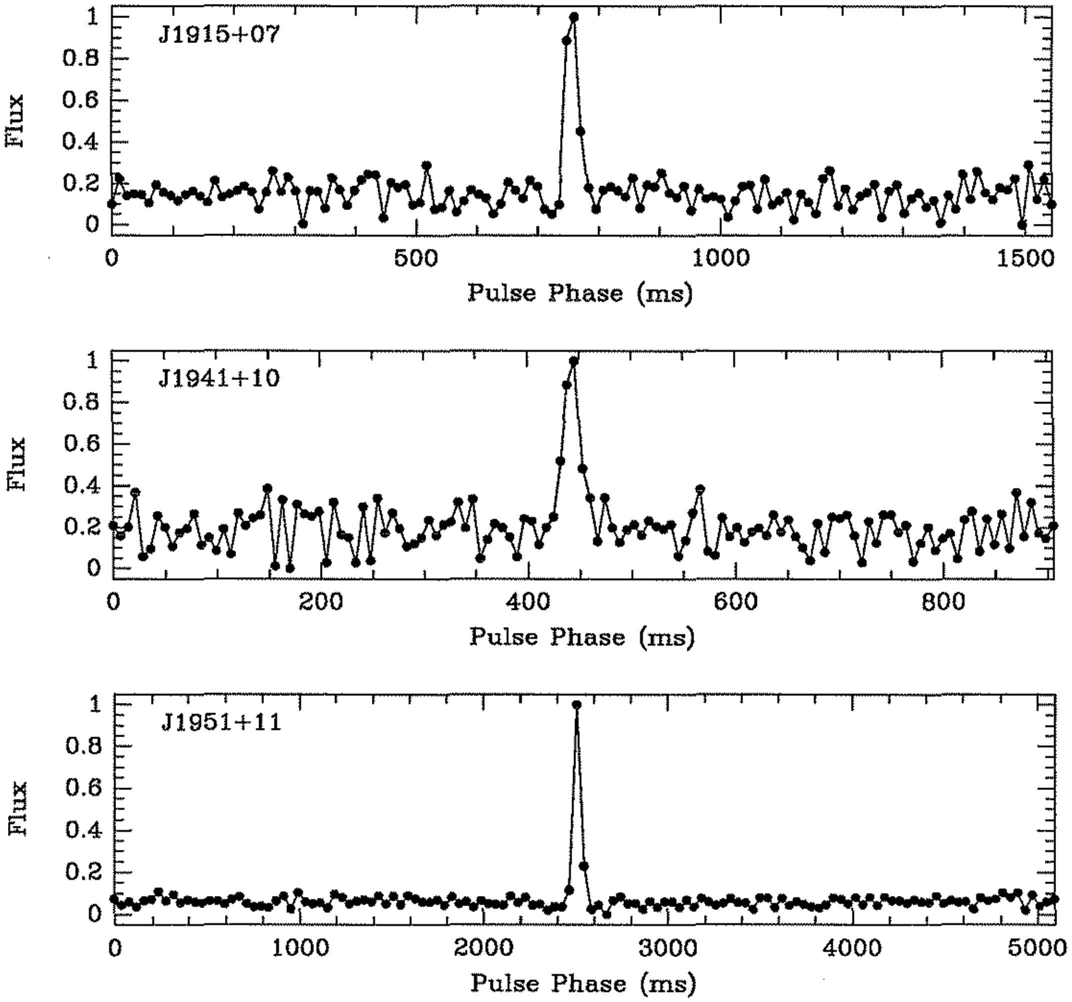

Figure 4.6: Part three of four.

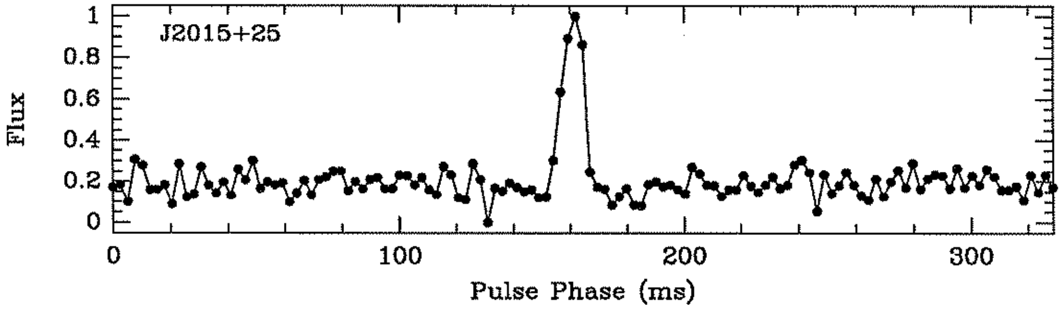

Figure 4.6: Part four of four.

4.4 PSR J1951+11

One of the new pulsars, PSR J1951+11, with a period of 5.094 s, has the slowest rotation rate of any known radio pulsar. The detection of a pulsar with a period this slow was particularly surprising because the search software filters out signals with periods greater than 1 s and has a firm upper limit of 2.5 s in its period search range. The pulsar was initially detected as a 1.698 s periodicity—one third its actual period, meaning that the 3rd, 6th, 9th, and so on up to $3 \times 16 = 48$th harmonics were being detected. Follow-up observations detected periods alternating between one third and one fourth the 5.094 s period, and the fundamental period was soon deduced.

The pulsar could be detected using such high harmonics only because of its extremely short duty cycle: the pulse width is approximately 20 ms, so the duty cycle is only 0.4% or 1.4°. Individual pulses are substantially shorter than this, typically 10 ms, and a large fraction of pulses are not visible at all. An average profile is given in figure 4.6. Figure 4.7 shows close-up views of the pulsar peaks in each of twenty-six consecutive periods. No pattern is apparent in the subpulse behavior, but further analysis is called for.

The extremely short duty cycle of PSR J1951+11 is unprecedented. Surprisingly, however, it is in some sense predicted. Rankin (1990) suggested an empirical relation between pulse width $W_{\rm core}$, period P, and the angle α between the pulsar's rotation and magnetic axes:

$$W_{\rm core} = 2\overset{\circ}{.}45 P^{-1/2} / \sin\alpha. \tag{4.8}$$

This predicts a core-component width of 1.1° if the pulsar is an orthogonal rotator (i.e., if $\alpha = 90°$), and a larger width otherwise. Such core-dominated pulsars are in general very young, which suggests that J1951+11 has a relatively large period derivative (which is also necessary for it to have a large enough magnetic field to emit radio waves.)

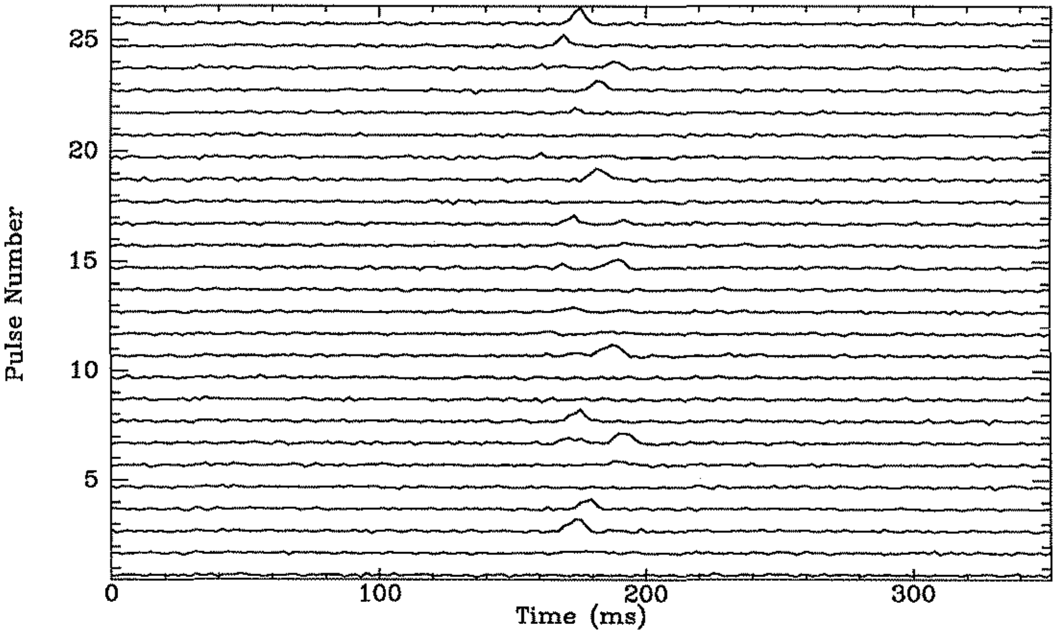

Figure 4.7: Close-up view of 350 ms (approximately 7% of the pulse period) around peaks of twenty-six consecutive pulses of PSR J1951+11. The pulsar frequently nulls for one to two periods. When visible, the emission pattern consists of one or occasionally two 10 ms subpulses. When data from a sufficiently large number of periods is summed the resulting profile has a single component of width 20 ms.

Chapter 5

The High Latitude Survey

A search program oriented away from the Galactic plane was undertaken at the Arecibo Observatory in August and September 1991, with follow-up observations in subsequent months. The particular region of the sky surveyed, between Galactic latitudes $b = -50°$ and $b = -30°$, was assigned somewhat arbitrarily by the observatory scheduling committee.

5.1 Rationale

A list of the recycled pulsars detected in the Galactic plane search is given in table 5.1. The distribution of detected pulsars is clearly skewed toward those pulsars close to the earth: two of the four pulsars detected in the plane search are less than 1 kpc away.

If the scale height of recycled pulsars were of order 1 kpc, we would expect the distribution of these pulsars to be nearly uniform on the sky. Even if the scale height were only a few hundred kpc, a substantial fraction of detectable pulsars would be found away from the Galactic plane.

The scale height of these objects was not known as we began this survey. However, the scale height of slow pulsars is 230 pc (Manchester & Taylor 1977), and recycled pulsars are much older (and thus have more time to propagate away from the Galactic plane), so we might expect them to have a somewhat

Table 5.1: Recycled pulsars detected in recent surveys.

Pulsar	l (deg.)	b (deg.)	DM ($\mathrm{cm^{-}3pc}$)	Dist.[a] (kpc)
Galactic plane survey (chapter 4)				
B1855+09	42.3	3.1	13	0.72
B1937+21	57.5	-0.3	71	3.94
B1957+20	40.9	-15.1	29	1.66
J2019+24	65.2	-6.9	17	0.95
Wolszczan (1991) high latitude survey				
B1257+12	311.3	75.4	10	0.58
B1534+12	19.8	48.3	12	0.69

[a] Calculated using model of Cordes & Taylor (1992)

larger scale height.

Thus it appeared that searching for pulsars at high Galactic latitudes would be a productive activity. Further (overwhelming) evidence that pulsars could be detected at high latitudes was provided by a survey of Wolszczan (1991), which found two recycled pulsars out of 150 square degrees surveyed using a system similar to that described in chapter 4 (see table 5.1).

5.2 Hardware and Sensitivity

The expected characteristics of high-latitude pulsars led us to use data acquisition equipment for this survey which differed from that of the earlier plane survey. The local density of interstellar free electrons is around 0.02 cm^{-3} (Cordes *et al.* 1992; Cordes & Taylor 1992), so for pulsars a kiloparsec from the earth, we expect dispersion measures of order 20 $\mathrm{cm}^{-3}\mathrm{pc}$, significantly less than expected for the distant Galactic plane sources to which we were sensitive in our earlier survey. Since the expected dispersion smearing was less than that of our earlier survey, we were able to use wider frequency channels without fear of unduly smearing the pulsar signals.

A filterbank with thirty-two 250 kHz channels in each of two polarizations is available at Arecibo and was used for this project. The channel bandwidths were approximately three times those used in the Galactic plane survey, but this was relatively unimportant. The total bandwidth was 8 MHz rather than the 10 MHz processed by the autocorrelator-based survey, but the response of the telescope feed falls off rapidly at the edge of the passband, so this was a minor loss. We centered the passband at sky frequency 429 MHz, close to the center frequency of the feed.

The switch to the filterbank-based system had a major advantage. Using the observatory's "Radar Interface", a digitizing data acquisition system, the filterbank data could be sampled much more frequently than the 516.625 μs rate to which we were restricted by the autocorrelator-based system. As an added benefit, the detected data were already in the time and frequency matrix form desired for analysis.

The filterbank detected the signals from each of the 2×32 channels and filtered the result through a low-pass RC circuit with a 333 μs time constant. The detected signals from the same frequency but opposite polarizations were summed, and the resulting voltages sampled every 250 μs. The digitization circuit had 12-bit resolution; to save storage space, only 3 bits were retained. The 3-bit resolution was not used to its fullest potential for two reasons: first, signal levels were adjusted manually by observing output levels on an oscilloscope and tuning an attenuator, a procedure which cannot precisely optimize the levels; second, the fluctuation levels of the filterbank channel outputs could not be individually adjusted, so to keep all channels in the valid digitization range some channels necessarily covered less than the full range. Still, all channels normally crossed several digital levels, so there was little loss of sensitivity due to quantization.

During data collection, a clock signal with period 250 μs would trigger a sampling cycle in which pairs of channels were sampled in turn at 1 μs intervals. Since the interval between measurements of different channels was much less than the sample period, we treated the data as though the channels were sampled simultaneously.

The system temperature was of order 60 K for these observations—the sky temperature at high latitudes does not vary significantly, as it did in the Galactic plane search, and all observations were made at low zenith angles ($z < 4.2°$). The bandwidth was $B = 8$ MHz and the integration time $t = 32.768$ s. Average telescope gain across the passband was 16.4 K/Jy (at zero zenith angle). These numbers in equation 2.31 give SNR = 2.21 mJy$^{-1}S_j$ for a single sine wave source of amplitude S_j. Thus, a 3.6 mJy source would be over the threshold limit of SNR ~ 8 with one harmonic, while a source with sixteen equal amplitude harmonics and a total flux of 0.9 mJy would have been detected.

The passband shape of individual filters in this filterbank is given in Rawley (1986) as

$$a(\nu) = \frac{1}{w\sqrt{\pi}} \exp(-(\nu - \nu_0)^2/w^2), \tag{5.1}$$

where $w = 125$ kHz is the half-width of the filters and we have assumed normalization $\int_0^\infty df\, a(\nu) = 1$. The passband has Fourier transform

$$\mathcal{A}(t) = \exp(-(\pi w t)^2). \tag{5.2}$$

An RC low-pass filter with time constant τ—such as used here to filter the detected channel outputs—has transmission function

$$V_{out} = \frac{1}{2\pi i f \tau + 1} V_{in}, \tag{5.3}$$

so the amplitude transmission is

$$\mathcal{R}(f) = \left|\frac{1}{2\pi i f \tau + 1}\right| = \left(\frac{1}{1 - (2\pi f \tau)^2}\right)^{1/2}. \tag{5.4}$$

These transmission functions, combined with equations 2.31 and 2.32 can be used to calculate the relative sensitivity to pulsars of different periods and dispersion measures. Results of this calculation are given in figure 5.1. A comparison of the sensitivity of this survey with that of the plane survey is given in figure 5.2. The faster sampling time for this survey made it more

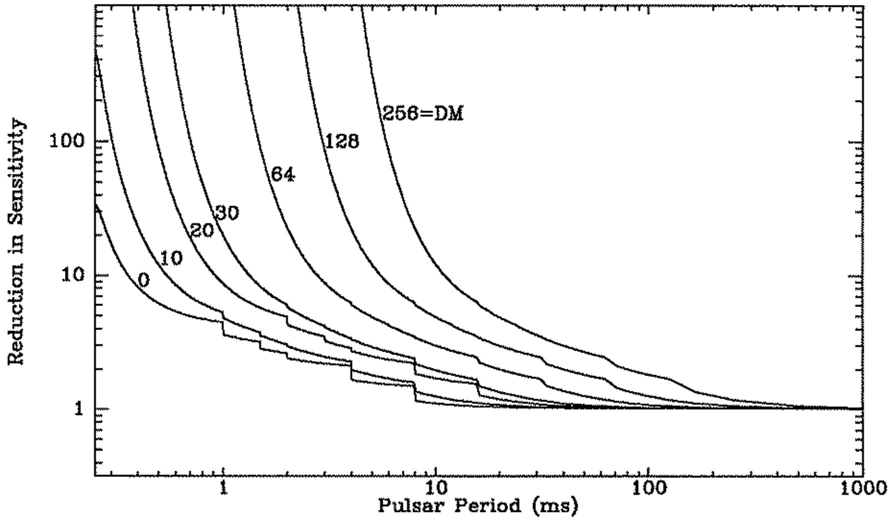

Figure 5.1: Relative sensitivity as a function of pulsar period. Curves are given for several values of DM. Figure 4.2 gives comparable information for the Galactic plane survey. All known pulsars at high latitudes have DM < 40.

sensitive at the lowest dispersion measures, but as dispersion smearing became significant at higher DM's the plane search became relatively more sensitive. The high latitude survey had the added benefit of lower zenith angles and lower sky temperatures, but was hampered by a factor of two reduction in integration time.

5.3 Sky Coverage

The particular patch of sky covered in this survey was somewhat arbitrarily assigned by the Arecibo Observatory administration. Since we expected that pulsars could be found anywhere in the sky the precise location was unimportant. To minimize zenith angles, the observations were made between +14° and +22° declination, centered around Arecibo's latitude of 18°21′. The right ascension range was $21^h30^m < \alpha < 01^h00^m$. A total of 170 square degrees of clean data were processed; a map of the beam areas successfully observed and

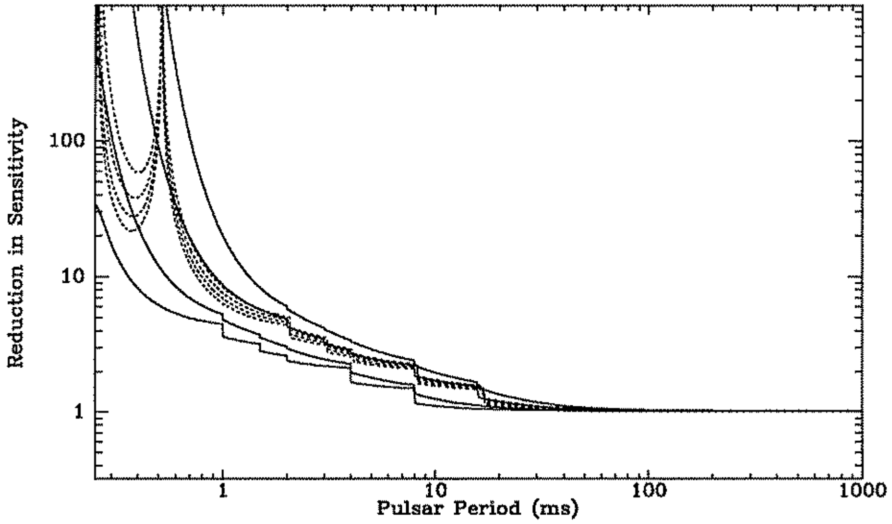

Figure 5.2: A comparison of the sensitivity of data acquisition equipment used in the two surveys. Note that differences due to zenith angle, sky temperature, total bandwidth, and integration time are not included here. For each survey curves are given for DM of 0, 10, 20, and 30, from bottom to top. Broken lines correspond to the Galactic plane survey; solid lines to the high latitude survey. Because the sensitivity of the Galactic plane survey was dominated by its limited sampling rate and not dispersion smearing at these low DM's, its curves have little variation. It is evident that the high-latitude survey was more sensitive for DM < 20, and less sensitive for DM > 20.

processed is presented in figure 5.3.

The survey was conducted using drift scans, in which the telescope acted as a transit instrument. This allowed us to minimize the zenith angle at a given declination. The beamwidth of the telescope is approximately 9′, so a source drifts through the beam in 38 s at the central declination +18°21′, with slight variations in time depending on the precise declination under observation. Each session observed a different strip of constant declination (in 1991 coordinates). Scans of continuously sampled data were collected for 4000 s each, producing the maximum amount of data we could store on a single 9-

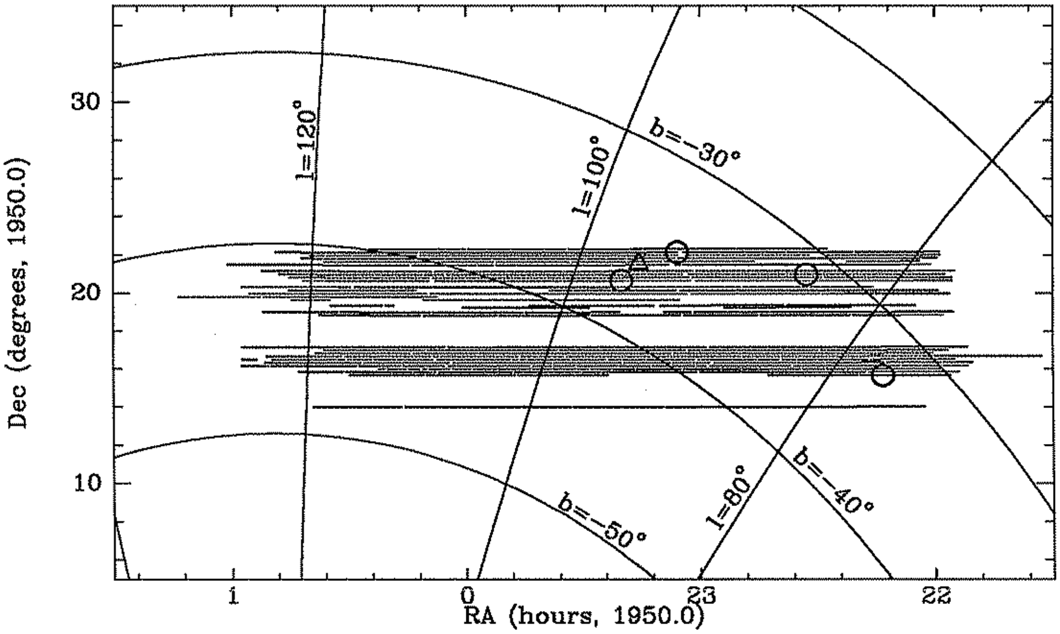

Figure 5.3: Successfully processed beam areas in the high latitude survey. Circles are new pulsars. The triangle is the previously discovered pulsar detected in the survey. Note that this plot has half the linear scale of the similar plots in chapter 4, and that it is in equatorial rather than Galactic coordinates.

track magnetic tape. Dead time between scans was of order 20 s. Scans were all begun on 10 s clock signals from the observatory's standard clock to allow the data to be used for timing of newly discovered pulsars.

The data were analyzed in 32.768 s blocks, a computationally convenient number (equal to 2^{17} sample periods) which closely matches the time a source takes to traverse the beam. Each drift scan was analyzed in two passes, with offset blocks of data analyzed in the different passes. Initially, the data were processed in consecutive 32.768 s blocks in each pass, with the start points of blocks for the two passes offset by 16.384 s. To save computer time without significant loss of efficiency, we later switched to a "skip-stop" method in which the drift scans were analyzed by processing a 32.768 s block, skipping 16.384 s,

Table 5.2: Period ranges disallowed due to frequent detection of interference signals.

Period(ms)	DM	Period(ms)	DM
1.858–1.868	0–300	3.345–3.346	0–19
1.239–1.245	0–18	4.291–4.299	0–19
0.7442–0.7448	0–18	5.550–5.555	0–19
7.590–7.598	0–76	7.580–7.590	0–19
2.152–2.168	59–83	16.800–17.100	0–38
4.995–5.005	76–300	19.360–19.410	0–38
0.743–0.746	0–19	33.600–34.200	0–76
1.855–1.858	0–19		

and repeating, then doing a second pass offset by 24.576 s.

5.4 Results

The search software followed the procedure outlined in chapter 2. A number of regularly occurring interference signals were automatically excised; these portions of period-dispersion measure space are listed in table 5.2.

There was only one previously known pulsar in the area under observation. PSR B2315+21 has a period of 1.444 s, a DM of 20.5 $\mathrm{cm}^{-3}\mathrm{pc}$, and a flux of 12 mJy; it was readily detected in our survey. Three new slow pulsars and one millisecond pulsar were also discovered. Their characteristics are listed in table 5.3 and profiles of the slow pulsars are displayed in figure 5.4. The millisecond pulsar PSR J2322+2057 is discussed in detail in chapter 7.

While drawing conclusions from the positions of only four objects is problematic, it appears significant that all four slow pulsars detected in this survey have Galactic latitudes smaller than the single millisecond pulsar detected.

Table 5.3: New pulsars discovered in the high latitude survey. Parameters are from the initial discovery data (except the flux density of J2322+2057).

Pulsar (2000.0)	α (1950.0)	δ (1950.0)	P (ms)	DM $\mathrm{cm}^{-3}\mathrm{pc}$	S_{430} (mJy)
J2215+15	$22^h13^m10^s$	$+15°38'56''$	374.160	19	1.8
J2235+21	22 32 36	+20 58 27	1357.380	16	1.4
J2308+22	23 05 39	+22 07 52	535.940	15	3.4
J2322+2057	23 19 53	+20 40 34	4.808	13	0.5

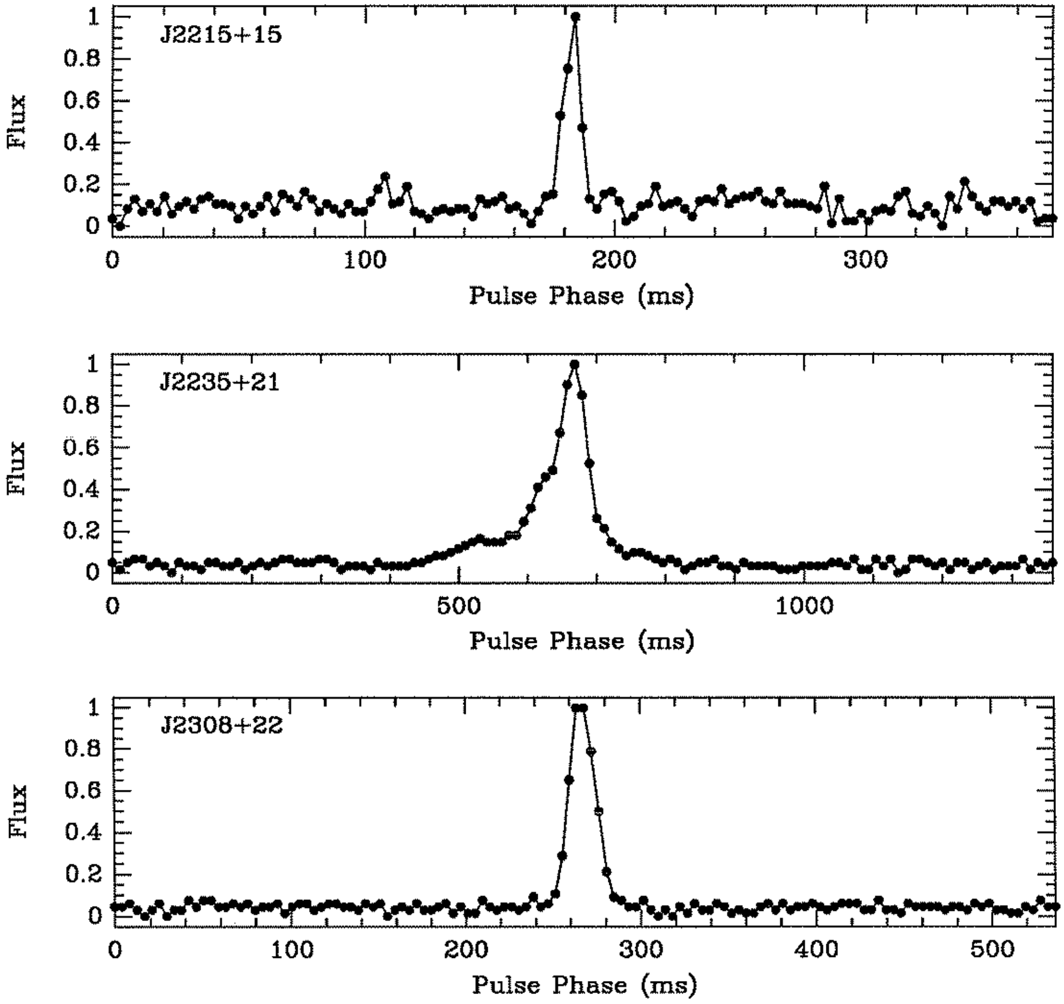

Figure 5.4: Profiles of newly discovered slow pulsars. Each profile was generated by folding 230 s of data taken with the search equipment.

Chapter 6

PSR J2019+2425

The millisecond pulsar PSR J2019+2425 was initially detected in Galactic plane search data collected on 10 February 1991. It was confirmed by a search-mode observation on 6 August 1991. On 8 August 1991 an intensive campaign of timing observations was begun. Conveniently, the high-latitude search was underway at this time, and the pulsar was visible at the start of many of the search sessions. For approximately one and a half months (through 24 September 1991), it was possible to make brief (and sometimes extensive) observations of the new pulsar. Further observations have been made at intervals of several weeks since then.

Within two days of confirmation, it was clear that this pulsar is in a binary system: the observed period slowly changes in a manner consistent with Doppler shifts induced by orbital motion. Subsequent observations have shown the pulsar to be in a long-period, nearly circular orbit with a $\sim 0.3\ M_\odot$ companion. The observed pulsar period is plotted as a function of time in figure 6.1.

6.1 Timing Observations

The timing observations used the Princeton Mark III data acquisition system, which was specifically designed for high-resolution timing of millisecond

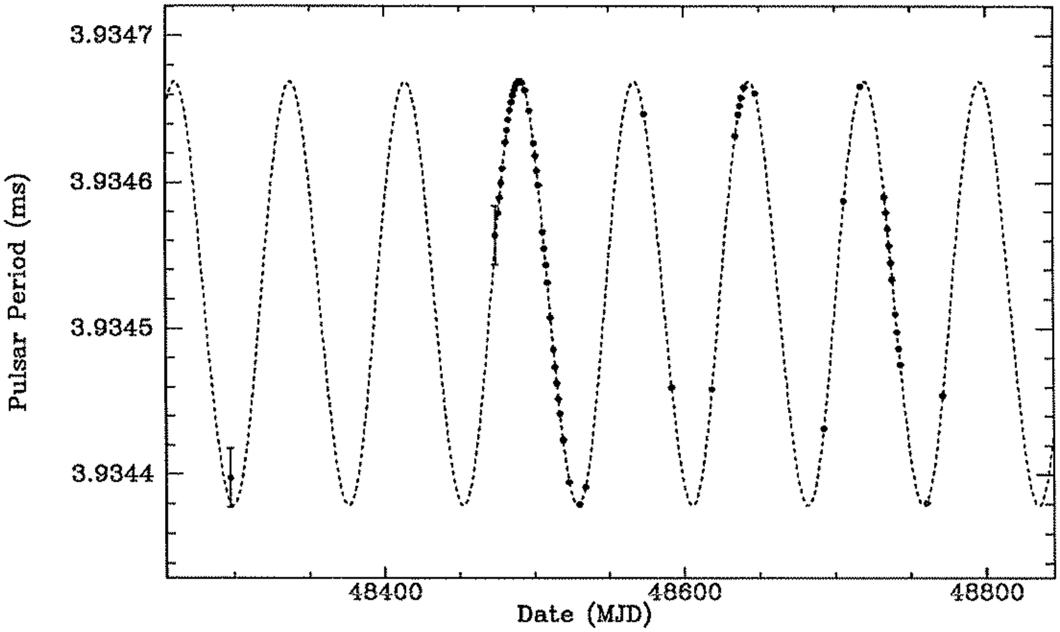

Figure 6.1: The observed pulsar period, reduced to the solar system barycenter, is shown as a function of time. The period varies due to Doppler shifts as the pulsar traverses its orbit. The broken line was calculated using the a model fit to the timing data (see below). The two points with large uncertainties were calculated using single 67 second observations during search and confirmation runs. All other points (which have error measures smaller than the displayed points) are averages of daily observations ranging from 10 to 160 minutes in duration.

pulsars (Stinebring *et al.* 1992). The bulk of the timing measurements were made at 430 MHz. Two separate data collection subsystems were operated in parallel. An 8 MHz passband was divided into thirty-two 250 kHz channels in each of two orthogonal polarizations. The resulting 2 × 32 narrow channels were square-law detected, and the voltages from orthogonal polarizations at the same frequency were summed. The summed signals were digitized and the resulting series folded at an approximate topocentric pulse period. Thus, a total of 32 pulse profiles, each at a separate frequency, were collected simultaneously. Dispersion smearing across the 0.250 MHz channels limited resolution to 450 μs in this data. At the same time, a separate circuit was used to coherently de-disperse two 0.625 MHz passbands in each polarization, providing data with lower signal strength (due to the smaller bandwidth) but higher time resolution. Details of the coherent dispersion removal hardware can be found in Hankins and Rajkowski (1987) and Ryba (1991). These signals were also detected, digitized, and folded at the pulsar period. Software in the data acquisition system varied the center frequencies of the two narrow, high-resolution passbands to seek scintillation maxima in the incoming data. Data in both subsystems were integrated for intervals of one to three minutes.

A small amount of data was collected between 1300 MHz and 1420 MHz. In this frequency range, a $2 \times 32 \times 1.25$ MHz filterbank was used in the manner of the $2 \times 32 \times 250$ kHz filterbank at 430 MHz. Dispersion smearing across a single channel limited resolution to 68 μs for this data.

6.2 Profile and flux

Integrated pulse profiles collected at the two observing frequencies are displayed in figure 6.2. The pulse shape consists of four distinct components, labeled A through D in the figure. The profiles at 430 MHz and 1400 MHz are similar in spacing and relative heights of the components with the exception that component B is much stronger at the higher frequency. To quantify the component strength variation, a model of four Gaussian-shaped components (plus an overall DC offset) was fit to the profiles. This model fit the 1400 MHz data well, but left a small systematic residual in the 430 MHz profile. Despite this minor residual, the fit component locations in the two profiles lined up within reasonable tolerance, suggesting the model is adequate for crudely quantifying the profile component behavior. The relative locations and strengths of the components are listed in table 6.1.

The mean flux density of the pulsar is difficult to measure at either observing frequency due to the very significant effects of interstellar scintillation.

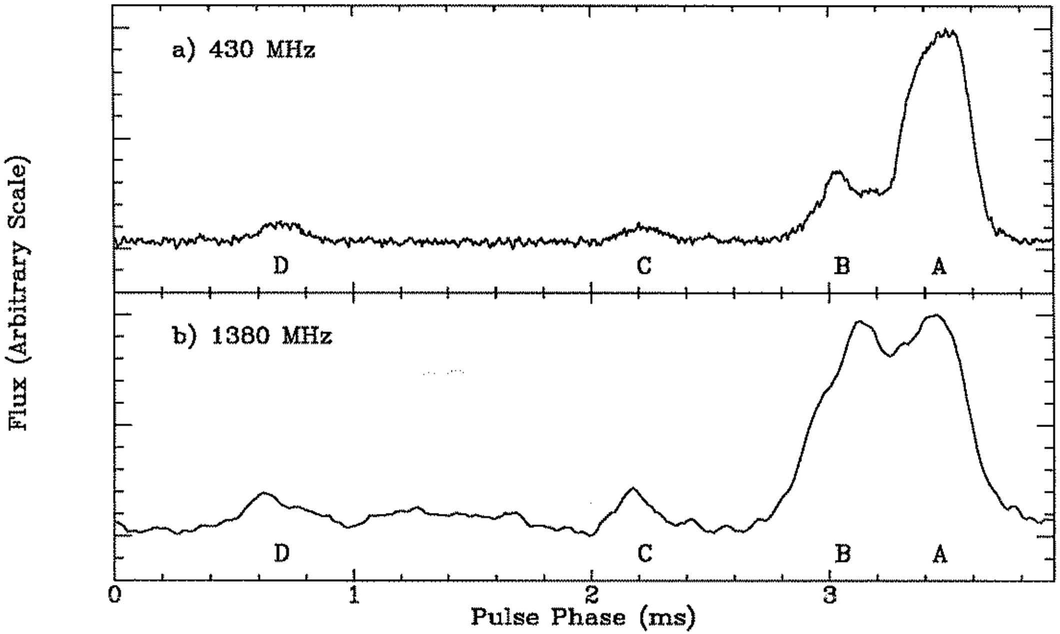

Figure 6.2: Integrated pulse profiles at 430 MHz and 1380 MHz. The 430 MHz profile was generated using pre-detection dedispersion circuitry, and so smearing is minimal. Data from independent observations made over several days were coherently summed to produce this profile. The 1380 MHz profile was compiled from filterbank data from a single observing session. Resolution of the 1380 MHz data, limited by dispersion smearing, is 68 μs. Relative strengths of the profile components are given in table 6.1.

The flux at 430 MHz can vary by a factor of two on a timescale of a few minutes. By averaging over many observations, we estimate the flux to be $S_{430} = 2.7 \pm 0.3$ mJy. The situation at 1300–1420 MHz is less clear due to the small number of observations (and the fact that we varied the observing frequency during these observations to peak up on scintillation maxima). Flux densities in this band were measured between 0.15 and 0.43 mJy; the true flux is likely between 0.2 and 0.3 mJy, but more extensive, systematic observations would be needed to make an accurate measurement.

Table 6.1: Profile component parameters. Components are defined in figure 6.2. Component positions are measured relative to the fit position of component A. The apparent changes in component position between the two frequencies are probably not due to intrinsic profile evolution but rather to systematic errors caused by our naive four-Gaussian-component model of the pulse profile.

Component	Position		Relative Strength	
	430 MHz	1380 MHz	430 MHz	1380 MHz
A	000.0°	000.0°	0.729	0.37
B	323.0(3)°	328.6(5)°	0.190	0.55
C	246.9(9)°	242.0(6)°	0.035	0.03
D	107.3(6)°	102.9(9)°	0.045	0.04

6.3 Timing Results

Pulse times-of-arrival were calculated for individual one to three minute data scans by (1) rotating the pulse profile acquired in each frequency channel to counteract the effects of interstellar dispersion; (2) adding these de-dispersed profiles to produce a single profile for a given integration; (3) fitting this profile to a high-resolution "standard profile" built up from many integrations; and (4) adding the offset obtained from the fit to the scan start time, which can be traced back to atomic time standards such as that of the National Institute of Standards and Technology.

The resulting series of times-of-arrival was fit to a model of pulse behavior using standard techniques, including the Tempo software package (Taylor & Weisberg 1989). Free parameters in the model include dispersion measure; pulse phase, period, and period derivative; pulsar sky position; and the five Keplarian orbital parameters: projected semi-major axis, orbital period, eccentricity, angle of periastron, and time of periastron passage. The best-fit parameters are listed in table 6.2. Residual pulse arrival times after subtract-

Table 6.2: Parameters of the PSR J2019+2425 system.[a]

Right ascension (J2000)[b]	$20^h19^m31^s.95213(9)$
Declination (J2000)[b]	$+24^\circ25'15''.376(4)$
Right ascension (B1950)[c]	$20^h17^m23^s.0631(1)$
Declination (B1950)[c]	$+24^\circ15'46''.162(3)$
Period (ms)	3.934524079417(8)
Period derivative (10^{-21})	7.0(5)
Epoch (MJD)	48505.0000
Dispersion measure ($\mathrm{cm}^{-3}\mathrm{pc}$)	17.2028(1)
Projected semi-major axis (lt-s)	38.7623(1)
Orbital period (s)	6610605.4(2)
Time of ascending node (MJD)	48524.412(5)
Eccentricity	0.00011103(4)
Angle of periastron	159.04(2)°

[a] Figures in parentheses are uncertainties in the last digit quoted.
[b] J2000.0 coordinate system based on DE200 ephemeris (Standish 1982).
[c] B1950.0 coordinate system based on PEP740R ephemeris.

ing the best-fit model are displayed in figure 6.3. No trends are apparent in these plots, confirming the validity of the orbital model.

The period derivative of this pulsar, $\dot{P} = 7 \times 10^{-21}$, is unusually small. There is no reason to doubt that the measured period derivative is in fact intrinsic to the pulsar. It is possible for external accelerations to bias the measured $\dot{P}$, but the likelihood of a passing star influencing the pulsar is small. Following the argument of Damour and Taylor (1991), and assuming a pulsar distance of 1 kpc and no proper motion, the measured $\dot{P}$ would be shifted -3×10^{-22} by acceleration of the pulsar along the line of sight due to Galactic differential rotation, so this effect too is negligible.

Assuming pulsar rotation is slowed by magnetic dipole radiation, a pulsar's characteristic evolution timescale (traditionally referred to as its "age") is $\tau = P/2\dot{P}$. This formula gives a timescale of 9×10^9 yr for PSR J2019+2425, the longest timescale observed for any pulsar. The next-longest timescale, at

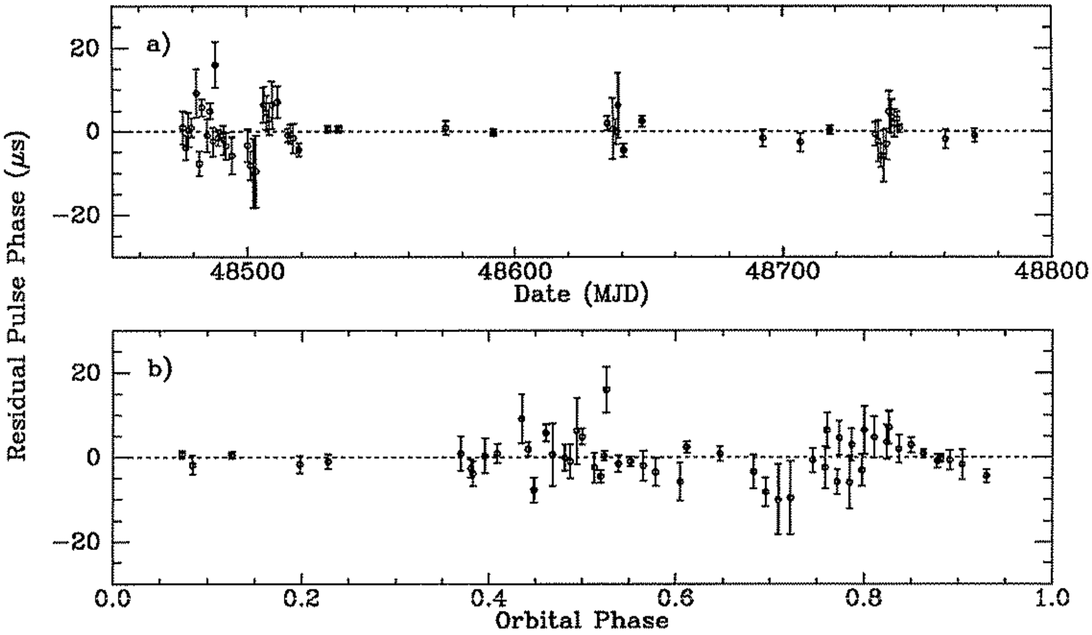

Figure 6.3: Daily average pulse arrival times after subtracting the model using the parameters in table 6.2 as a function of (a) time and (b) orbital phase.

least in formal calculations, is 8.2 Gyr for PSR B1639+36A; however, this pulsar is associated with a globular cluster, and its period derivative (and hence its age) is susceptible to bias from the cluster gravitational acceleration (Kulkarni *et al.* 1991). After B1639+36A, the next oldest two pulsars are B1855+09 and B0655+64, with ages 4.8 Gyr and 4.5 Gyr, respectively; both are in binary systems similar to that of J2019+2425.

The surface magnetic field, estimated by $B_0 = 3.2 \times 10^{19}(P\dot{P})^{0.5}$ (Manchester & Taylor 1977), is 1.7×10^8 gauss, the second smallest in the known pulsar population. The field of B1957+21 is slightly smaller.

The small dispersion measure, DM = 17.2028 $\mathrm{cm}^{-3}\mathrm{pc}$, indicates the pulsar is quite near the earth. A new distance model (Cordes & Taylor 1992) gives its distance as approximately 1 kpc.

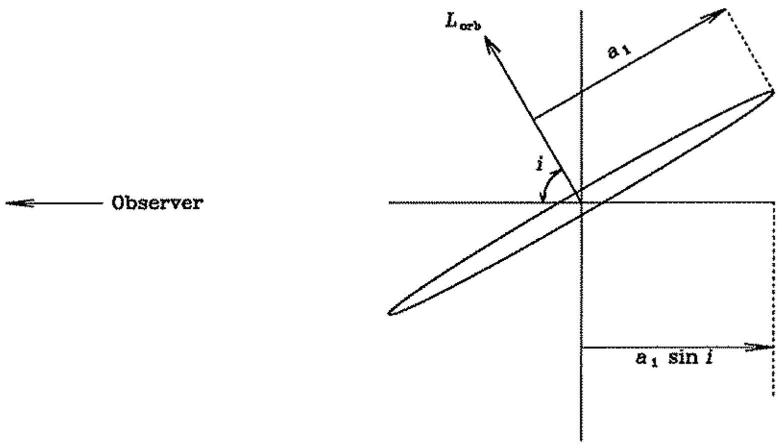

Figure 6.4: Orbital geometry of PSR J2019+2425.

6.4 The Binary System

The geometry of the pulsar orbit is shown in figure 6.4. The orbital radius projected onto the observer's line of sight is known from timing measurements, but the inclination of the orbit, described by the angle i between the orbital angular momentum vector and the line of sight, is not known. We can only analyze quantities which depend on i in a probabilistic sense. Assuming the orbital momentum vector $L_{\rm orb}$ is equally likely to be pointing in any direction, the inclination angle has distribution $p\,(i > i_0) = \cos i_0$.

The observed binary parameters can be used to calculate the mass function of the pulsar:

$$f_1 = \frac{(M_2 \sin i)^3}{(M_1 + M_2)^2} = \frac{4\pi^2}{G} \frac{(a_1 \sin i)^3}{P_b^2}. \tag{6.1}$$

The parameters in table 6.2 give $f_1 = 0.0107\ {\rm M}_\odot$. The companion mass as a function of inclination angle, assuming the canonical pulsar mass of $M_1 = 1.4\ {\rm M}_\odot$, is plotted in figure 6.5. The lower limit on this mass, calculated at $i = 90°$, is $M_2 \geq 0.316 {\rm M}_\odot$. This relatively light mass combined with the small measured eccentricity puts PSR J2019+2425 in a category with similar

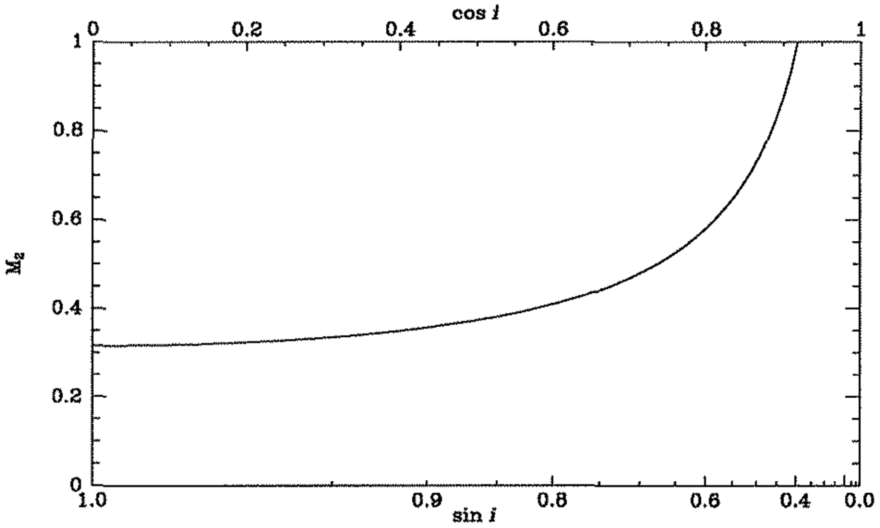

Figure 6.5: Mass of PSR J2019+2425's companion as a function of orbital inclination angle i. The probability distribution of i is $p\,(i > i_0) = \cos i_0$, so the horizontal axis of this figure is scaled such that any point along the it has equal probability of being the true value.

non-cluster recycled pulsars B0655+64, B0820+02, B1831−00, B1855+09, and B1953+29. These objects are believed to have evolved from low-mass X-ray binary systems. The companions, which were giant stars during the spin-up episodes that created the millisecond pulsars, have long since collapsed into white dwarfs (Bhattacharya & van den Heuvel 1991, and references therein).

The white dwarf companions of B0655+64 and B0802+02 have been observed (Kulkarni 1986). Claimed detections of a companion of B1855+09 remain controversial (Wright & Loh 1986; Kulkarni & Hester 1988; Callanan *et al.* 1989). Kulkarni *et al.* (1991) put lower limits on the magnitude of the companion of B1855+09 at 24.6 and 23.4 in the R and I bands, respectively. Since J2019+2425 is likely a bit further away than B1855+09 (using distance estimates based on dispersion measures) and is twice as old, allowing the companion more time to cool, we expect any optical companion of J2019+2425 to be fainter than that of B1855+09. Preliminary optical observations in the direction of J2019+2425 have found no hint of a companion, but a well-calibrated magnitude limit has yet to be set (S. Thorsett and S. Kulkarni, personal communication).

While the wide, low-mass pulsar binaries cannot be used to detect gravitational radiation as tight neutron star-neutron star systems can, the presence of a compact object in these systems does allow for some interesting gravitation experiments. In particular, limits can be placed on violations of the strong equivalence principle. A detailed discussion of this application of PSR J2019+2425 is in chapter 8.

Chapter 7

PSR J2322+2057

The 4.8 ms pulsar PSR J2322+2057 was discovered in the course of the high latitude search described in chapter 5. It was detected in data collected on 17 August 1991, and confirmed on 13 December 1991. Unlike PSR J2019+2425, and unlike most other field millisecond pulsars, it is not in a binary system.

Follow-up timing observations included week-long campaigns in December 1991 and January 1992, and bi-weekly observations since. These observations used the Princeton Mark III pulsar timing system in the same manner as the observations of PSR J2019+2425 described in section 6.1. We report here on data collected through 30 May 1992.

7.1 Profile and Flux

Average pulse profiles at 430 MHz and 1400 MHz are given in figure 7.1. The profiles have a relatively simple structure, with a single interpulse preceding the main pulse by approximately 165°. The interpulse becomes relatively stronger at higher observing frequencies: the ratio of power in the interpulse to power in the main pulse is 0.062 ± 0.002 at 430 MHz and 0.284 ± 0.005 at 1418 MHz.

The basic pulse/interpulse structure is reminiscent of that of the other iso-

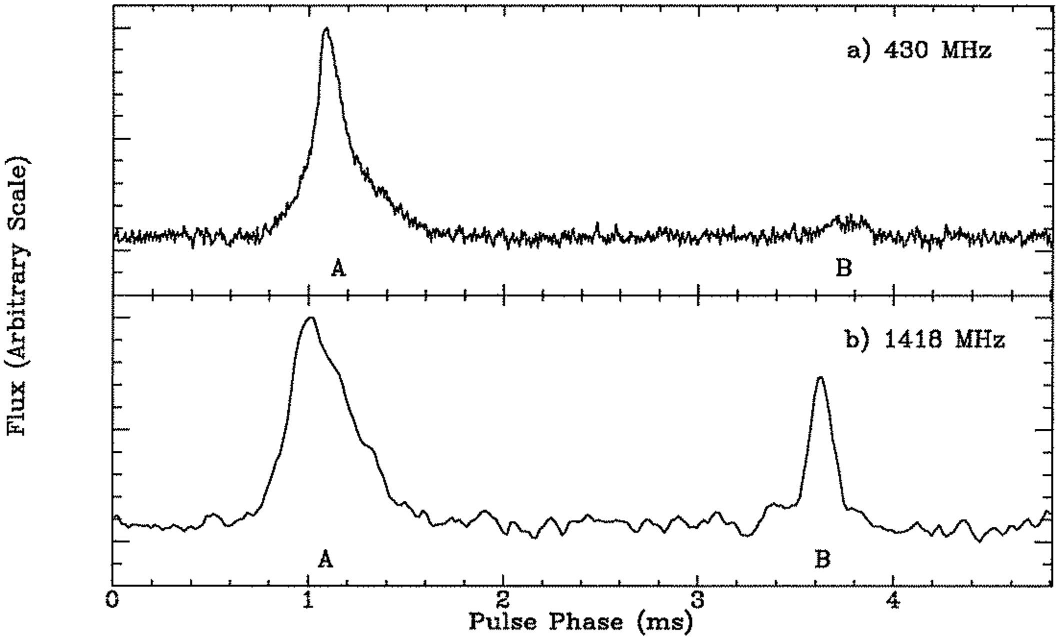

Figure 7.1: Profile of PSR J2322+2057 at (a) 430 MHz (coherently de-dispersed data) and (b) 1418 MHz (filterbank data).

lated field millisecond pulsar, PSR B1937+21. The wide separation of the components suggests this pulsar is an "orthogonal rotator," that is, its magnetic dipole axis and its spin axis are close to 90° apart. The resulting emission pattern, consistent with a line of sight along the pulsar's equator, would make both of the pulsar's magnetic poles visible, producing the widely separated components.

Polarization measures of this profile could confirm this guess about pulsar emission geometry. Unfortunately, the relatively weak flux from the pulsar, combined with the lack of a high-time-resolution, large-bandwidth polarization system at Arecibo make such a measure difficult, and it has not yet been done.

The average flux density of the pulsar at 430 MHz, as measured in timing observations, is 0.5±0.1 mJy. Because the distance to the pulsar is small, there are large variations in the observed signal due to interstellar scintillation. The average flux is below the detection threshold for the high latitude survey, so it

Table 7.1: Parameters of the PSR J2322+2057 system.[a]

Right ascension (J2000)[b]	$23^{\mathrm{h}}22^{\mathrm{m}}22^{\mathrm{s}}.357(1)$
Declination (J2000)[b]	$20^{\circ}57'02''.96(4)$
Right ascension (B1950)[c]	$23^{\mathrm{h}}19^{\mathrm{m}}52^{\mathrm{s}}.876(1)$
Declination (B1950)[c]	$20^{\circ}40'34''.94(4)$
Period (ms)	4.80842820962(2)
Period derivative (10^{-21})	6(7)
Epoch (MJD)	48653.0000
Dispersion measure (cm^{-3}pc)	13.3767(2)
Flux density, 430 MHz (mJy)	0.5(1)

[a] Figures in parentheses are uncertainties in the last digit quoted.

[b] J2000.0 coordinate system based on DE200 ephemeris (Standish 1982).

[c] B1950.0 coordinate system based on PEP740R ephemeris.

was only because of a particularly strong scintillation peak that the pulsar was detected. (In fact, while the pulsar was found during a confirmation session, it would not have been detected then had we not known its period and dispersion measure.)

7.2 Timing Observations

Timing data were collected and reduced to pulse times-of-arrival in the same manner as the data collected for J2019+2425 (see chapter 6). The timing model for this pulsar has only six parameters: two coordinates of pulsar position; pulse phase, period, and spin-down rate; and dispersion measure. The best-fit parameters are listed in table 7.1 and the residual times of arrival after subtracting the best-fit model are displayed in figure 7.2. The data quality varied somewhat, but the average uncertainty in a single day's observation reached a level of 2 μs when observations extended over the full 160 minutes during which the pulsar can be tracked at Arecibo.

The dispersion measure, combined with the pulsar position, suggests a

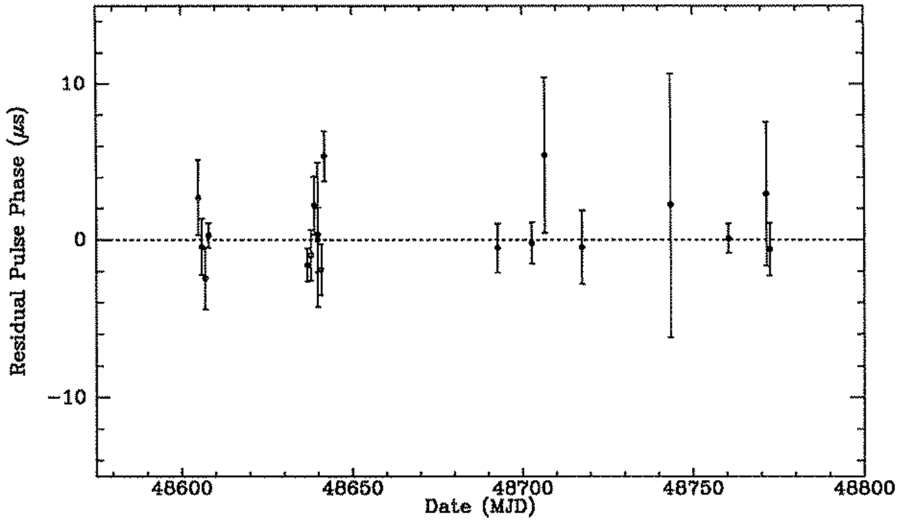

Figure 7.2: Pulse arrival times after subtracting a model based on the parameters in table 7.1 as a function of time.

distance of approximately 0.8 kpc using the model of Cordes and Taylor (1992). Its Galactic latitude is -37°, so it is about 0.5 kpc below the Galactic plane, confirming our expectation that millisecond pulsars would be found well off the plane. In addition to following the general trend of Galactic rotation, we expect the pulsar to have a large peculiar motion; in particular, we expect it to oscillate perpendicular to the Galactic plane. The perpendicular Galactic acceleration at this distance can be estimated by approximating the Galaxy as a uniform-density sheet. We will adopt the local column density, $\rho = 67\ \mathrm{M}_{\odot}\mathrm{pc}^{-2}$ (Bahcall 1984), as the mass density in the sheet. Acceleration is then $a = (\pi/2)G\rho$, so the time for a body to fall from $h = 0.5$ kpc to the plane, $t = (2h/a)^{1/2}$, is 5×10^7 yr. If the pulsar is near its maximum height at present, it must take $4t = 2 \times 10^8$ yr to make one full oscillation about the plane. (This is a minimum figure—if the pulsar travels further off the plane, the timescale is longer.) The parameters in table 7.1 suggest a lower limit of the age of the pulsar of 5.9×10^9 yr, though longer ages are not ruled out. This age is an order of magnitude greater than the oscillation time, so the pulsar must have traversed the plane several times.

7.3 Isolated Millisecond Pulsar Formation

Millisecond pulsars are believed to be formed by "spinning up" during an episode of mass and angular momentum accretion in a binary system. Most such recycled pulsars are found in binary systems; isolated millisecond pulsars can exist only if the binary system is somehow disrupted. There are three postulated methods by which isolated millisecond pulsars can be produced: first, the binary system can interact with a third body, possibly freeing the neutron star from the system. Alternately, in tight binaries, the pulsar wind can slowly evaporate its companion, as seen in the PSR B1957+20 and PSR B1744-24A systems (Fruchter, Stinebring & Taylor 1988; Lyne *et al.* 1990). Finally, if the companion is sufficiently massive, it can collapse in a supernova, possibly disrupting the binary system by its asymmetric explosion. Each of these scenarios has difficulty explaining the formation of PSR J2322+2057.

Three-body interactions are believed to be the source of isolated recycled pulsars in globular clusters. The fraction of recycled pulsars in clusters which are isolated is quite high; for example, four of the ten known pulsars in 47 Tucanae are isolated (Manchester *et al.* 1991). However, outside the cluster environment, the likelihood of a three-body interaction is low, so one is required to look for other mechanisms for freeing pulsars from their binary companions.

To explain the isolated pulsar B1937+21, Ruderman, Shaham, and Tavani (1989) suggested that the pulsar could eliminate its companion through interactions between the companion and a pulsar wind. A stellar companion in a tight orbit would intercept a large fraction of the pulsar's emitted energy, and this could heat and even evaporate the companion. Assuming a moment of inertia of 10^{45} cm^{2}g, the loss in rotational energy for a pulsar with period P and spin-down rate $\dot{P}$ is $\dot{E} = 4\pi \times 10^{45}\dot{P}/P^3$. The energy-loss rates are 1×10^{36} s^{-1}erg for the isolated pulsar B1937+21 and 2×10^{35} s^{-1}erg for B1957+20, which is known to be slowly evaporating its companion. The energy-loss rate for J2322+2057 is at most 5×10^{33} s^{-1}erg, suggesting it may not have had a sufficiently strong wind to ablate its companion. On the other hand, there has long been speculation that pulsar magnetic fields (and therefore period derivatives and energy-loss rates) decay over time, so perhaps J2322+2057 once had a stronger wind.

There are five known pulsars which are members of neutron star-neutron star systems. In each case, it is believed that the observed pulsar was formed while its companion was still a massive star, and that the massive star later underwent a supernova explosion. In some instances it might be expected that such a supernova explosion would disrupt the orbital system, freeing the pulsar. J2322+2057 could have been formed as an isolated pulsar in this way; however, it is interesting to note that its period (under 5 ms) stands in stark contrast with the periods of pulsars in orbit with other neutron stars (always at least 30 ms.)

7.4 Limits on Planetary Companions

Several apparent detections of planets around pulsars have been reported over the years, but generally they have not held up to closer scrutiny (e.g., Demiański & Prószyński 1979; Bailes, Lyne, & Shemar 1991; Lyne & Bailes 1992). The most compelling such claim to date has been the observation by Wolszczan and Frail (1992) of regular periodicities in pulse arrival times from the millisecond pulsar B1257+12, highly suggestive of two planets in nearly circular orbits around the pulsar. The orbital periods of the planets are 66.6 and 98.2 days, and the projected orbital radii are 1.31 and 1.41 light-ms, respectively. These figures yield lower limits on masses of 3.4 $M_\oplus$ and 2.8 $M_\oplus$ for the planets (Wolszczan & Frail 1992).

PSR B1257+12 is similar to PSR J2322+2057 in that it is out of the plane of the Galaxy, its period is a few milliseconds, and it has no stellar binary companion. One might anticipate, then, that J2322+2057 could also have

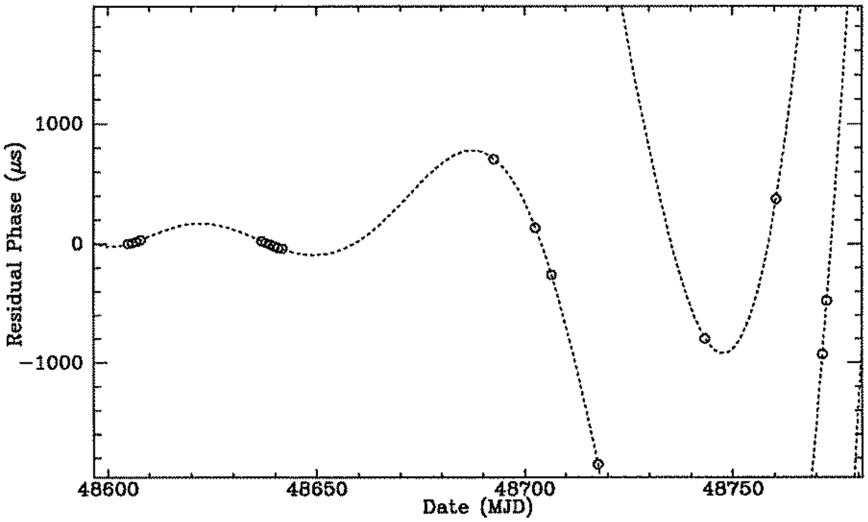

Figure 7.3: Residual arrival times as perturbed by a simulated planet. Compare with figure 7.2. Details of the simulated data are given in the text.

planetary companions.

We have analyzed the J2322+2057 data with this possibility in mind and we find no evidence for planets similar to those around B1257+12. Figure 7.3 shows the effect the outer B1257+12 planet would have on the timing residuals of J2322+2057. The figure was created by generating simulated pulse times of arrival (TOA's) assuming the (fictitious) planetary orbit and then fitting the TOA's to an isolated-pulsar model. Of course, the true effect of the planet would be to create a sinusoidal pattern in the residual phase. However, we made the "best fit" displayed in the figure by assuming no *a priori* knowledge of the planetary parameters. With only a limited number of data points, covariances between orbital parameters and isolated pulsar parameters distort the apparent effect of the orbit; further, with a sufficiently large planet orbit, there would be a strong possibility of mis-numbering pulses. In any case, such data could not be fit with an isolated-pulsar model and yield the observed small residuals with a spread of only a few microseconds.

We cannot reasonably expect to detect planets with periods longer than the 200 day span of our data set. To make a conservative estimate of our ability to detect planets with periods under 200 days, we will assume that any planet that would cause pulse times of arrival to vary with amplitude 10 μs or more would be detected. Using the relation

$$\frac{(M_2 \sin i)^3}{(M_1 + M_2)^2} = \frac{4\pi^2}{G} \frac{(a_1 \sin i)^3}{P_b^2} \tag{7.1}$$

along with an assumption that the pulsar has mass $M_1 = 1.4\ \mathrm{M}_\odot$, we can place an upper limit on planetary companion mass as a function of orbital period: $M_2 < 0.214\mathrm{M}_\oplus / \sin i P_b^{-2/3}$ where P_b is in days. This yields upper limits of $0.092\mathrm{M}_\oplus / \sin i$ for orbits of 20 days and $0.010\mathrm{M}_\oplus / \sin i$ for orbits of 100 days.

Planetary systems similar to that around PSR B1257+12 would have been detected by now. Instead, it is clear that PSR J2322+2057 is truly isolated.

Chapter 8

Applications of the Millisecond Pulsars

In this chapter we discuss some implications of the results of timing the newly discovered millisecond pulsars. We also estimate the measurability of several phenomena through hypothetical long-term timing programs.

8.1 Assumptions

In the following sections we use a combination of analytic and numerical techniques to analyze the accuracy to which various astrometric and relativistic phenomena can be measured. Several assumptions must be made to make these predictions. Except when explicitly looking for deviations from general relativity (GR), we assume GR to accurately describe gravitational interactions. We assume that "timing noise", unexplained long-period fluctuations seen in timing data of slow pulsars, will not bias millisecond pulsar results. We assume that interstellar propagation effects are negligible, or at least that they can be removed from the data by occasional multi-frequency observations.

We base numerical predictions on an extrapolation of our current observing program. We assume that the pulsars are observed using the Princeton Mark III pulsar timing system and the 430 MHz line feed at Arecibo as described in section 6.1.

At present, a millisecond pulsar timing program is under way at Arecibo. PSRs B1855+09, B1937+21, J2019+2425, and J2322+2057 are observed regularly (approximately bi-weekly); within an observing session, each of the pulsars is observed in turn following a fixed schedule. Because the first three pulsars are relatively close in the sky, they cannot each be observed for the full time they are visible from the telescope. In particular, 2019+2425 is tracked only from its transit point to the point where it reaches zenith angle $z = 20°$ at the observatory. The resulting data series can be reduced to a single effective pulse time of arrival with average uncertainty 2.5 μs. Observations of PSR J2322+2057 are made through the entire time the pulsar is visible from the observatory, producing a timing point with accuracy 2.0μs. (The higher accuracy of J2322+2057 timing is because we are assuming that significantly longer observations of it are possible.) In our analysis below, we assume that similar biweekly observations will continue for periods of up to 10 years.

8.2 PSR J2019+2425 and General Relativity

There are three distinct ways in which Newtonian models of pulsar binary systems have been shown to be inadequate to describe observed pulse arrival times; in these instances, general relativity must be included in the timing model. Two of these effects involve secular changes in orbital elements of the binary systems (in particular, precession and decay of the orbit) and will not be measurable in the J2019+2425 system in a reasonable time period. Our ability to measure the third effect, a delay in pulse arrival times during certain portions of the orbit, depends heavily on the (unknown) orientation of the orbit relative to the plane of the sky, but unless we are exceedingly lucky it too will be unmeasurable. We discuss each of these phenomena below, estimating their measurability using current equipment.

8.2.1 Precession of the Orbit

Orbital precession is a well known effect of GR. Indeed, it was the small but persistent advance of perihelion of Mercury's orbit around the sun which first indicated that Newton's laws were not sufficient to explain orbital dynamics. The rate of advance of periastron in an orbit is (Will 1981, p. 294)

$$\dot{\omega} = \frac{6\pi G M_2}{c^2 P_b a_1 (1 - e^2)} \tag{8.1}$$

where ω is the angle of periastron, e is the orbital eccentricity, M_2 is the secondary mass, P_b is the orbital period, a_1 is the primary orbital semi-major axis, G is the gravitational constant, and c is the speed of light. Since the values of a_1 and M_2 depend on the unknown inclination angle i, the precise $\dot{\omega}$ value for J2019+2425 cannot be calculated. However, the dependence of $\dot{\omega}$ on i is sufficiently weak that a reasonably robust estimate can be made assuming an edge-on orbit ($i = 90°$). Assuming also that the pulsar mass is $M_1 = 1.4\ \mathrm{M}_\odot$, we find $\dot{\omega} = 2 \times 10^{-4}$ deg/yr.

With data collected over about 1 year, the angle of periastron ω has been measured to $\delta\omega = 0.02°$ precision (see table 6.2). If a similar set of measurements were made in the subsequent year, we could estimate

$$\dot{\omega} \simeq (\omega(t_1) - \omega(t_0))/(t_1 - t_0) \tag{8.2}$$

where t_0 and t_1 are central epochs of the data sets. The accuracy of the $\dot{\omega}$ measure would then be $\sim 2^{1/2}\delta\omega/(t_1 - t_0) = 0.03$ deg/yr, two orders of magnitude shy of the expected GR value.

The uncertainty of a $\dot{\omega}$ measurement derived from regularly sampled data is proportional to $T^{-3/2}$ where T is the total timespan of the observations. (A factor of T^{-1} comes from the differential formula for $\dot{\omega}$; a further $T^{-1/2}$ comes from the increased number of observations.) Using the values calculated above, it would take about 30 years to marginally detect the precession of J2019+2425's orbit.

8.2.2 Gravitational Radiation

Gravitational radiation is emitted by a rotating system in proportion to the third time derivative of the quadrupole moment of that system. The emission of gravitational radiation can be inferred from observations of pulsars in neutron star–neutron star binary systems, such as that of PSR B1913+16 (Taylor & Weisberg 1989). Energy is released by the orbit to produce the radiation, and the resulting lower-energy orbit has a shorter orbital period.

The observed change in binary period is (Will 1981, p. 198)

$$\dot{P}_b/P_b = -\frac{96}{5}\frac{\mu m^2}{a^4}\frac{G^3}{c^5}F(e) \tag{8.3}$$

$$F(e) = (1 + \frac{73}{24}e^2 + \frac{37}{96}e^4)(1 - e^2)^{-7/2}, \tag{8.4}$$

where $m = M_1 + M_2$ and μ is the reduced mass $M_1M_2/(M_1 + M_2)$. For the J2019+2425 orbit, we can approximate $e = 0$, so $F(e) = 1$. Assuming $i = 90°$, and using the parameters in table 6.2, we calculate $\dot{P}_b/P_b = 2.4 \times 10^{-14}$ yr^{-1}, or $\dot{P}_b = 5 \times 10^{-15}$.

Again we can estimate the length of time it would take to make a nonzero measure of this effect, assuming regular observations of the pulsar are made. Uncertainty of the $\dot{P}_b$ measure is proportional to $T^{-5/2}$, where T^{-2} is attainable because $\dot{P}_b$ is a function of the second derivative of orbital phase and a further $T^{-1/2}$ comes from continuously increasing the number of measurements made. Table 6.2 gives an estimated uncertainty of $\delta P_b = 0.2$ s over about 1 yr of measurement. The uncertainty on $\dot{P}_b$ is then $\sim 0.3\text{s}/1\text{yr} = 9 \times 10^{-9}$. Using the $T^{-5/2}$ scaling law, we estimate observations would take over 300 yr to reach the precision of 5×10^{-15} needed to measure the radiation. (It seems unlikely the Observatory would approve of such a program!)

8.2.3 Shapiro Delay

It was recognized by Shapiro (1964) that pulsed signals traversing a gravitational potential well would accumulate a measurable time delay. The first experimental verification of this phenomenon was made in interplanetary radar experiments in which the signal propagation was delayed as it passed close to the sun. This effect can be measured in pulsar systems when the pulsar–earth line of sight passes sufficiently close to the orbital companion. Nonzero Shapiro parameters have been measured in two pulsar systems to date and have been used to deduce the inclination of the orbit and the masses of the pulsars and companions in these systems (Ryba & Taylor 1991; Wolszczan 1991).

Neglecting eccentricity, the delay in the pulse signal due to this effect is (Ryba & Taylor 1991)

$$\Delta = 2r \log_e(1 + s\cos\theta) \tag{8.5}$$

where $r \equiv GM_2/c^3$; s is the sine of the orbital inclination angle i; and θ is the position of the pulsar within its orbit. (As an order-of-magnitude estimate, $r = 1.56\ \mu s$ for the minimum J2019+2425 companion mass 0.316 $M_\odot$, calculated assuming a 1.4 $M_\odot$ pulsar mass.) It is clear from equation 8.5 that the magnitude of the observed Shapiro delay is highly dependent on orbital inclination: if we are looking at the orbit "edge on," the line of sight between the pulsar and the earth will pass close to the companion, and the magnitude of the effect will be large; conversely, the effect is not measurable in a "face-on" system.

To test our ability to measure the Shapiro delay, an analysis was run on simulated 5- and 10-year timespans of J2019+2425 data as discussed above. Since the inclination angle is not known, we ran simulations at a variety of values of i. The simulations were performed using the Tempo software package. "Perfect" data were created, noise was added, and the resulting TOA's were fit to the standard spin-down, astrometric, and binary parameters, as well as the Shapiro parameters. To relate the results of the simulations to a physically interesting parameter, we have plotted the measurement uncertainty of the companion mass as a function of inclination angle in figure 8.1. It can be seen that unless the inclination angle is greater than $\sim 84°$ (i.e., $\sin i > 0.996$), it will be difficult to make a useful measure of the companion mass.

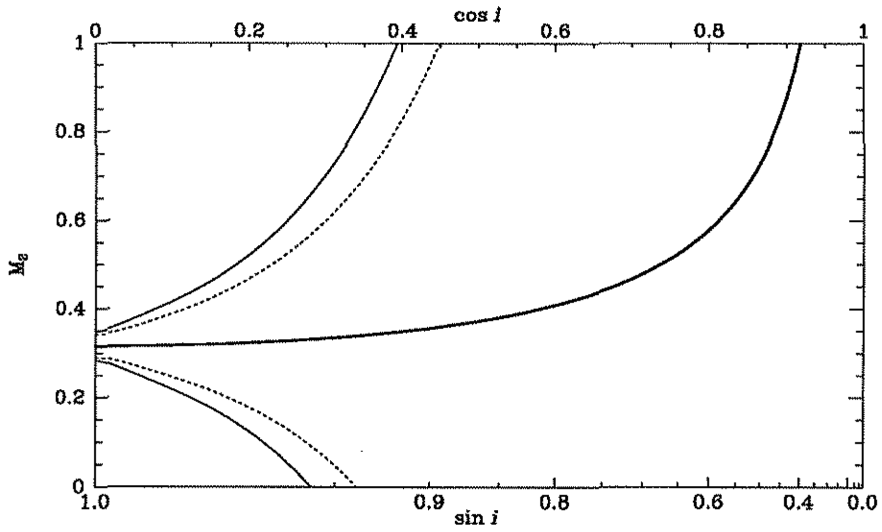

Figure 8.1: Projected uncertainty in measurements of the Shapiro effect. The central line is the value of the J2019+2425 companion mass M_2 as a function of inclination angle i assuming a pulsar mass of $M_1 = 1.4\ \mathrm{M}_\odot$. The plot is linear in $\cos i$, as is the *a priori* probability of the orbital inclination. The broken lines bracket the 1σ range expected of measurements of M_2 derived from the Shapiro effect over a five-year timing experiment; the outer solid lines represent the expected uncertainties in a ten-year experiment.

The likelihood of this is slim, around 10% if we assume the orbit to be randomly oriented. On the other hand, this effect has been observed in B1855+09, despite a similarly low *a priori* probability (Ryba & Taylor 1991). If our probability estimate is wrong, and pulsar systems at large inclination angles are more likely to be discovered, then the chance of measuring the Shapiro delay in 2019-like systems increases. Such a bias could exist if the pulsar angular momentum vector and the orbital angular momentum vector were close to alignment (an expected result in the "spin-up" scenario for millisecond pulsar formation), and if the pulsar were an "orthogonal rotator," that is, if its magnetic and rotation axes were perpendicular, making its emission region equatorial.

8.3 PSR J2019+2425 and the Gravitational "Constant" G

8.3.1 Orbital Effects

In general relativity, the coupling value G, traditionally referred to as the gravitational constant, is a time-independent quantity. The strictest limits on changes in G have come from observations of the stability of orbital systems. If there were a nonzero $\dot{G}$, an orbital system of two point masses would experience a change in orbital period over time (in addition to any changes due to gravitational radiation). Damour, Gibbons, and Taylor (1988) show that if the only significant effect of changing G is a change of its value in the quadrupole formula then

$$\left(\frac{\dot{P}_b}{P_b}\right)_{\rm obs} - \left(\frac{\dot{P}_b}{P_b}\right)_{\rm GR} = -2\left(\frac{\dot{G}}{G}\right). \tag{8.6}$$

Various ranging and position observations within the solar system, most notably radar ranging between the Earth and Mars, have allowed the construction of a model of solar system dynamics with $\dot{G}/G$ as a free parameter. The resulting measure of $\dot{G}/G$, actually an upper limit, is $s \pm 4 \times 10^{-12}$ yr^{-1} (Hellings *et al.* 1983), although another analysis of the same data has produced a somewhat weaker limit (Reasenberg 1983). The measurement is limited by uncertainties in the model of the asteroid belt.

Binary pulsar systems are "cleaner" than the solar system in the sense that they have only two bodies. On the other hand, they are complicated by the possible presence of relativistic effects and by the possible effect of $\dot{G}$ on the structure of neutron stars. Damour and Taylor (1991) have calculated $\dot{G}/G = 1.10 \pm 1.07 \times 10^{-11}$ yr^{-1} for PSR B1913+16, and they estimate that a limit of 3×10^{-12} can be achieved by continued observations of this pulsar. (The ultimate limit reflects uncertainties in Galactic acceleration of the binary system, which will induce a spurious observed $\dot{P}_b$.) A somewhat better limit might be expected from the relativistic binary system PSR B1534+12 as it is closer to the earth and the acceleration uncertainties are smaller.

The B1913+16 limits on $\dot{G}/G$ were calculated under the assumption that the pulsar is a point mass. In reality, of course, it is not, and in fact it has substantial gravitational self-energy. This energy is proportional to G, so a change in G will change the mass of the pulsar (as well as its neutron star companion). Since the detailed structure of neutron stars is not known, the size of this effect is unclear. Following Nordvedt (1990), we use the gravitational self-energy

$$E_g = -\frac{G}{2}\sum_{i,j}\frac{m_i m_j}{r_ij} \tag{8.7}$$

to define a "compactness" parameter for each body

$$c = \frac{G}{m}\frac{\delta m}{\delta G} = \frac{E_g}{mc^2}. \tag{8.8}$$

Changes in the orbital period can then be related to changes in the gravitational constant by

$$\frac{\dot{P}_b}{P_b} = -\left(2 + 2\left(\frac{m_1c_1 + m_2c_2}{m_1 + m_2}\right) + 3\left(\frac{m_1c_2 + m_2c_1}{m_1 + m_2}\right)\right)\frac{\dot{G}}{G}. \tag{8.9}$$

For a neutron star–neutron star system such as B1913+16, where $c_1 \simeq c_2$ and $m_1 \simeq m_2$ this reduces to

$$\frac{\dot{P}_b}{P_b} = -(2 + 5c)\frac{\dot{G}}{G}. \tag{8.10}$$

The value of c is not well known. Nordvedt (1990) suggests it falls in the range -0.39 to -0.15, possible reducing the induced period change significantly, and making the $\dot{G}/G$ measure by pulsar timing more difficult.

For PSR J2019+2425, as well as other neutron star–white dwarf binary systems, the compactness of the dwarf companion can be ignored, so equation 8.9 reduces to

$$\frac{\dot{P}_b}{P_b} = -\left(2 + c_1\left(1 + \frac{m_2}{m_1 + m_2}\right)\right)\frac{\dot{G}}{G}, \tag{8.11}$$

and the effect of the neutron star structure term is reduced. In section 8.2.2 we estimated the uncertainty of $\dot{P}_b$ to be 6×10^{-9} in one year of observations, with $T^{-5/2}$ scaling to the total length of observations. This uncertainty is equivalent to an uncertainty in $\dot{P}_b/P_b$ of 3×10^{-8} yr^{-1}. To reach an interesting level of 10^{-11} yr^{-1} would take approximately 25 years of timing data.

8.3.2 Spin-down Effects

Structural changes within compact bodies due to changes in G would modify not only the total masses of the bodies but also their moments of inertia. Counselman and Shapiro (1968) pointed out that a reduction in G would cause a pulsar to increase its moment of inertia while conserving angular momentum, thus reducing its rotation frequency. The exact relation between the induced spin-down (which would be in addition to the normal magnetic-braking spin-down) and the change in G depends on the (unknown) structure of the neutron stra, but dimensional analysis suggests

$$\frac{\dot{G}}{G} = \alpha \frac{\dot{P}}{P}. \tag{8.12}$$

The right hand side of this equation is proportional to the reciprocal of the conventionally defined pulsar spin-down age, so the limit on changes in G using this technique is directly related to the age of the oldest known pulsar. Since J2019+2425 has the largest pulsar age (see section 6.3), it provides the best limits using this technique.

Goldman (1990) considered several equations of state and found that α is likely in the range 0.2–0.5 for a neutron star with mass 1.4–1.5 $M_\odot$. He used the parameters of PSR B0655+64 to derive the limit $\dot{G}/G \leq (2.2 - 5.5) \times 10^{-11}$ yr^{-1}. Since J2019+2425 has twice the age of B0655+64, we can use the same logic to reduce the limit on changes in G to

$$\frac{\dot{G}}{G} \leq (1.1 - 2.8) \times 10^{-11} \text{ yr}^{-1}. \tag{8.13}$$

While this limit is weaker than those derived from the solar-system model and the PSR B1913+16 orbit, the uncertainties involved are different from those limiting the other techniques, so it is still an interesting confirmation of the constancy of G.

8.4 The J2019+2425 Orbit and the Strong Equivalence Principle

The strong equivalence principle (SEP) states that inertial mass and gravitational mass are the same quantity—in other words, the "m"s in $F = ma$ and $F = Gm_1m_2/r^2$ are the same. Strict limits have been put on violations of this principle in ordinary matter by Eötvös (1890) and Roll, Krotkov, and Dicke (1964). The latter defined

$$\mu_0(A, B) = 2\frac{(m_g/m_i)_A - (m_g/m_i)_B}{(m_g/m_i)_A + (m_g/m_i)_B} \qquad (8.14)$$

as a parameter measuring the differences in inertial versus gravitational masses for two substances A and B, and, through a torsion-balance experiment, found a limit $|\mu_0| < 3 \times 10^{-11}$ using gold and aluminum masses.

This limit has not been surpassed; however, the small masses used to make the measurement had negligible gravitational self-energy, leaving open the possibility that the extra mass-energy in denser (or larger) objects would not obey the strong equivalence principle. We define gravitational self-energy as $E_g/mc^2 = Gm/ac^2$, where a is the characteristic size of the mass. Representative values are 10^{-25} for laboratory test bodies, 5×10^{-10} for the earth, 10^{-5} for the sun, and 0.15 for a neutron star.

Nordvedt (1968a, 1968b) pointed out that lunar ranging experiments could put limits on violations of the SEP if the violations took the form of nonzero μ_1 in $m_g/m_i = 1 + \mu_1(E_g/mc^2)$. The self-energy of the earth would modify the behavior of the earth-moon orbital system in the presence of the gravitational field of the sun. The experiment was carried out, and a null result was found: $\mu_1 = 0.001 \pm 0.015$ (Williams *et al.* 1976; Shapiro, Counselman & King 1976).

The lunar ranging limit does not preclude violations of the equivalence principle which depend on higher-order contributions of the self-energy, in particular nonzero μ_2 in the expansion

$$m_g/m_i = 1 + \mu_1(E_g/mc^2) + \mu_2(E_g/mc^2)^2 + \cdots . \qquad (8.15)$$

Such nonzero values of μ_2 are allowed in some alternative gravity theories which fix $\mu_1 = 0$ (Damour & Esposito-Farèse 1992).

Damour and Shäfer (1991) used the existence of long-period binary pulsar systems with nearly circular orbits to put a limit on μ_2. For neutron stars the $(E_g/mc^2)^2$ term in equation 8.15 is non-negligible. Neutron stars in wide binary orbits are affected by the Galactic gravitational potential in the same sense as the earth-moon system interaction is affected by the sun's potential. Uncertainties involved in analyzing pulsar binary systems, in particular their uncertain angle of inclination on the sky and their uncertain angle of inclination relative to the Galactic center, make analysis of these systems less robust than solar system experiments. However, it can be shown (Damour & Schäfer 1991) that an SEP violation would induce a slight eccentricity into an otherwise circular orbit. The existence of near-circular orbits, then, can be used to limit SEP violations. They put a limit of $|\mu_2| < 1.1 \times 10^{-2}$ using the eccentricity ($e = 3.304 \times 10^{-4}$) and binary period ($P_b = 1.013 \times 10^7$ s) of PSR B1953+29. Their limit on μ_2 is proportional to P_b^2/e, with a weak (and in our case negligible) dependence on pulsar position (which factors into the Galactic acceleration and relative orientation distributions.) Therefore we can use PSR J2019+2425's parameters, $e = 1.11 \times 10^{-4}$ and $P_b = 6.61 \times 10^6$ s, to put a marginally better limit on SEP violations: $|\mu_2| < 0.9 \times 10^{-2}$. The reader is referred to Damour and Shäfer (1991) for detailed calculation of this effect.

8.5 Proper Motion and Parallax

Any model of terrestrial pulse arrival times must include the travel time across the orbit of the earth. This travel time varies depending on the position of the earth and the direction of the incoming signal, so it depends on the pulsar's position. If the pulsar's position changes over time, this too must be incorporated in the model. Proper motions of several slow pulsars have been measured using timing data (Helfand *et al.* 1980), but VLBI observations have shown that such observations can be contaminated by timing noise (Lyne, Anderson & Salter 1982). However, so far as is known, timing noise is negligible for millisecond pulsars. The effect of proper motion on pulse times of arrival is shown in figure 8.2.

Slow pulsars typically have velocities up to several hundred kilometers per second (Lyne, Anderson & Salter 1982), and one pulsar has been suggested to have a velocity of 2300 km/s (Frail & Kulkarni 1991). Whether recycled pulsars achieve such high velocities is still an open question. Ryba (1991) measures a velocity of 75 km/s for B1937+21, 33 km/s for B1855+09, and 120 km/s for B1957+21, all in the lower part of the slow-pulsar range, but all also in the Galactic plane.

We simulated 1-, 5-, and 10-year spans of bi-weekly observations of both new millisecond pulsars to assess the measurability of their proper motions. Since proper motion is a differential with respect to time, the precision with which it can be measured is proportional to $T^{-3/2}$ if regularly spaced observations are made over time T. Thus proper motion can be measured much more easily over a longer timespan.

For PSR J2019+2425, the dispersion-derived distance to the pulsar is 1 kpc. Simple trigonometry gives

$$\mu(\mathrm{mas/yr}) = 0.211 v_t(km/s) \tag{8.16}$$

where v_t is the transverse velocity of the pulsar in the solar system frame of rest. Measurement uncertainties of proper motion in declination are $\delta\mu_\delta = 76$, 0.14, and 0.05 mas/yr with simulated observations over 1, 5, and 10 years. The uncertainties of proper motion in right ascension are $\delta\mu_\alpha = 30$, 0.09, and 0.03 mas/yr over the same timespans. These measurement uncertainties correspond to transverse velocities of 390, 0.7, and 0.3 km/s. Clearly within a few years the proper motion (and hence the transverse velocity) of this pulsar will be measured.

Similar simulations for PSR J2322+2057 result in estimated uncertainties $\delta\mu_\delta = 95$, 0.17, and 0.06 mas/yr and $\delta\mu_\alpha = 57$, 0.10, and 0.04 mas/yr, for 1, 5, and 10 year observing campaigns. At a distance of 0.8 kpc, the proper motion

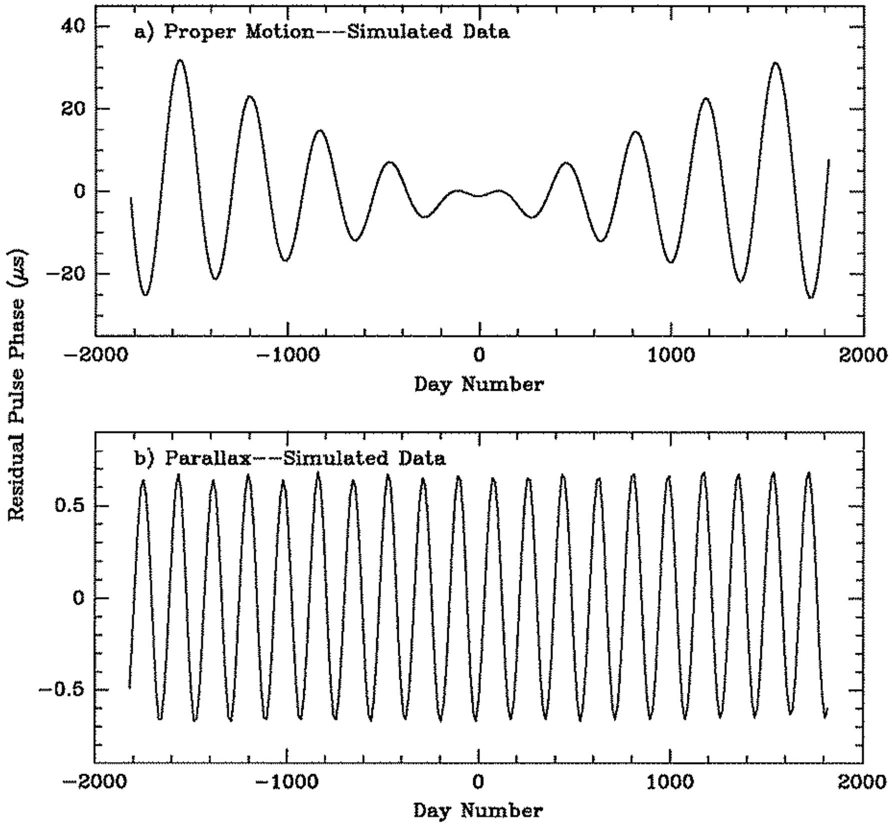

Figure 8.2: Simulated residual pulse arrival times for PSR J2322+2057 incorporating (a) proper motion and (b) parallax. The proper motion plot was made by assuming 2 mas/yr motion in both right ascension and declination, which translates to a very small 7 km/s motion in the sky at the nominal distance of 770 pc. The true signal will likely be much larger than this. The parallax residuals correspond to $\pi = 1.30$ mas, the parallax expected from the 770 pc distance.

and transverse velocities are related by

$$\mu(\text{mas/yr}) = 0.274 v_t(km/s) \tag{8.17}$$

which yields $v_t = 400$, 0.7, and 0.3 km/s resolution for the simulated measurements.

Parallaxes—periodic changes in the pulsars' apparent positions relative to a reference frame based on distant objects—are much more difficult to measure. The effect on timing data does not accumulate over time as proper motion effects do. The effect is also much lower in amplitude (see figure 8.2). The estimated distance of 1 kpc and 770 pc to J2019+2425 and J2322+2057 correspond to parallaxes of $\pi = 1$ mas and $\pi = 1.25$ mas, respectively. Estimated uncertainties in parallax measures over 10 years of observations are 0.7 mas and 1.1 mas, respectively, so the effect will be marginally visible at best. Only through a significant increase in observation rate or timing accuracy could distances to these pulsars be measured through timing.

8.6 Conclusion

The most esoteric, but perhaps the most interesting, potential application of millisecond pulsar timing data is its use to detect (or limit) the presence of a background of long-wavelength gravitational waves. Small perturbations in pulse times of arrival from a pulsar could suggest the presence of such a background. Current standard clocks and solar system ephemerides are not sufficiently accurate to measure such perturbations and therefore a redundant array of pulsars spread throughout the sky is needed for such a project. Detailed discussions of this concept can be found in Foster (1990), chapter 5 of Thorsett (1991), Stinebring *et al.* (1990), and Romani (1989).

Any results from such a project are a long ways off. Fortunately, as we have shown, the discovery and observation of the two new millisecond pulsars will provide several interesting astrophysical results within a shorter time period. The surveys have taken a large amount of human effort, telescope time, and computer resources; but in light of the science which continues to emerge from the pulsars discovered, the investment has been worthwhile.

Appendix A

Autocorrelation Spectroscopy

The Wiener-Khinchin Theorem, also called the Autocorrelation Theorem, states that the Fourier transform of an autocorrelation is a power spectrum (e.g., Bracewell 1965). In other words, if $\mathcal{F}(\nu)$ is the Fourier transform of $f(t)$, then

$$|\mathcal{F}(\nu)|^2 = \int_{-\infty}^{\infty} d\tau \int_{-\infty}^{\infty} dt\, f(t) f^*(t-\tau) e^{i2\pi\tau\nu}. \qquad \text{(A.1)}$$

Measurement of the power spectrum $|\mathcal{F}(\nu)|^2$ is a necessary part of most radio astronomy observations. In our search projects, for instance, the data had to be in this "filterbank" form to be analyzed. Direct measurement of the power spectrum, either through Fourier analysis of the incoming signal or through the use of filterbanks, can be difficult. Autocorrelation hardware is easier to implement. To measure an autocorrelation function, the incoming signal is digitized, stored on a delay line, and the summed product of each delayed signal with the new incoming signal must be accumulated. The number of lags stored in the delay line is proportional to the resolution of the spectrum.

The autocorrelation functions must be transformed into power spectra off-line after the observation. Since $f(t)$ is a real signal, we can ignore the imaginary part of $e^{i2\pi\tau\nu}$ in equation A.1 and write

$$\int_{-\infty}^{\infty} d\tau\, A(\tau) \cos(2\pi\tau\nu) = |\mathcal{F}(\nu)|^2 \qquad \text{(A.2)}$$

where we have defined the autocorrelation function $A(\tau) \equiv \int dt\, f(t) f(t-\tau)$. In practice, then, a cosine transformation of each autocorrelation function must be calculated. The discrete case is a trivial extension of this formula.

The Arecibo-Berkeley 40 MHz correlator was used for data acquisition in the Galactic plane pulsar survey. (40 MHz refers to an internal clock speed in the instrument.) In our configuration, the correlator operated in parallel on several 2.5 MHz passbands. The undetected signal from each passband was measured and correlated with itself. The incoming signal was digitized to $+1$ if over a voltage threshold $+\alpha$, -1 if below $-\alpha$, and 0 if in between. The value of α was set to approximately 0.6σ, where σ denotes the rms fluctuation of the incoming signal; this minimizes the loss of information due to three-level sampling, but this loss is still significant. Sampling at the Nyquist rate (in our case 5 MHz) would reduce the eventual signal-to-noise ratio of our data by 1.25. The coarse quantization effectively increases the bandwidth of the signal, however, so sampling more frequently than the Nyquist rate will reduce this loss. In our project the 2.5 MHz passbands were sampled at the double Nyquist rate of 10 MHz, resulting in only a 13% loss in SNR. Details of these calculations can be found in Hagen (1985).

The passband shape from correlator data, once processed into a power spectrum, is the same as that produced by a Fourier analysis. Press *et al.* (1986) give the leakage function as

$$a(s) \sim \frac{1}{N^2}\left(\frac{\sin(s\pi)}{\sin(s\pi/N)}\right)^2, \tag{A.3}$$

where N is the number of lags and $s \equiv (\nu - \nu_0)(N/\delta\nu)$, $\delta\nu$ the bandwidth, f the frequency. For N large this is approximately

$$\begin{aligned} a(s) &\sim \frac{1}{N^2}\left(\frac{\sin(s\pi)}{s\pi/N}\right)^2 && \text{(A.4)} \\ &= \mathrm{sinc}^2(s) && \text{(A.5)} \end{aligned}$$

where

$$\mathrm{sinc}(x) \equiv \sin(x\pi)/x\pi. \tag{A.6}$$

In the notation of section 2.4, we have transmission function

$$a(\nu) = \frac{1}{\delta\nu}\,\mathrm{sinc}^2((\nu - \nu_0)/\delta\nu) \tag{A.7}$$

where $\delta\nu$ is the spacing between effective filterbank channels after transforming the autocorrelation function, and the initial constant factor provides normalization $\int_{-\infty}^{\infty} d\nu\; a(\nu) = 1$. The transmission function then has Fourier transform (Bracewell 1965)

$$\mathcal{A}(f) = \Lambda(f\delta\nu) \tag{A.8}$$

where

$$\Lambda(x) = \begin{cases} 1 - |x| & |x| < 1 \\ 0 & \text{elsewhere.} \end{cases} \tag{A.9}$$

Autocorrelations are collected for some finite integration time $t_s \gg n_{lag} t_f$, where t_f denotes the digitization rate of the unsampled data. The sampling function is therefore a boxcar:

$$r(t) = \begin{cases} 1 & -1/2t_s < t < 1/2t_s \\ 0 & \text{elsewhere,} \end{cases} \tag{A.10}$$

and its transform is a sinc function:

$$\mathcal{R}(f) = \mathrm{sinc}(ft_s). \tag{A.11}$$

Appendix B

Noise Statistics

Our ability to detect pulsars is limited by fluctuations in the background noise. In each of the search programs we analyzed a large number of combinations of potential pulsar positions, periods, and dispersion measures, and for each combination there is an independent variable which signals the presence (or absence) of pulsars. Because of the large number of such variables analyzed, small 1 and 2σ fluctuations are commonplace, and the threshold for detection of signals must be set higher. In this appendix we make an analytical calculation of the minimum signal-to-noise ratio (SNR) needed for a pulsar to be detected given the parameters of our searches.

We begin by assuming that elements of the data time series are uncorrelated, as would be true if the passband had a perfect boxcar shape and the sampling rate was exactly the Nyquist frequency. Then the components (real part and imaginary part) of the complex coefficients of the Fourier transforms are composed of weighted sums of many numbers. By the central limit theorem these components must have a Gaussian distribution:

$$p(x) = (2\pi)^{-1/2}\sigma^{-1}\exp\left(-\frac{1}{2}\left(\frac{x-\mu}{\sigma}\right)^2\right). \tag{B.1}$$

For white noise there will be no bias in the transform, i.e., $\mu = 0$. Fluctuation spectra are constructed from the amplitudes of complex Fourier coefficients. For each Fourier coefficient $a + ib$ there is a corresponding element of the spectrum $c = (a^2 + b^2)^{1/2}$. The statistics of c determine our ability to detect signals.

The sum of the squares of n variables (each of which has an independent Gaussian distribution) are described by the χ^2 distribution. The general form of this distribution is

$$f(\chi^2) = \frac{(\chi^2)^{\frac{n}{2}-1}e^{-\frac{x^2}{2}}}{\Gamma(\frac{n}{2})2^{\frac{n}{2}}}. \tag{B.2}$$

where Γ is the "gamma function",

$$\Gamma(z) = \int_0^\infty du\, e^{-u}u^{z-1}. \tag{B.3}$$

Thus the distribution of c^2, the squares of the amplitudes of Fourier transform elements, should follow a χ^2 distribution in the absence of periodic signals due to pulsars or interference. With $n = 2$, equation B.2 reduces to

$$f(c^2)\, dc^2 = (1/2)\exp(-c^2/2)dc^2. \tag{B.4}$$

In the search code, the reported SNR is a scaled version of c:

$$\mathrm{SNR} = \frac{c - \bar{c}}{\sigma_c} \tag{B.5}$$

where $\bar{c}$ and σ_c are the mean and rms values for the c's in the array under consideration. The distribution function for c (equation B.4) can be used to calculate these values:

$$\begin{aligned} \bar{c} &= \int_0^\infty dc^2\, c\,(1/2)e^{-\frac{c^2}{2}} && \text{(B.6)} \\ &= \frac{1}{2}\int_0^\infty dx\, x^{\frac{1}{2}}e^{-\frac{x}{2}} && \text{(B.7)} \\ &= \left(\frac{\pi}{2}\right)^{\frac{1}{2}} \approx 1.2533 && \text{(B.8)} \end{aligned}$$

$$\begin{aligned} \sigma_c^2 &= \langle c^2\rangle - \bar{c}^2 && \text{(B.9)} \\ &= \int_0^\infty dc^2\, c^2\,(1/2)e^{-\frac{c^2}{2}} - \left(\frac{\pi}{2}\right) && \text{(B.10)} \\ &= \frac{1}{2}\int_0^\infty dx\, xe^{-\frac{x}{2}} - \frac{\pi}{2} && \text{(B.11)} \\ &= 2 - \frac{\pi}{2} && \text{(B.12)} \\ \sigma_c &\approx 0.655 && \text{(B.13)} \end{aligned}$$

The searches discussed in chapters 4 and 5 had of order $4096 = 2^{12}$ independent beam areas. In each beam area, power spectra had $65,536 = 2^{16}$ independent measures of the variable c. There was some redundancy in the dispersion measure calculations, but at least $32 = 2^5$ independent values of DM were constructed using full-length time series in each search. Thus a total of 2^{33} independent variables were analyzed for potential pulsar signals in each survey. To detect signal, it must have a SNR larger than the largest noise fluctuations, i.e., it must be above a threshold value c_{thresh} such that the likelihood of chance occurrence of c at or above this value is less than 2^{-33}. The probability integral is

$$\int_{c^2_{\mathrm{thresh}}}^{\infty} dc^2\,(1/2)\exp(-c^2/2) = \exp(-c^2_{\mathrm{thresh}}/2). \tag{B.14}$$

Setting this to 2^{-33} gives $c_{\mathrm{thresh}} = 6.76$; scaling using equation B.5 gives $\mathrm{SNR}_{\mathrm{thresh}} = 8.4$. Thus we expect to be able to distinguish signals from noise at about the 8.4σ level.

In practice we found that spurious "detections" became common below the 8σ level, and we used this empirical value as our cutoff.

References

Backer, D. C., Kulkarni, S. R., Heiles, C., Davis, M. M., and Goss, W. M. 1982, *Nature*, **300**, 615.

Bahcall, J. H. 1984, *Astrophys. J.*, **276**, 169.

Bailes, M., Lyne, A. G., and Shemar, S. L. 1991, *Nature*, **352**, 311.

Bhattacharya, D. and van den Heuvel, E. P. J. 1991, *Phys. Rep.*, **203**, 1.

Biggs, J. D. and Lyne, A. G. 1992, *Mon. Not. R. astr. Soc.*, **254**, 257.

Bionta, R. M. *et al.* 1987, *Phys. Rev. Lett.*, **58**, 1494.

Bracewell, R. 1965, *The Fourier Transform and its Applications*, New York: McGraw–Hill.

Callanan, P. J., Charles, P. A., Hassal, B. J. M., Machin, G., Mason, K. O., Naylor, T., Smale, A. P., and van Paradijs, J. 1989, *Mon. Not. R. astr. Soc.*, **238**, 25P.

Clifton, T. R., Lyne, A. G., Jones, A. W., McKenna, J., and Ashworth, M. 1992, *Mon. Not. R. astr. Soc.*, **254**, 177.

Cordes, J. M. and Taylor, J. T. 1992, In preparation.

Cordes, J. M., Weisberg, J. M., Frail, D. A., Spangler, S. R., and Ryan, M. 1992, *Nature*, **354**, 121.

Counselman, C. C. and Shapiro, I. I. 1968, *Science*, **162**, 352.

Damashek, M., Taylor, J. H., and Hulse, R. A. 1978, *Astrophys. J.*, **225**, L31.

D'Amico, N., Manchester, R. N., Durdin, J. M., Stokes, G. H., Stinebring, D. R., Taylor, J. H., and Brissenden, R. J. V. 1988, *Mon. Not. R. astr. Soc.*, **234**, 437.

Damour, T. and Esposito-Farèse, G. 1992, *Class. Quant. Grav.* Submitted.

Damour, T., Gibbons, G. W., and Taylor, J. H. 1988, *Phys. Rev. Lett.*, **61**, 1151.

Damour, T. and Schäfer, G. 1991, *Phys. Rev. Lett.*, **66**, 2549.

Damour, T. and Taylor, J. H. 1991, *Astrophys. J.*, **366**, 501.

Davies, J. G., Lyne, A. G., and Seiradakis, J. H. 1977, *Mon. Not. R. astr. Soc.*, **179**, 635.

Demiański, M. and Prószyński, M. 1979, *Nature*, **282**, 383.

Dickel, H. R., Lortet, M.-C., and de Boer, K. S. 1987, *Astr. Astrophys. Suppl. Ser.*, **68**, 75.

Foster, R. S. 1990. *Constructing a Pulsar Timing Array.* PhD thesis, University of California, Berkeley.

Frail, D. A. and Kulkarni, S. R. 1991, *Nature*, **352**, 785.

Fruchter, A. S. 1989. *Pulsars Lost and Found: The Second Princeton-Arecibo Millisecond Pulsar Search.* PhD thesis, Princeton University.

Fruchter, A. S., Stinebring, D. R., and Taylor, J. H. 1988, *Nature*, **333**, 237.

Goldman, I. 1990, *Mon. Not. R. astr. Soc.*, **244**, 184.

Hagen, J. 1985, NAIC Manual No. 8319.

Hankins, T. H. and Rajkowski, J. M. 1987, *Rev. Sci. Instrum.*, **58**, 674.

Haslam, C. G. T., Salter, C. J., Stoffel, H., and Wilson, W. E. 1982, *Astr. Astrophys. Suppl. Ser.*, **47**, 1.

Helfand, D. J., Manchester, R. N., and Taylor, J. H. 1975, *Astrophys. J.*, **198**, 661.

Helfand, D. J., Taylor, J. H., Backus, P. R., and Cordes, J. M. 1980, *Astrophys. J.*, **237**, 206.

Hellings, R. W., Adams, P. J., Keesey, M. S., Lau, E. L., Standish, E. M., Canuto, V. M., and Goldman, I. 1983, *Phys. Rev. Lett.*, **51**, 1609.

Hirata, K. *et al.* 1987, *Phys. Rev. Lett.*, **58**, 1490.

Hulse, R. A. and Taylor, J. H. 1974, *Astrophys. J. (Lett.)*, **191**, L59.

———.1975, *Astrophys. J. (Lett.)*, **201**, L55.

International Astronomical Union 1976, *Trans. IAU*, **16B**, 58.

Johnston, S. 1990. *A High Frequency Survey of the Southern Galactic Plane for Pulsars.* PhD thesis, The University of Manchester.

Kulkarni, S. R. 1986, *Astrophys. J. (Lett.)*, **306**, L85.

Kulkarni, S. R., Anderson, S. B., Prince, T. A., and Wolszczan, A. 1991, *Nature*, **349**, 47.

Kulkarni, S. R., Djorgovski, S., and Klemola, A. R. 1991, *Astrophys. J.*, **367**, 221.

Kulkarni, S. R. and Hester, J. J. 1988, *Nature*, **335**, 801.

Large, M. I. and Vaughan, A. E. 1971, *Mon. Not. R. astr. Soc.*, **151**, 277.

Lyne, A. G., Anderson, B., and Salter, M. J. 1982, *Mon. Not. R. astr. Soc.*, **201**, 503.

Lyne, A. G. and Bailes, M. 1992, *Nature*, **355**, 213.

Lyne, A. G. *et al.* 1990, *Nature*, **347**, 650.

Manchester, R. N., Lyne, A. G., Robinson, C., D'Amico, N. D., Bailes, M., and Lim, J. 1991, *Nature*, **352**, 219.

Manchester, R. N., Lyne, A. G., Taylor, J. H., Durdin, J. M., Large, M. I., and Little, A. G. 1978, *Mon. Not. R. astr. Soc.*, **185**, 409.

Manchester, R. N. and Taylor, J. H. 1977, *Pulsars*, San Francisco: Freeman.

National Astronomy and Ionosphere Center 1989, *Arecibo Observatory User's Manual.*

Nordtvedt, K. 1968a, *Phys. Rev.*, **169**, 1014.

———.1968b, *Phys. Rev.*, **170**, 1186.

———.1990, *Phys. Rev. Lett.*, **65**, 953.

Press, W. H., Flannery, B. P., Teukolsky, S. A., and Vetterling, W. T. 1986, *Numerical Recipes: The Art of Scientific Computing*, Cambridge: Cambridge University Press.

Rankin, J. M. 1990, *Astrophys. J.*, **352**, 247.

Rawley, L. A. 1986. *Timing Millisecond Pulsars.* PhD thesis, Princeton University.

Reasenberg, R. D. 1983, *Philos. Trans. Roy. Soc. London A*, **310**, 227.

Romani, R. W. 1989, in *Timing Neutron Stars*, ed. H. Ögelman and E. P. J. van den Heuvel, Dordrecht, Holland: Kluwer, 113.

Ruderman, M., Shaham, J., and Tavani, M. 1989, *Astrophys. J.*, **336**, 507.

Ryba, M. F. 1991. *High Precision Timing of Millisecond Pulsars.* PhD thesis, Princeton University.

Ryba, M. F. and Taylor, J. H. 1991, *Astrophys. J.*, **371**, 739.

Segelstein, D. J., Rawley, L. A., Stinebring, D. R., Fruchter, A. S., and Taylor, J. H. 1986, *Nature*, **322**, 714.

Shapiro, I. I. 1964, *Phys. Rev. Lett.*, **13**, 789.

Shapiro, I. I., Counselman, C. C., and King, R. W. 1976, *Phys. Rev. Lett.*, **36**, 555.

Staelin, D. H. and Reifenstein, E. C. 1968, *Science*, **162**, 1481.

Standish, E. M. 1982, *Astr. Astrophys.*, **114**, 297.

Stinebring, D. R., Kaspi, V. M., Nice, D. J., Ryba, M. F., Taylor, J. H., Thorsett, S. E., and Hankins, T. H. 1992, *Rev. Sci. Instrum.* In press.

Stinebring, D. R., Ryba, M. F., Taylor, J. H., and Romani, R. W. 1990, *Phys. Rev. Lett.*, **65**, 285.

Stokes, G. H., Segelstein, D. J., Taylor, J. H., and Dewey, R. J. 1986, *Astrophys. J.*, **311**, 694.

Taylor, J. D., Wolszczan, A., Damour, T., and Weisberg, J. M. 1992, *Nature*, **355**, 132.

Taylor, J. H. 1974, *Astr. Astrophys. Suppl. Ser.*, **15**, 367.

Taylor, J. H. and Weisberg, J. M. 1989, *Astrophys. J.*, **345**, 434.

Thorsett, S. E. 1991. *Observing Millisecond and Binary Pulsars.* PhD thesis, Princeton University.

Will, C. M. 1981, *Theory and Experiment in Gravitational Physics*, Cambridge: Cambridge University Press.

Williams, J. G. *et al.* 1976, *Phys. Rev. Lett.*, **36**, 551.

Wolszczan, A. 1991, *Nature*, **350**, 688.

Wolszczan, A. and Frail, D. A. 1992, *Nature*, **355**, 145.

Wright, G. A. and Loh, E. D. 1986, *Nature*, **324**, 127.